International Journal of Heat and Mass Transfer 218 (2024) 124751

Contents lists available at ScienceDirect

International Journal of Heat and Mass Transfer

journal homepage: www.elsevier.com/locate/ijhmt

Cryogenic flow boiling in microgravity: Effects of reduced gravity on two-phase fluid physics and heat transfer

Sunjae Kim [a], Nishad Damle [a], Issam Mudawar [a,*], Jason Hartwig [b]

[a] Purdue University Boiling and Two-Phase Flow Laboratory (PU-BTPFL), School of Mechanical Engineering, Purdue University, 585 Purdue Mall, West Lafayette, IN 47907, USA
[b] Fluids and Cryogenics Branch, NASA Glenn Research Center, 21000 Brookpark Rd, Cleveland, OH 44135, USA

ARTICLE INFO

Keywords:
Cryogens
Microgravity
Flow boiling
Parabolic flight

ABSTRACT

With the growing interest in space exploration, cryogenic technologies involving two-phase flow and heat transfer are in high demand to successfully procure advanced space applications such as fuel depots and nuclear thermal propulsion (NTP) systems for deep space missions. However, the unique and extreme thermal properties of cryogenic fluids introduce distinct flow boiling fluid physics and energy transport phenomena, which differ significantly from those observed with conventional fluids. Understanding the unique two-phase physics in cryogenic flow boiling remains an ongoing challenge. Furthermore, the lack of readily available microgravity cryogenic steady-state heat transfer data hinders the assessment of gravitational effects on cryogenic flow boiling. This study aims to elucidate the gravitational effects on two-phase fluid physics and heat transfer by conducting the first-ever experimental measurement of cryogenic flow boiling performance using a steady-state heated method in a reduced gravity environment. Parabolic flight experiments were performed to acquire both heat transfer measurements and high-speed video of interfacial behaviors, under varying gravity levels (microgravity, hypergravity, Lunar gravity, and Martian gravity). The experiments involved flow boiling of liquid nitrogen (LN_2) with a near-saturated inlet along a circular heated tube of dimensions 8.5-mm inner diameter and 680-mm heated length. The operating parameters varied are mass velocity of 398.3 – 1342.8 kg/m2s, inlet quality of -0.08 to -0.01, and inlet pressure of 413.68 – 689.48 kPa. Captured microgravity flow patterns range from bubbly to annular, all having vapor structures that are larger than those under higher gravity levels. Under microgravity, absence of buoyancy yields symmetrical vapor structures without flow stratification, laying a physical foundation for the distinct two-phase heat transfer trends during LN_2 flow boiling in microgravity. Transient data collected during the flight parabolas exhibited decreasing heated wall temperature as the aircraft transitioned from hypergravity to microgravity phases. The temperature variation indicated an enhancement in flow boiling heat transfer with decreasing gravity levels and a reduction with increasing gravity levels. The effect of reduced gravity on cryogenic flow boiling heat transfer coefficient (HTC) is discussed based on steady state heat transfer analysis. Seminal HTC correlations are evaluated against the measured microgravity HTC data, of which one is identified for superior accuracy in predicting microgravity data. Finally, a new HTC correlation is proposed to improve accuracy of microgravity predictions, yet there still exists room for further improvement with future terrestrial flow boiling experiments at different flow orientations relative to Earth gravity.

1. Introduction

1.1. Importance of cryogenic two-phase fluid physics to future space missions

1.1.1. Cryogens for in-space applications

Cryogenic fluids, which are liquids that exist at extremely low

* Corresponding author.
E-mail address: mudawar@ecn.purdue.edu (I. Mudawar).

https://doi.org/10.1016/j.ijheatmasstransfer.2023.124751
Received 21 June 2023; Received in revised form 23 August 2023; Accepted 22 September 2023
Available online 4 October 2023

Nomenclature

A	area (m^2)
Bo	boiling number, q''/Gh_{fg}
c_i	empirical constant
Co	confinement number, $\sqrt{\sigma/((\rho_f-\rho_f)gD^2)}$
D	diameter (mm)
G	mass velocity (kg/m^2s)
g	gravitational acceleration (m/s^2)
g_e	Earth gravity (m/s^2)
h	enthalpy (J/kg); heat transfer coefficient (kW/m^2K)
h_{fg}	latent heat of vaporization (J/kg)
k	thermal conductivity (W/m•K)
L	length (m)
L_e	entrance length (mm)
L_H	heated length (mm)
$\dot{m}$	mass flow rate (kg/s)
P	pressure (Pa)
P_R	pressure ratio, P/P_{crit}
Pr	Prandtl number
q''	wall heat flux (W/m^2)
T	temperature (°C, K)
t	time (s)
Th	thickness (mm)
u	velocity (m/s)
x_e	thermodynamic equilibrium quality
X_{tt}	Lockhart-Martinelli parameter, $\left(\frac{1-x_e}{x_e}\right)^{0.9}\left(\frac{\rho_f}{\rho_g}\right)^{0.5}\left(\frac{\mu_f}{\mu_g}\right)^{0.1}$
z	axial coordinate (m)

Greek symbols

λ	interfacial wavelength (m)
μ	dynamic viscosity (kg/m•s)
ν	kinematic viscosity (m^2/s)
ρ	density (kg/m^3)
σ	surface tension (N/m)

Subscripts

avg	average
bot	bottom of horizontal tube
cb	convective boiling
crit	critical point
f	liquid
g	vapor
i	inner
in	inlet to heated tube
meas	measured
nb	nucleate boiling
o	outer
out	outlet
pred	predicted
s	solid wall
sat	saturation
sp	single phase liquid
sub	subcooling
top	top of horizontal tube
w	wall
z	local

Acronyms

CFM	cryogenic fluid management
CHF	critical heat flux
DNB	departure from nucleate boiling
GHe	gas helium
GN2	gas nitrogen
HTC	heat transfer coefficient
HV	hand (ball) valve
LCH_4	liquid methane
LEO	low Earth orbit
LH_2	liquid hydrogen
LHe	liquid helium
LN_2	liquid nitrogen
LOX	liquid oxygen
MAE	mean absolute error
NEP	nuclear electrical propulsion
NTP	nuclear thermal propulsion
ONBD	onset of departure from nucleate boiling
ONB	onset of nucleate boiling
SV	solenoid valve

temperatures, have found diverse applications in numerous industries. Among the different cryogenic fluids, liquid oxygen (LOX), liquid hydrogen (LH_2), liquid methane (LCH_4), and liquid helium (LHe) have garnered significant attention in recent years for their diverse applications particularly for space exploration. Having the lowest critical temperature of any known fluid, LHe is used to chill down Earth-orbiting telescopes and satellites as well as cool space experiments, where ambient space temperature is ~ 2.7 K. And following initial work around 1960, LCH_4 has received renewed interest at NASA's Glenn Research Center [1] and Johnson Space Center [2,3] as part of the Propulsion and Cryogenics Advanced Development (PCAD) project [4], where nontoxic propellants such as LOX/LCH_4 are being tested for spacecraft applications. LOX/LCH_4 and LOX/LH_2 are used in ascent stages, descent stages, and in-space fuel depots. Additionally, LH_2 has been proposed for use in several other future advanced propulsion systems such as nuclear thermal propulsio [5] n and hybrid-electric aircraft [6], where it would be used as both propellant and coolant. James Webb Space Telescope, which is deployed to L_2 Lagrange point, utilizes LHe to cryogenically cool optical instruments down to less than 7 K [7]. Most recently, NASA researchers suggested a conceptual design for inter-Marian transport vehicle utilizing two different cryogenic propulsion systems: (1) liquid oxygen/liquid methane (LO_2/LCH_4) chemical propulsion system in conjunction with nuclear electric propulsion (NEP) using xenon propellant ion thrusters, and (2) nuclear thermal propulsion (NTP), in which the reactor serves as heat source to expand liquid hydrogen (LH_2) propellant though a nozzle for thrust [8].

1.1.2. Cryogenic fluid management (CFM) and importance of flow boiling fluid physics

Cryogenic propellants have been found to offer notably higher performance in terms of specific impulse and energy density when compared to conventional propellants such as hydrazine. Aside from NTP systems, no known pure chemical propulsion system propellant combinations can deliver a specific impulse higher than those of LH_2/LO_2 [9]. In such perspective, recently reported NASA roadmap designated cryogenic fluid management (CFM) technologies as essential to achieving efficient utilization of cryogenic propellants for NASA's future long duration missions [10].

A fuel depot in low Earth orbit (LEO) and connected transfer lines comprise one of the critical components for missions traveling far outside LEO, providing the necessary propellant for maneuvering and other in-space activities. These systems typically involve the transfer of cryogenic liquids from a large volume storage tank to smaller tanks or spacecrafts [11]. During the fuel transfer, it is crucial to ensure that the

system hardware, including the feed line, flow components, and various storage tanks, be cooled down to cryogenic temperatures before providing vapor-free liquid. The cooling process is typically achieved through phase change heat transfer, where a portion of the propellant is allowed to boil, effectively removing thermal energy from the system walls [12], which highlights the importance of understanding flow boiling fluid physics of cryogens. Necessity of CFM technology is not limited to propellant transfer or storage for fuel depots but is more emphasized as a key technology area for developing NTP powered vehicles. NTP, whether designed to provide the thrust to move a spacecraft between orbits or operate as a dual-mode system that provides power and propulsion capability, provides strong architectural benefits to exploration missions and reusable in-space transportation systems [13]. Such NTP systems use a nuclear reactor to heat a propellant, such as LH_2, which is then expelled out of a nozzle to produce thrust and also used as coolant for maintaining acceptable temperature of the nuclear reactor. Consequently, the importance of understanding cryogenic flow boiling fluid physics should be highlighted in order to design high fidelity reactors and incorporated feed systems of NTP; this is equivalent to how thermal hydraulic understanding of water is crucial for pressurized water reactors (PWRs) in Earth based nuclear reactors.

The unique and extreme thermal properties of cryogenic fluids, give rise to distinct flow boiling fluid physics and energy transport phenomena that differ significantly from those observed with conventional fluids. Studies have shown that existing HTC correlations based on room temperature fluids are inadequate for predicting heat transfer for cryogens. Specifically, LH_2 quenching heat transfer data is overpredicted by as much as 200 times, which highlights the need for specialized correlations tailored to cryogenic fluids [14]. Moreover, there is significant disparity between correlations for conventional fluids and heated tube cryogenic flow boiling data, further emphasizing the necessity of specially tailored experimental data and correlations for cryogenic fluids [12]. In short, successful use of cryogenic propellants in aerospace engineering applications requires the accumulation of experimental data within a specialized database to accurately quantify the HTC as a function of relevant geometrical and flow parameters. Moreover, the effects of gravity need to be ascertained, not only for microgravity, but also partial gravity, such as Lunar and Martian gravities, to ensure applicability of the data for a range of end-users. This step is crucial for effective design and optimization of cryogenic fluid systems, given the unique and extreme thermal properties of cryogenic fluids that demand specialized modeling and analysis techniques. Fig. 1 shows examples of in-space applications requiring CFM technology.

1.2. *Influence of gravity on flow boiling fluid physics*

The work described in this paper is a continuation of Purdue University Boiling and Two-Phase Laboratory (PU-BTPFL) research efforts dating back to the mid-1980s. These efforts have included (i) development of theoretical models for fundamental two-phase flow and heat transfer mechanisms, (ii) acquisition of new databases, (iii) compilation of "consolidated databases" for different mechanisms and fluids, (iv) construction of "universal" heat transfer correlations applicable to multiple fluids, and (v) development of practical thermal management solutions for a broad variety of applications (computer electronics, data centers, avionics, energy, laser, microwave, radar, space, materials processing, etc.). These efforts encompass virtually every aspect of boiling and two-phase flow including capillary flows [15], pool boiling [16], falling films [17], flow boiling in macro-channels [18,19], flow boiling in mini/micro-channels [20,21] jet impingement [22], sprays [23], and hybrid cooling schemes [24,25]. These studies formed a foundation for recent efforts at PU-BTPFL centered on selecting most suitable and relevant thermal management schemes for adoption in space applications. Key takeaways for each scheme in microgravity

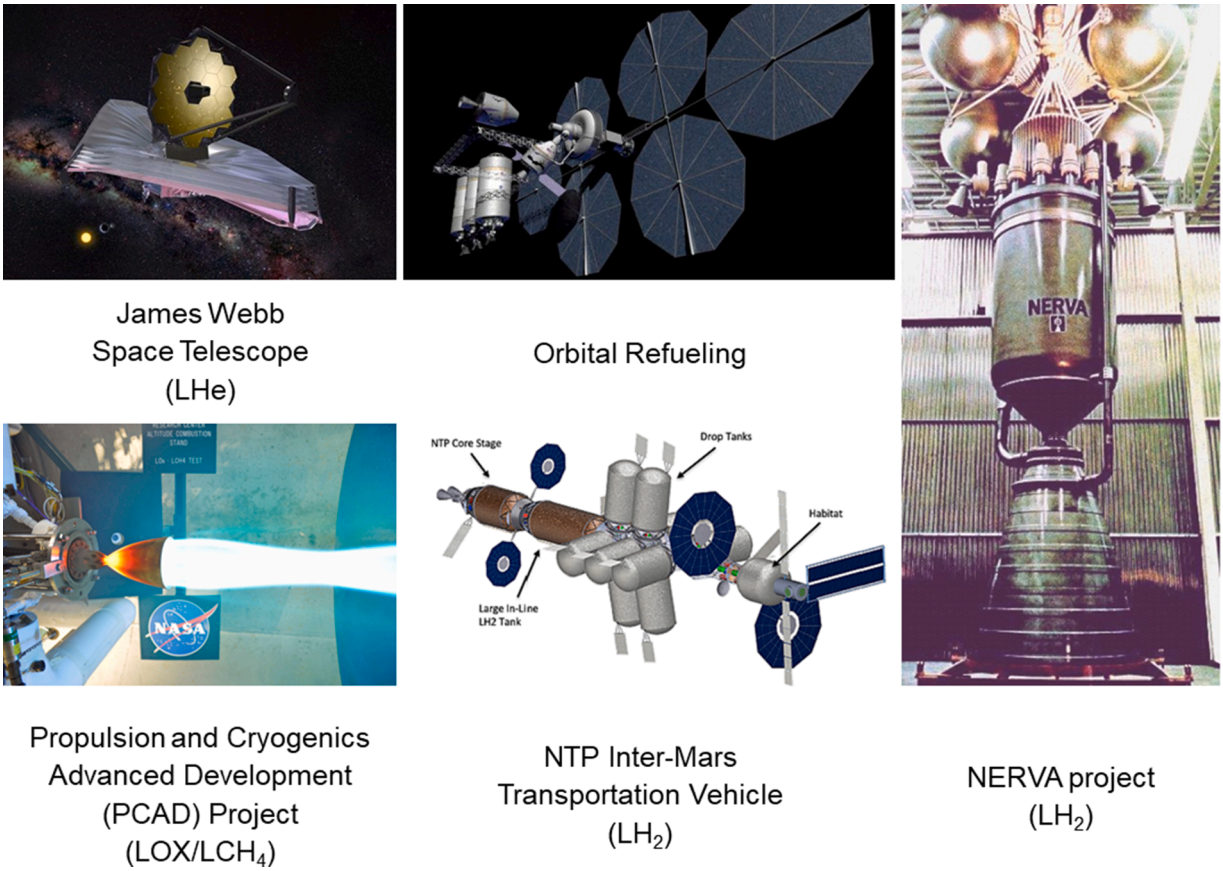

Fig. 1. Space applications of cryogens.

applications are as follows:

(i) Despite their passive circulation attributes, capillary devices (e.g., heat pipes, capillary pumped loops, loop heat pipes) can only tackle very small power densities.
(ii) Pool boiling (e.g., using thermosyphons) is very problematic in microgravity because, as described later, absence of a body force to remove bubbles from the heated surface, the produced vapor aggregates into a few enormously sized bubbles that resist liquid replenishment and therefore culminate in unusually low critical heat flux (CHF).
(iii) Falling-film schemes, because of reliance on gravity to drive the cooling liquid film, are inoperable in microgravity.
(iv) Macro-channel and mini/micro-channel boiling are well suited to cooling high-heat-flux surfaces in space applications. Key to their adaptability are small weight and volume requirements (often using "cold plates') and ability to tackle high-heat-fluxes, the latter being outcome of reliance on fluid motion rather than body force to flush bubbles away from and sustain supply of bulk liquid to heated surfaces. Notably, flow boiling in tubes is the primary focus for the present study.
(v) While jet impingement is well known for ability to tackle very high heat flux situations, to maintain uniform surface temperatures for sensitive devices, they demand use of multiple jets thereby greatly increasing coolant flow rate requirements, which is less desirable in space applications.
(vi) Spray cooling mirrors high flux advantages of jets but, by breaking the liquid flow into fine droplets which are dispersed upon the heating surface, provides better cooling uniformity with lesser flow rate than jets. This is one reason sprays are found in several space applications especially in fuel delivery and chilldown.

As future space applications for two phase flow boiling are subject to varying gravitational environments, it is of paramount importance to investigate gravitational effects on flow boiling fluid physics to safely and cost-efficiently design in-space fluid and thermal management systems. Despite this obvious inference, present understanding of gravitational effects on two-phase flow and heat transfer is quite limited. For conventional fluids, such as water, FC-72, and perfluorohexane (C_6H_{14}), microgravity flow boiling experiments have been carried out for over two decades. Saito et al. [26] performed microgravity flow boiling experiments via parabolic flight using water in 25-mm square channel and compared flow visualization and heat transfer data against horizontal flow boiling data in terrestrial gravity. Compared to Earth gravity they observed a significant decrease in bubble detachment causing bubbles to grow larger especially in the channel's downstream. This distinction was more pronounced at low flow rates, high heat fluxes, and low subcoolings. Interestingly, they reported very small differences in HTCs between the two gravitational environments. Misawa [27] reported earlier transitions among two-phase flow patterns in microgravity than in terrestrial gravity but these effects diminished at high flow qualities. They also described how attenuation of bubble-agitation-induced turbulence leads to heat transfer degradation in microgravity. Ohta et al. [28] conducted parabolic flight experiments involving flow boiling along an 8-mm i.d. transparent Pyrex glass tube which was electrically heated using thin gold film. For low quality bubbly flow conditions, heat transfer during nucleate boiling was consistent between 1-g_e and microgravity for both low and high mass velocities. For moderate quality, nucleate boiling in microgravity was suppressed with a more dominance of annular flow, which caused deterioration in the heat transfer performance. Overall, gravity effects were negligible altogether at high velocities, high quality annular flow, and very low quality flow (where heat transfer is dominated by nucleate boiling). And, in microgravity, greater amounts of vapor were produced due to absence of buoyancy, which resulted in larger bubble diameters and earlier transition to annular flow. Zhang et al. [29] conducted both 1-g_e and parabolic flight experiments involving flow boiling of FC-72 along a rectangular flow channel heated along one wall. High-speed video revealed how, at low flow velocities, bubbles in horizontal 1-g_e flow with heat supplied along the underside more easily detached and were driven by buoyancy across the channel, resembling pool boiling, while no such detachment was observed in microgravity. Konishi et al. [30,31] carried out parabolic flight experiment to investigate flow boiling of FC-72 in a rectangular channel heated along two opposite walls. While bubbly flow was prevalent at low heat fluxes, high heat fluxes (especially close to CHF) produced a distinct wavy vapor layer regime along the heated walls. Overall, microgravity degraded heat transfer effectiveness. Iceri et al. [32] flow boiling experiments with FC-72 along a vertical upflow aluminum tube both in microgravity and hypergravity environments. High gravity was observed to decrease both bubble size in bubbly flow and liquid film thickness in annular flow, leading to improved heat transfer. However, for low-quality subcooled flow, gravity effects were inconsequential. The same study compared data to predictions of seminal HTC correlations, concluding none provide acceptable results for all gravitational environments and both subcooled and saturated inlet conditions.

When it comes to cryogenic flow boiling, a very limited number of microgravity experiments have been conducted, and all of which employed the quenching method rather than steady-state heating method. Kawanami et al. [33] conducted microgravity quenching experiment in a 500-m high drop tower which produced approximately 10 s of microgravity (10^{-4} to 10^{-3} of Earth gravity) and compared results to ones conducted in 1 g_e. They investigated relatively low mass velocity (300 to 500 kg/m^{2}s) LN_2 flow boiling along a vertically mounted transparent Pyrex glass tube with 7-mm i.d. and length of 50 mm. They reported the HTC was enhanced in μg when compared to 1-g_e, evidenced by reduced quenching time. Yuan et al. [34] conducted microgravity LN_2 quenching experiments in a drop tower that provided 1.7 s of microgravity (10^{-5} to 10^{-4} of Earth gravity) using a horizontally oriented transparent quartz tube with 11.1-mm i.d. and length of 254 mm. Their investigation was focused on very low mass velocities (3.6 to 10.8 kg/m^{2}s) and only annular film boiling, which yielded degraded heat transfer (slowed quenching) in μg when compared to 1-g_e. Darr et al. [35] conducted microgravity LN_2 quenching experiments in parabolic flight onboard C9 aircraft which provided 20 – 23 s of μg using a stainless steel (SS304) tube with 11.68-mm i.d. and length of 572 mm. By comparing quenching data to 1-g_e data for mass velocities between 31 and 503 kg/m^2, they reported a 20 – 25 % reduction in average heat flux for the former and concluded that chilldown in reduced gravity is less efficient than in 1-g_e.

Unfortunately, there are no publicly available reduced gravity cryogenic transfer line data that are measured using the more accurate steady-state heating method. To date, only ground-based cryogenic heated tube testing has been conducted [36], and no one has flown a cryogenic flight rig with provisions for taking steady-state heating data. Given that flow boiling is heavily gravity-dependent, this limitation casts doubt over usefulness of such cryogenic data for design of space-based cryogenic systems. Additionally, there is abundant evidence that available correlations derived from databases for room temperature fluids fail to accurately predict even terrestrial cryogenic flow boiling data [14]. This fact points to a need to conduct parabolic flight experiments that employ steady-state heating in a quest for much needed reduced gravity cryogenic fluid data and better understanding of cryogenic flow boiling fluid physics.

1.3. Parabolic flight experiments

Researchers have explored the effects of gravity on two-phase flow boiling by performing Earth-gravity experiments at different flow orientations [37], or short-duration microgravity experiments in drop towers [38], sounding/ballistic rockets [39], parabolic flight aircraft

[30,31], or long-duration experiments onboard the International Space Station (ISS) [40]. Of those, parabolic flight aircraft offer a cost-effective approach to performing microgravity experiments with microgravity duration lasting from 15 to 30 s. The microgravity period is attained through a series of parabolic maneuvers executed by the aircraft several tens of times, with each parabola preceded and followed by brief periods of high gravity or hypergravity. Minor drawbacks here are gravity jitter and microgravity control; both are influenced by both pilot skills and weather conditions. Nonetheless, parabolic flight experiments provide several important advantages over drop tower, including longer microgravity duration, ability to accommodate larger experimental payloads, and direct operator interaction during the experiment [41]. Ability to accommodate large payloads is especially important to cryogenic microgravity experiments, whose payloads are generally heavier and more voluminous than conventional room temperature fluid payloads. This is the result of using multiple pressure tanks in an open-loop cycle, such as a large LN_2 dewar along with gaseous nitrogen (GN_2) or gaseous helium (GHe) pressure cylinders. Furthermore, ability of parabolic flight aircraft to allow for outboard venting offers significant benefits by simplifying payload construction and eliminating the need for gas collection by compression. The current study employs a parabolic flight aircraft of Zero-G corporation, a modified Boeing 727–200F, for conducting microgravity cryogenic flow boiling experiments.

1.4. Objectives of present study

This study presents results obtained from microgravity cryogenic flow boiling experiments using LN_2 as working fluid. The experiments are conducted in a parabolic flight aircraft using a specially designed and constructed cryogenic payload, which is the first of its kind. The overarching purpose of the experiments is to collect and acquire LN_2 two-phase heat transfer data using the steady-state heating method which has never been attempted before. Additionally, high-speed video is used to capture interfacial behavior to supplement the heat transfer data with detailed understanding of the flow boiling fluid physics. Results are provided not only for the microgravity duration of a parabola but also in hypergravity and partial gravity (both Lunar and Martian). Heat transfer results are presented in the form of boiling curves, streamwise profiles of local wall temperature and local HTC, and average HTC. The acquired microgravity data are compared with previously measured terrestrial data [42] to further understanding of the influence of gravity on heat transfer behavior. Furthermore, the microgravity data are used to assess the accuracy of prior terrestrial-gravity two-phase heat transfer correlations. A new HTC

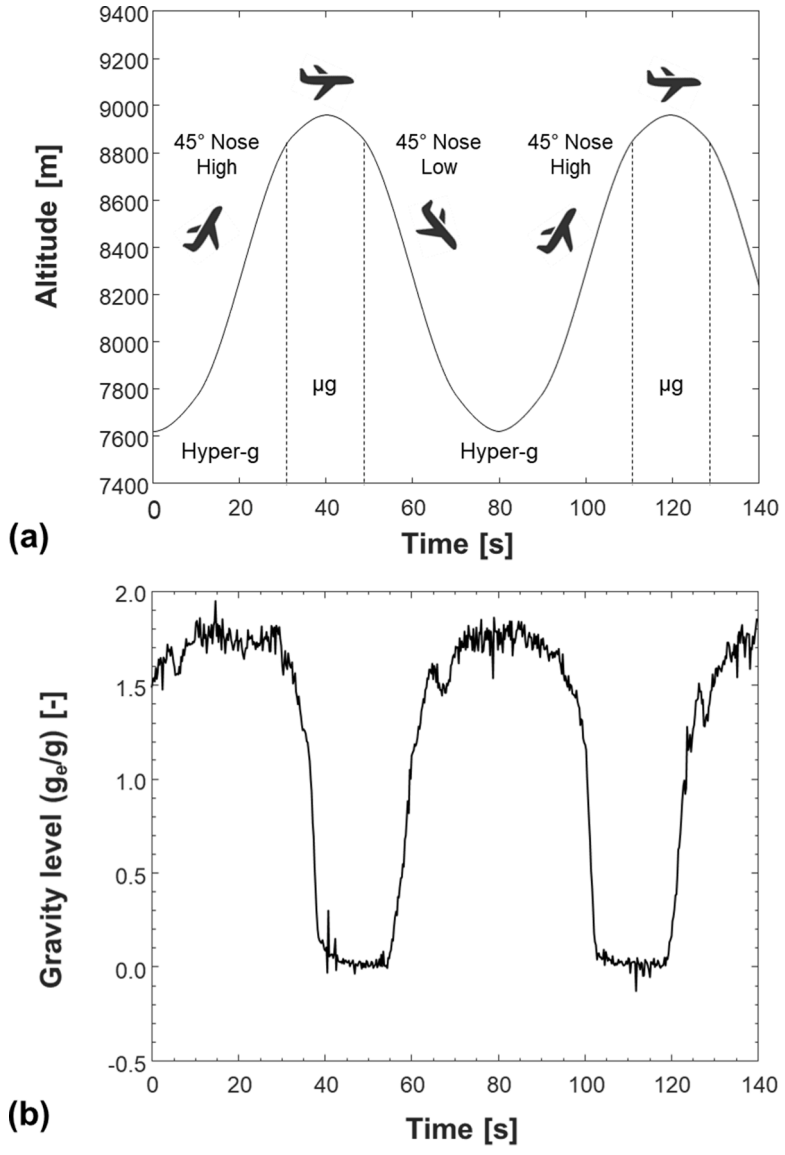

Fig. 2. Representative schematics of (a) trajectory and (b) varying gravity level during parabolic flight maneuver.

correlation is proposed which shows superior accuracy compared to prior predictive tools. In future studies, the new correlation will be the basis for further accuracy improvement as additional HTC data are acquired from future experiments.

2. Experimental methods

2.1. Flight platform

A total of 150 parabolas were flown on Zero-G aircraft during two separate flight campaigns with a total of five flight days. Fig. 2 provides schematic illustrations of a trajectory and varying gravity level experienced during a parabolic flight maneuver. Depicted in Fig. 2(a), a single parabola is initiated by pulling up the aircraft nose with an angle of 45°, resulting in hypergravity phase of approximately 1.8 g_e. Subsequently, at an altitude of approximately 30,000 ft (9,144 m), the aircraft nose is lowered to 0°, creating a microgravity condition which persists for approximately 15 to 20 s. This is followed by another hypergravity phase as the aircraft descends with a 45° downward nose angle to initiate the next parabola. Fig. 2(b) shows measured gravitational acceleration during one of the parabolic flight maneuvers. Reacting to the described flight maneuvering, hypergravity phase is indicated by a gravity level ranging between 1.5 and 1.8 g_e. Upon the sudden lowering of the aircraft's nose, gravity level rapidly decreases, reaching microgravity condition of approximately 0 ± 0.02 g_e, which persists for a duration of 15–20 s.

It is important to note that design of parabolic flight payloads requires careful conformance to several mostly safety requirements. First, weight and size restrictions posed by the flight provider impose hard-set limits that have profound influence on operating conditions for the intended test matrix. Second, the payload must satisfy strict structural integrity criteria also stipulated by the flight provider. Meeting such criteria requires careful structural analysis of the payload in documents provided and approved well before the flight experiments. Third, any venting of the payload's working fluid must take place in gaseous state. Fourth, but most importantly, use of a cryogenic dewar in parabolic flight requires careful consideration of pressure decline due to ullage. To avoid pressure decline in the dewar artificial pressurization is necessary, wherein a non-condensable gas from a separate pressure cylinder is used to drive the cryogen out of the dewar. For the present study, gaseous helium (GHe) having 99.99 % purity was used to pressurize liquid nitrogen (LN_2) in the dewar during the microgravity experiments.

2.2. Experiment facility

2.2.1. Two-phase flow loop

Fig. 3 depicts a schematic of the open-loop two-phase flow system utilized to (i) provide working fluid, LN_2, into the test section and (ii) safely vent fluid from the test section outlet to ambient air outboard the aircraft. Although the experimental set up has been thoroughly documented in Kim et al. [42], a concise summary is provided herein to aid understanding of the obtained results.

Since the loop is designed as open circuit, a helium gas (GHe) cylinder with a volume of 44 L, which is initially pressurized to 14.5 MPa, is connected to the LN_2 dewar. By pressurizing liquid in the dewar, resulting positive pressure difference pushes the LN_2 out of the dewar.

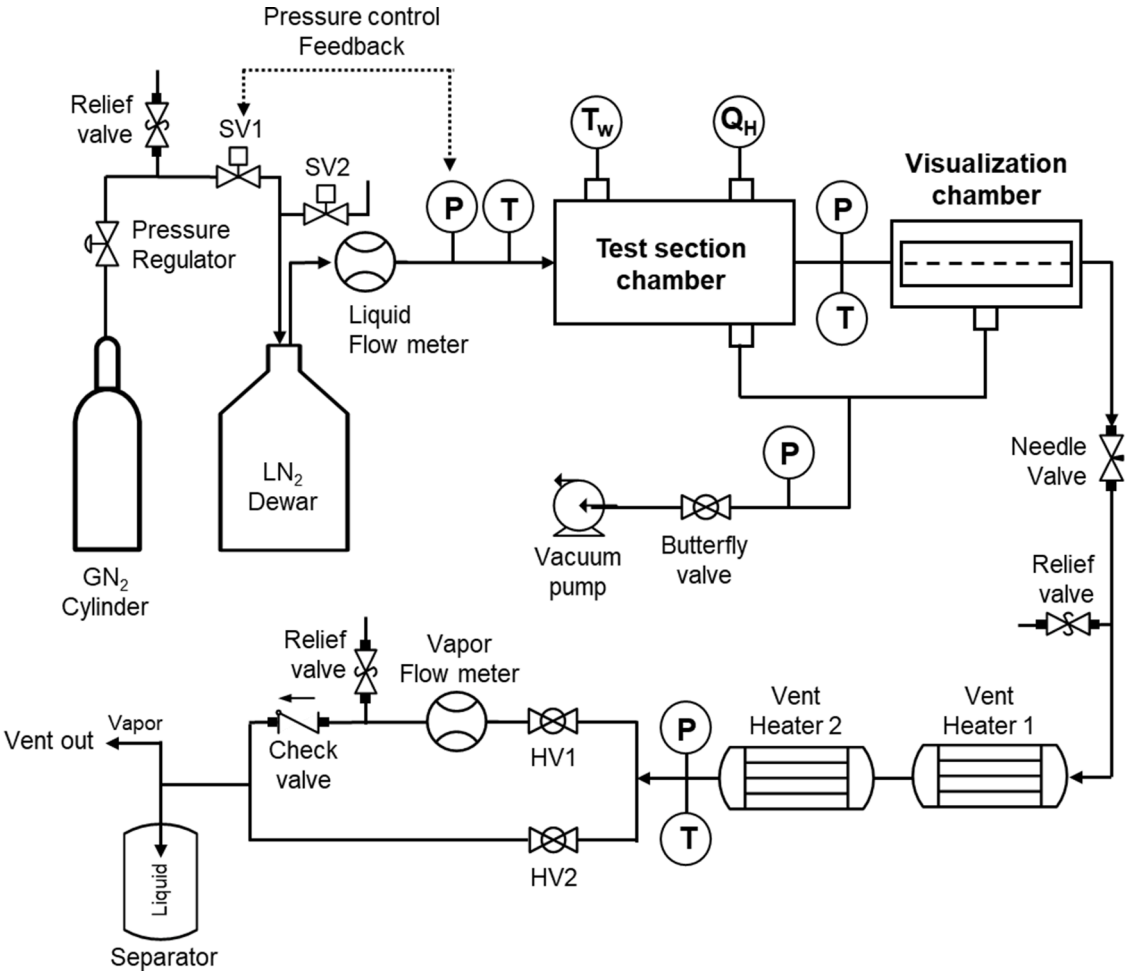

Fig. 3. Schematic of two-phase flow loop.

The liquid passes into a turbine flow meter to measure the volume flow rate. To determine the mass flow rate accurately, fluid density information is required. Therefore, the temperature and pressure of the fluid are measured immediately downstream from the flow meter to obtain accurate thermal property values for the incoming liquid. The liquid then enters the test section, where a finite amount of heat is added, causing the fluid to undergo phase change and emerge as a two-phase mixture. At the outlet of the test section, fluid temperature and pressure are measured at the same axial location. The fluid is then directed into an adiabatic visualization chamber featuring a transparent Pyrex tube, which is used to capture interfacial behavior with the aid of high-speed video camera (additional design details relating to the test section and visualization chamber are provided in a later section). Note that, in order to preserve the developed flow structure from the test section until the visualization section, the inner diameter is maintained constant with the inner diameter of test section tube from the inlet of the test section chamber to the outlet of the visualization chamber, minimizing any flow distortion. A cryogenic grade needle valve is installed downstream of the visualization section to regulate the flow rate. The needle valve facilitates fine-tuning of the fluid's mass velocity by sensitively controlling the vertical movement of the needle in 11 rotations from fully open to fully closed. Two 3-kW rated vent heaters are serially connected downstream of the needle valve to fully evaporate any remaining two-phase mixture to pure vapor phase. Note that it is a mandatory

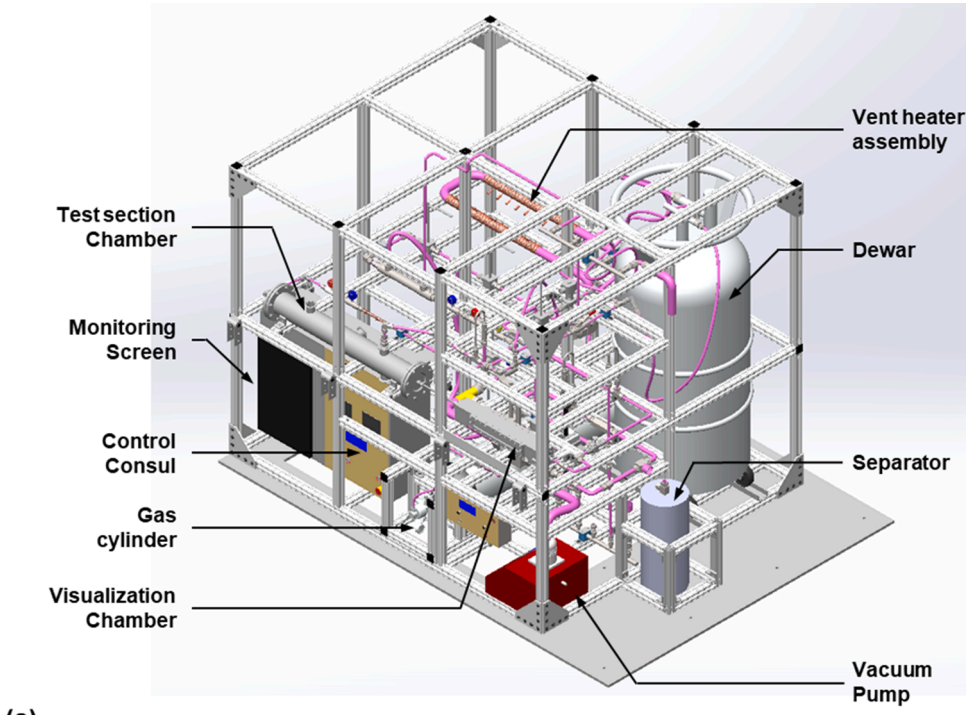

Fig. 4. (a) 3D CAD model and (b) picture of the experimental facility.

requirement from Federal Aviation Administration (FAA) to allow only gaseous nitrogen to be vented outboard the aircraft. At the outlet of the second vent heater, fluid temperature and pressure are measured, which, coupled with the volume flow rate reading from a vapor flow meter, facilitate determination of the mass flow rate. The flow loop is divided into two flowlines, one with the vapor flow meter and the other without. Flow into the parallel flowlines is controlled manually using ball valves indicated in Fig. 3 as HV1 and HV2. The vapor flow meter is used to measure low fluid mass velocities below 100 kg/m^{2}s while mass velocities above 100 kg/m^{2}s are measured by the upstream liquid flow meter. However, mass velocity range for the present study never reached below 100 kg/m^{2}s. For the mass velocities higher than 100 kg/m^{2}s, HV1 is closed to prevent failure of turbine blades or bearing of the vapor flow meter due to abnormally high rotation speed. Farther downstream, the two flowlines are merged and connected to a receiver tank which serves to eliminate any possibility of liquid escaping outboard in improbable situations such as vent heater power loss. The two-phase mixture is then separated into liquid that is trapped in a receiver tank while vapor is vented outboard the aircraft.

Fig. 4 displays a 3D CAD drawing of the flight payload containing the entire flow components along with an actual picture of the payload. The flight rig is built upon a 12.7-mm thickness aluminum (AL7075-T6) baseplate with carved out hollow interior (to reduce weight) and an 80/20 aluminum structure to ensure structural integrity of the entire setup. The flow loop is situated in the lower middle part of the payload. From the inlet of the test section to the inlet of the vent heater, piping is maintained at the same elevation to prevent any secondary flow effects due to differences in hydrostatic pressure. This is especially important during parabolic flight wherein vertical movement of fluid in the presence of drastic variations in gravity acceleration can induce unwanted two-phase flow instabilities. The dewar is positioned in the back-right cubicle with rails upon which the dewar can be easily installed or removed. Two vacuum chambers, one surrounding the test section and another the visualization chamber, are positioned toward the front of the payload, near to where the system operators are situated. The vent heater assembly is stationed in the back-left corner on the middle plane of the payload as a U-shaped tubing fitted with 20 individual nozzle heaters producing 6 kW in total. The U-shape of the tubing is intended for the compactness of the assembly so that it can sufficiently fit into the dedicated space within the flight rig. The payload's control consul is situated in the bottom-left corner of the flight rig. This component contains all electronic devices, including a data logger, AC power distributors, a DC power converter, circuit breakers, heater power controllers for test section heaters, heater temperature controllers for vent heaters, power meters for heaters, and an Arduino board for pressure automation control. All the controlled and measured parameters are integrated through LabVIEW software and displayed on a monitor installed on the front of the control consul.

2.2.2. *Heat transfer test section and visualization section*

The primary components of the payload are the test section and the visualization section. The test section is comprised of a heated tube that is enclosed within a test section vacuum chamber serving to minimize heat loss. As shown in Fig. 5(a), the vacuum chamber has inner diameter of 0.1 m and length of 0.8 m and is fitted with flanges on both ends to ensure vacuum tight enclosure. A center hole is machined through each flange for insertion of the heated test section. The vacuum chamber is equipped with four feedthrough ports, three are vertical and one

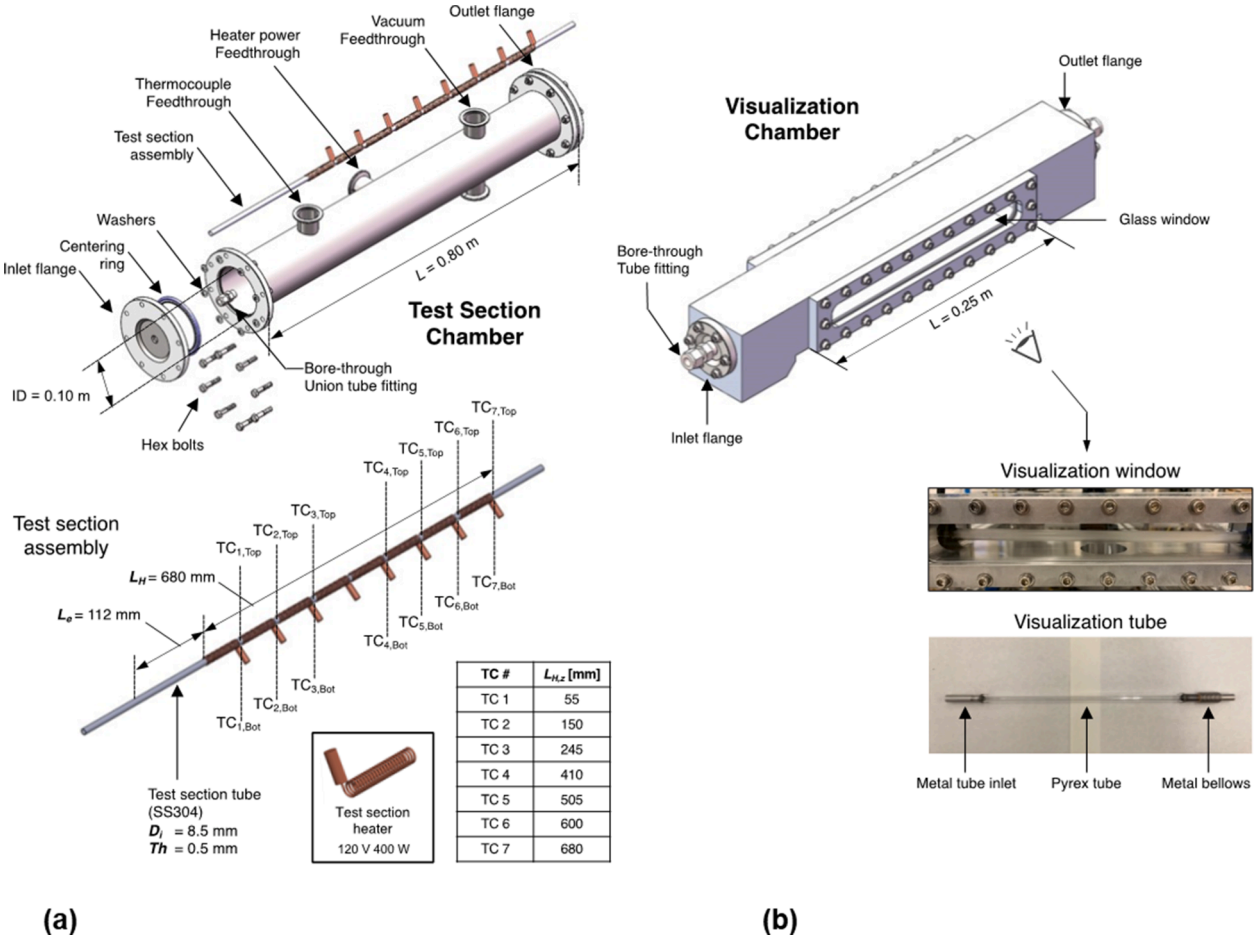

Fig. 5. Schematics of (a) test section chamber and assembly, and (b) visualization chamber with pictures of visualization window and Pyrex tube.

horizontal. The two vertical feedthroughs near to the outlet are for vacuum hose connections while the foremost vertical feedthrough passes wires from thermocouple attached to the outer wall of the test section to an external control box containing the data logger. The horizontal feedthrough passes heater power leads from the test section's eight individual heaters. The test section assembly is comprised of a heating tube, eight individual heaters, and thermocouples wires. Test section heated tube is a thin walled ($Th = 0.5$ mm) stainless steel (SS304) tube with i.d. of $D_i = 8.5$ mm, heated length $L_H = 0.68$ m, and entrance length $L_e = 0.112$ m. The transient behavior of wall temperature heavily relies on the tube wall thickness design. The larger the thermal mass of the heated tube, the longer it takes to reach a steady state. Concurrently, findings reported by Zhang et al. [29] reveal the independence of CHF on wall thickness for values greater than 0.4 mm. Therefore, to achieve the fastest thermal response during parabolic flight experiments, the heated tube wall thickness must be maintained as small as possible while satisfying the asymptotic CHF criterion. Based on this methodology, the wall thickness of the test section tube was determined to be 0.5 mm. Note that the stainless-steel tube employed in this study adheres to the ASTM A269 standard and possesses a Bright Annealed (BA) surface finish. Eight individual electrically powered coil heaters, depicted schematically in Fig. 5(a), surround the test section's heated tube to provide uniform heat flux along the tube wall. At 120 VAC power input, each heater can dissipate up to 400 W, for total capacity for the eight heaters of up to 3200 W. Seven pairs of thermocouples are attached to the heated tube wall at seven axial locations, one in each pair is mounted at the top and a second the bottom. Detailed axial locations of the thermocouples are provided in table form in Fig. 5(a). Aside from using vacuum to minimize heat loss, the entire test section assembly is wrapped with layer of insulation which is also covered with aluminum sheet to minimize loss by radiation.

Shown schematically in Fig. 5(b), the visualization section is comprised of an adiabatic glass tube enclosed in a visualization vacuum chamber. The tube is made of Pyrex glass and fitted on one end with flexible metal bellows to accommodate thermal expansion as captured in Fig. 5(b). The adiabatic glass tube has outer diameter of $D_o = 9.5$ mm and length of 364.2 mm. The vacuum chamber, which is intended to minimize heat transfer to the glass tube, features rectangular stainless-steel construction with inlet and outlet flanges on both ends to ensure tight vacuum enclosure. As shown in Fig. 5(b), transparent glass windows are attached to opposite lateral sides providing a visualization length of 0.25 m; one window is used for video camera viewing and the other for backlight illumination.

Vacuum in both the test section chamber and visualization chamber is achieved by connecting both to a vacuum pump equipped with both a turbopump and a multistage diaphragm pump to achieve 10^{-5} hPa.

2.3. Instrumentation and measurement accuracy

As shown in Fig. 5(a), 2 pairs of 7 type-E thermocouples are installed to the outer surface of the heated tube to enable axial wall temperature measurements. Three additional type-E thermocouples extend into the flow to measure local fluid temperature at test section inlet, test section outlet, and vent heater outlet. To validate the reliability of the installed thermocouples, single-phase heat transfer coefficients, measured in terrestrial environment before flight, were assessed against predicted heat transfer coefficients calculated using single-phase heat transfer coefficient correlation developed by Gnielinski [43]. The assessment results showed MAE of 7.39 %, revealing the validity of the utilized thermocouples, as shown in Fig. 6. Local pressure measurements are made using four Omega Engineering absolute pressure transducers situated at test section inlet, test section outlet, vent heater outlet, and vacuum pump inlet. Two turbine flow meters are used to measure flow rate. The liquid flow meter situated upstream of the test section has a range of 1.01×10^{-2} to 5×10^{-1} L/s while the downstream vapor flow meter is rated for 9.4×10^{-1} to 7.1 L/s. The measured volume flow rate

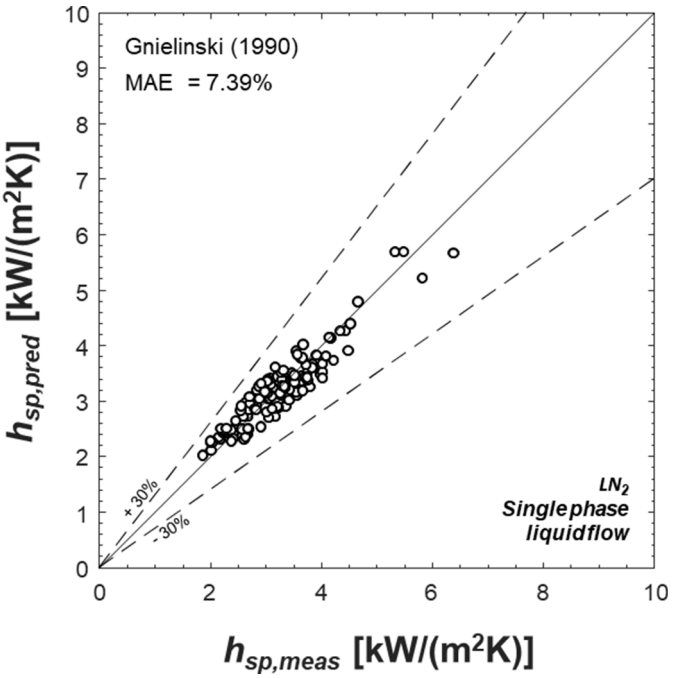

Fig. 6. Comparison of single phase heat transfer coefficients measured in terrestrial environment against predicted single phase heat transfer coefficients calculated by Gnielinski [43] correlation.

is converted into mass flow rate using liquid or vapor density information acquired from temperature and pressure sensors mounted in close proximity to respective flow meter.

To power the three test section heaters, vent heater 1, and vent heater 2, three separate power circuits from the aircraft's power panels are utilized to maintain electrical current for each below the allowable limit. A circuit breaker in each power circuit guards against any unintended power trip in the corresponding panel. Test section heater power input, a major control parameter for the flow boiling experiments, is measured using Yokogawa WT310 high accuracy power meter.

All temporal temperature, pressure, flow meter, and power meter signals are measured using a National Instruments data acquisition system (DAQ) at sampling rate of 80 Hz. Collected temporal data are processed using LabVIEW software and made visible on the payload's front monitor. Maximum uncertainties in measurements of relevant parameters are given in Table 1.

From the measurement uncertainties reported in Table 1, uncertainty propagation is analyzed and the maximum uncertainty in several important parameters are estimated using the root mean square method. Adopting a highly conservative approach with a 1 % uncertainty in length measurements, the majority of cases demonstrated uncertainty in local heat transfer coefficient, $h_{tp,z}$, that remained below 10 %. Moreover, leveraging the uncertainties associated with local heat transfer coefficients, the subsequent propagation of uncertainties for the average heat transfer coefficient was calculated. As anticipated, due to the cumulative impact of uncertainties, uncertainty for average heat transfer coefficient is larger than those of local heat transfer coefficient.

Table 1
Measurement uncertainties.

Parameter	Maximum Uncertainty
Fluid temperature, T_f	±0.5 °C
Wall temperature, T_w	±0.5 °C
Volume flow rate, $\dot{V}$	±0.1 % reading
Absolute Pressure	±0.25 % reading
Heat input, Q	±0.25 % reading

Nevertheless, the uncertainty in the majority of the $h_{tp,avg}$ dataset remains below 15 %. Furthermore, maximum uncertainty for the vapor quality is 5.01 %.

2.4. Flow visualization

The dynamic interfacial behavior of the two-phase flow is captured in the adiabatic visualization section using a high-speed video camera at each steady state point along the boiling curve and at CHF. Note that the adiabatic construction of the visualization section means the captured flow structure is preserved from the outlet of the test section to the outlet of the visualization chamber.

As indicated earlier, the Sentech high-speed video camera faces one of the visualization chamber's windows while the opposite window is backlit with blue light emitting diodes (LEDs) to minimize heat leak into the section. A light diffusing film is used to ensure uniform light intensity over entire viewing length of the visualization chamber. The video camera can capture images with 2040 × 350 (HxW) pixel resolution at 1000 frames/s and with shutter speed of 25.8 – 45 μs. A single captured video image sequence consists of 250 frames or about 250 ms of flow visualization data per steady state point. It is noted that all high-speed video images reported in this paper have been uniformly post-processed to render flow features more distinct.

2.5. Operating procedure

To control and maintain system pressure, a high pressure GHe gas tank is used along with two solenoid valves for pressurization (SV1) and de-pressurization (SV2). The solenoid valves are automatically controlled to maintain test section inlet pressure to the set value. If the sensed test section inlet pressure is lower than the target pressure, SV1 opens for pressurization. Whereas if the sensed test section inlet pressure is higher than target pressure, SV2 opens for depressurization. However, with the nature of open loop system, if not pressurized, system pressure naturally decreases. After several preliminary testing runs, it is observed that sudden pressure reduction by opening SV2 is not necessary nor beneficial for system pressure control. Therefore, the automation code is amended to use only SV1 (the pressurization valve) to control system pressure.

To initiate operation onboard the aircraft, target system pressure is set as input in the payload's pressure control panel. The dewar's liquid valve is then opened to allow liquid flow into the flow loop. Due to the sudden opening of this valve, system pressure drastically drops below the set pressure. This is when the automated system commences active pressurization by opening SV1. The entire flow loop undergoes quenching with continuous fluid flow until the inlet condition is matched with target inlet subcooling and pressure. Note that the inlet subcooling was achieved through the pressurization of the dewar using gaseous helium. The dewar pressure was elevated by introducing gaseous helium both before and during each case. This rapid pressurization of the dewar led to an increase in the system saturation temperature, while the stored liquid nitrogen within the dewar remained in a subcooled state. Across each boiling curve, a persistent inlet subcooling was successfully upheld. At the same time, it is always ensured that fluid state is in pure liquid by flow visualization monitoring. After the confirmation of subcooled liquid state at the test section inlet, the needle valve is manually adjusted to match flow rate to target value. Note that both vent heaters are ensured to be powered on and automatically controlled by temperature controllers to maintain surface temperature of 200 °C whenever the fluid is flowing through the flow loop.

For each boiling curve, provided that the flow loop is fully quenched and have inlet conditions matched, the test section heater is slowly powered up with small increments until CHF is reached. Note that with the increase of heater power, pressure drop across the test section increases due to increased vapor generation. Accordingly, due to the increased pressure drop, flow rate decreases, again, since the system is an open loop. Therefore, in order to maintain consistent flow rate, the needle valve is manually operated to increase and match target flow rate for each boiling curve. After each heater increment, steady state is reached and maintained for steady state data and camera recordings. Subsequent analysis of collected data confirms that steady state is indeed reached for all heat flux increments. Although CHF is defined as the heat flux increment which causes an unsteady rise in surface temperature, for safety and simplicity, CHF is designated to have occurred at the heat flux increment which causes at least one of the thermocouples to show extreme temperature excursion. As CHF is reached, heater power is immediately ramped down to zero to prevent any damage to the test section or thermocouples. All temporal data and high-speed videos are recorded. This procedure is repeated for all predetermined inlet conditions in the test matrix.

2.6. Data processing and experimental ranges

Steady state data are extracted from recorded temporal data by identifying each heater increment and confirming wall temperature reaching steady state. Extracted temporal data are averaged for each steady state period. Necessary thermophysical properties for nitrogen are retrieved from NIST-REFPROP [44].

Test section inlet enthalpy is found based on measured inlet temperature, T_{in}, and inlet and pressure, P_{in}, as

$$h_{in} = h(T_{in}, P_{in}) \tag{1}$$

Test section local enthalpy, h, at any z location from the heated inlet, and outlet enthalpy, h_{out}, are both calculated by application of energy conservation,

$$h(z) = h_{in} + \frac{q''\pi D_i z}{G\left(\pi D_i^2/4\right)} \tag{2a}$$

$$h_{out} = h_{in} + \frac{q''\pi D_i L_H}{G\left(\pi D_i^2/4\right)} \tag{2b}$$

Local thermodynamic equilibrium quality, $x_{e,z}$, is calculated according to the relation

$$x_{e,z} = \frac{h - h_f\big|_P}{h_{fg}\big|_P} \tag{3}$$

where h_f, and h_{fg} are, respectively, saturated liquid enthalpy, and latent heat of vaporization corresponding to local pressure which is linearly interpolated between measured inlet pressure, P_{in} and outlet pressure, P_{out}.

Local fluid temperature is determined based on the following relations:

$$T_{f,z} = \begin{cases} T_{in} + \left(T_{sat}|_{xe=0} - T_{in}\right)\dfrac{Z}{L_{sp}} & x_{e,z} < 0 \\ T_{sat,z} & 0 \le x_{e,z} \le 1 \end{cases} \tag{4}$$

where L_{sp} is the heated single-phase length, which is calculated as

$$L_{sp} = \frac{G\left(\pi D_i^2/4\right)}{q''\pi D_i}\left(h_f\big|_{P_{in}} - h_{in}\right) \tag{5}$$

The local heat transfer coefficient (HTC) is defined based on measured local wall temperature and calculated local fluid temperature for each axial location,

$$h_z = \frac{q''}{\left(T_{w,z} - T_{f,z}\right)} \tag{6}$$

Local inner wall temperature, $T_{w,z}$, at each axial thermocouple location is determined from measured outer wall temperature, $T_{w,o,z}$, and measured heat flux, q'', by accounting for conduction resistance across the heated tube wall,

$$T_{w,z} = T_{w,o,z} - \frac{q'' \pi D_i \ln(D_o/D_i)}{2\pi k_s} \quad (7)$$

Note that all the presented wall temperatures, $T_{w,z}$, are from bottom wall, noting lack of distinction between top and bottom in microgravity. Owing to the nature of parabolic flight having hypergravity phase before every microgravity phase, top wall has slightly higher wall temperatures than those of bottom wall. To avoid unwanted uncertainty, strictly only the bottom wall measurements were utilized for analysis.

The average HTC is calculated using the relation

$$\overline{h} = \frac{\iint dA}{\iint \frac{1}{h_z} dA} \quad (8)$$

which is based on harmonic averaging as proven by Ganesan et al. [45] for a constant wall heat flux boundary.

Ranges of operating conditions for the study are summarized in Table 2.

3. Flow visualization results and discussion

3.1. Temporal dynamics of flow boiling in parabolic flight

Fig. 7 presents temporal variations of recorded inlet fluid temperature, $T_{f,in}$, outlet fluid temperature, $T_{f,out}$, and heated wall temperatures, $T_{w,i,top}$ and $T_{w,i,bot}$, in response to incrementally increasing wall heat flux, q'', for inlet pressure of $P_{in} = 413.6$ kPa and $G = 840$ kg/m^{2}s. The notations of "top" and "bottom" are based on respective thermocouple locations on the horizontal heated tube in the payload; for periods of microgravity these notations do not represent orientation relative to Earth's gravity. The temporal plots shown represent data corresponding to a representative boiling curve from $q'' = 0$ to q''_{CHF}. Fig. 7 also shows the temporal variation of gravitational acceleration, which varies between hypergravity of 1.8 g_e and microgravity of $0 \pm 5 \times 10^{-2}$ g_e in response to parabolic maneuvers of the aircraft. For every flight day, 30 parabolas were executed in sets of five parabolas separated by three to five minutes "turn-around" periods. During the turn-around, experimental operating conditions including heater power, flow rate, and inlet pressure remain unchanged. Note that over the span of three to five minutes of turn-around phase, the aircraft executes continuous maneuvers in order to maintain its position within the designated airspace. The aircraft's maneuvering, during the turn-around, involves not only circular motion but also includes ascending and descending movements. These combined movements result in a continuous alteration of the gravitational acceleration experienced by the two-phase flow structure within the heated tube. Consequently, the wall temperatures also undergo continuous changes in response to the fluctuating flow structure, a direct consequence of the varying gravitational field influencing the behavior of the two-phase flow. The case shown in Fig. 7 required a total of 10 parabolas to construct the boiling curve; this number varied among different cases. The heater power is incremented to higher level during the hypergravity phase before entering the microgravity period. An increase in wall temperature is observed during hypergravity in response to the power increase. Wall temperature then decreases in microgravity, indicating enhancement in flow boiling heat transfer, which will be elaborated upon in subsequent sections in relation to changes in flow structure between hypergravity and microgravity. With further increases in q'', the boiling process intensifies and wall temperatures attain higher steady-state values. At the last heater increment, wall temperature exhibits unsteady excursion, indicating CHF occurrence, upon which heater power is abruptly reduced to zero. Throughout the entire test, T_{in} is maintained constant, ensuring consistent inlet subcooling of $\Delta T_{sub,in} = 2.54$ K. Note that as the heater power is increased, pressure drop across the test section also increases, which causes $T_{f,out}$ to gradually decrease with time as more vapor is produced along the heated tube.

Table 2
Ranges of key parameters of the flight experiments.

Parameter	Range
Mass velocity, G	398.3 – 1342.8 kg/m^{2}s
Mass flow rate, $\dot{m}$	0.021 – 0.076 kg/s
Inlet pressure, p_{in}	413.68 – 689.48 kPa
Inlet temperature, T_{in}	88.77 – 94.96 K
Inlet subcooling, ΔT_{sc}	1.04 – 5.67 K
Inlet quality, $x_{e,in}$	−0.08 – −0.01
Wall heat flux, q''_w	0 – 106.3 kW/m^2
Outlet quality, $x_{e,out}$	−0.06 – 0.16

To achieve a more detailed understanding of the key parameter dynamics during parabolic flight maneuvers, refer to Fig. 8. This figure exhibits temporal variations of recorded two bottom wall temperatures, $T_{w,3,bot}$ and $T_{w,4,bot}$, inlet and outlet pressure, P_{in} and P_{out}, gravity level, g/g_e, and heat flux, q'', under the same operating condition as depicted in Fig. 7. Fig. 8(a) illustrates temporal variations of key parameters for low to intermediate heat flux conditions, encompassing a heat flux transition from 33.6 kW/m^2 to 48.7 kW/m^2. Simultaneously, the two sets of cyclic variations of gravity level are also depicted in the figure. Notice the escalation in heat flux during the hypergravity phase prior to entering the microgravity phase. Focusing on the evolution of wall temperatures, a series of transient-to-steady behavior is evident in response to varying gravity and heat flux. Initially, at a stable state during the hypergravity period at $t = 280$–300 s, both wall temperatures decrease as gravity transitions to microgravity, where they promptly stabilize during the microgravity phase. Upon reentering a hypergravity phase, with an increase in heater power and in conjunction with varying gravity levels, the wall temperatures rise, attaining another stable temperature promptly before moving into the subsequent microgravity phase. Subsequently, as the aircraft shifts to a nose-dive position to create microgravity again, the wall temperatures decrease and reach steady state. Based on the analyzed transient behavior, it is evident that the wall temperatures successfully reached and maintained steady state during the microgravity periods. Fig. 8(b) demonstrates temporal variations of key parameters at high heat flux conditions, encompassing a heat flux transition from 77.8 to 88.3 and to 94.5 kW/m^2. A similar series of transient-to-steady dynamics continues in response to varying heat flux and gravitational acceleration. Here too, stable steady state wall temperatures were successfully achieved and maintained throughout the microgravity periods. Furthermore, notice the consistently maintained inlet pressure in both heat flux regions, Figs. 8(a) and 8(b). The steady inlet pressure represents stable inlet subcooling and mass flow rate since all three parameters are mutually coupled influenced by each other.

3.2.1. Flow patterns for low mass velocities

Fig. 9 shows flow visualization results captured in microgravity for three different sets of operating conditions corresponding to the lower range of mass velocity tested, with the flow direction from left to right. As explained earlier, all the presented flow visualization results are captured from the adiabatic visualization section which is located just downstream from the uniformly heated test section. Included for each set of operating conditions are high-speed video images recorded at steady state for indicated increasing values of heat flux from above onset of boiling (ONB) until (and including) CHF. Wall heat flux, q'', is indicated either as kW/m^2 value where CHF could not be reached, Fig. 9(a), or as percentage of q''_{CHF}, which is defined as

$$\%\ CHF = \frac{q''_{meas}}{q''_{CHF}} \times\ 100\ [\%] \quad (9)$$

Fig. 9(a) exhibits two-phase flow structure and flow patterns captured for $G = 400$ kg/m^{2}s, $P_{in} = 689.5$ kPa, $\Delta T_{sub\ in} = 5.39$ K, and four heat fluxes. The objective in presenting this figure is to investigate the flow regime transitions for a combination of low mass and low heat

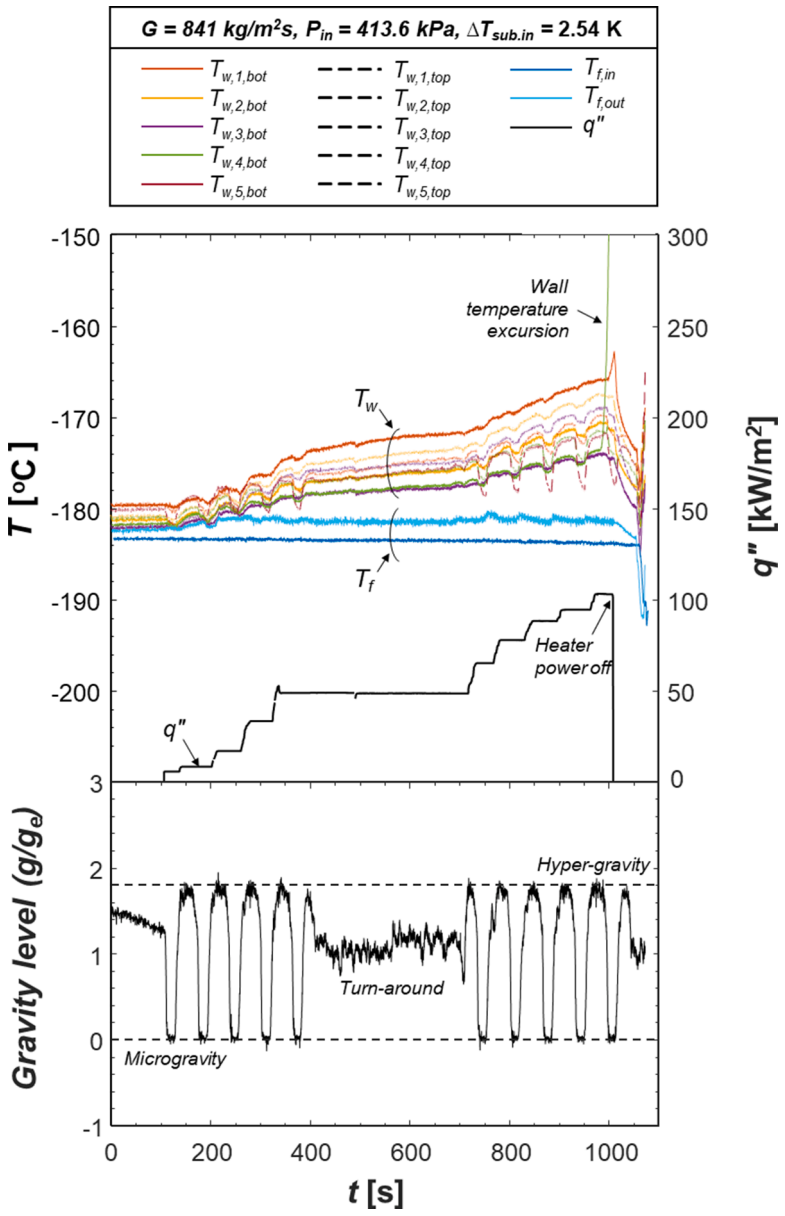

Fig. 7. Temporal variations of key system parameters in response to heat flux increments from zero to CHF for a set of operating conditions.

fluxes. For $q'' = 2.76$ kW/m^2, the wall superheat exceeds the superheat required for bubble nucleation within the upstream heated test section, evidenced by passage of multiple small bubbles along the adiabatic glass tube. Because of small surface tension of cryogens, including LN_2, nucleated bubbles can easily detach from the heated wall, despite their small size. The flow pattern for $q'' = 2.76$ kW/m^2 is one of well-dispersed bubbly flow, with bubbles scattered almost uniformly throughout the adiabatic glass tube. The bubbles vary from small grain-like spherical to those a few millimeters in diameter. The larger bubbles are more deformed in the flow direction due flow inertia despite the relatively low mass velocity. Overall, bubble distributions both across and along the adiabatic glass tube appear independent of bubble size, result of absence of body force in microgravity. At $q'' = 4.21$ kW/m^2, bubbles become larger due to higher wall superheat activating a greater number of nucleation sites on walls of the upstream heated tube, as well as to increased collision frequency promoting appreciable coalescence. Clearly captured for this heat flux are oblong bubbles which appear to coalesce together while traveling along the adiabatic glass tube. Absence of gravity is reflected in axisymmetric distribution with no stratification towards either side of the wall. With a slight increase of heat flux to $q'' = 5.59$ kW/m^2, there is a substantial increase in both vapor void fraction and size of coalescent bubbles, culminating is very long cylindrical bubbles with spherical front, comprising mostly the central portion of the cross-section, surrounding by an annular liquid layer. This interfacial behavior mimics closely one observed in slug flow along a vertical tube in Earth gravity. Red arrows in Fig. 9(a) indicating spherical fronts of the individual long bubbles, which are very evident for the right most and middle bubbles. Notice also how the front of the left most bubble is coalescing with the trailing edge of the middle bubble, outcome of both high void fraction and liquid recirculation behind the trailing edge. High velocity difference between the central vapor bubbles and surrounding liquid are shown producing noticeable disturbance to the interface in between. At $q'' = 11.26$ kW/m^2, a further increase in vapor void fraction is shown merging the previously discrete long bubbles into a thick continuous vapor core along with formation of a thin annular film along the walls; this annular flow pattern spans the entire length of the adiabatic glass tube. Large velocity difference between the fast-moving vapor core and slower annular liquid film can potentially induce

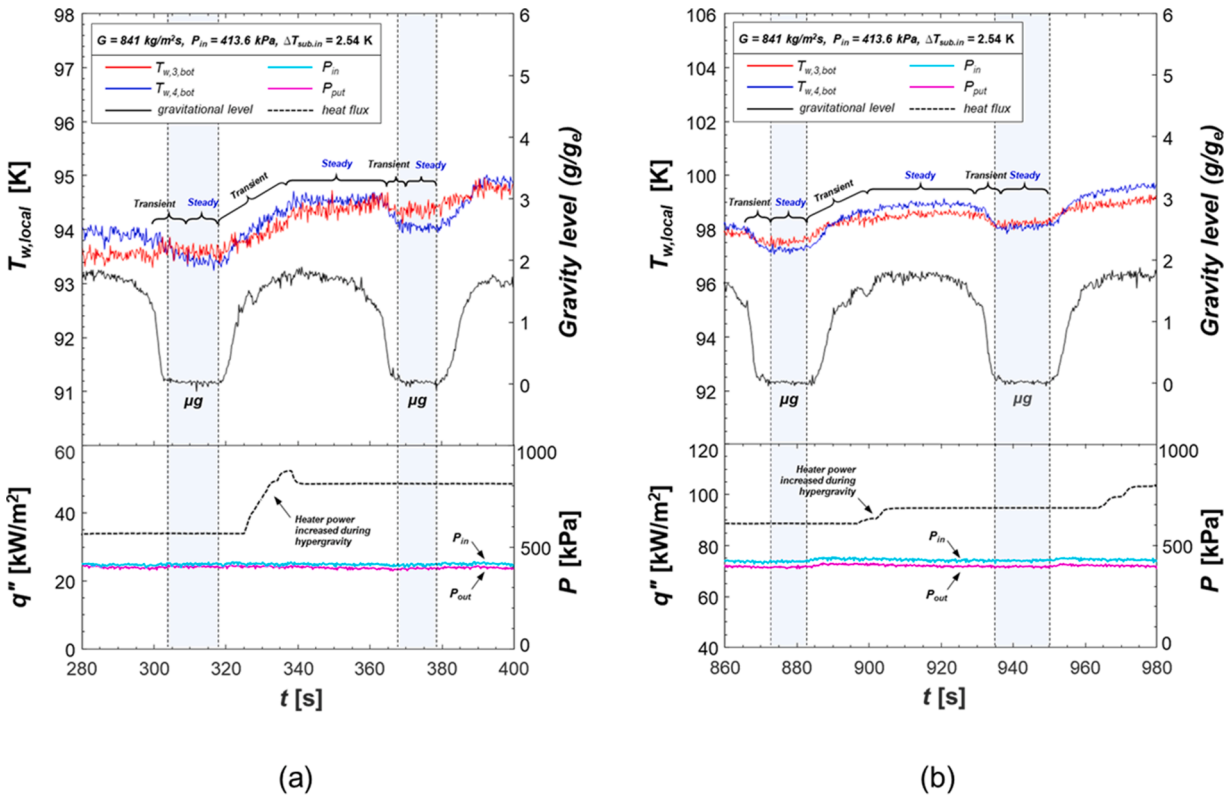

Fig. 8. Temporal variations of key system parameters in response to heat flux increments at (a) low heat fluxes and (b) high heat fluxes for a set of operating conditions during parabolic flight experiment.3.2 Flow Visualization under Microgravity.

instability along the interface in between. For an imposed interfacial perturbation of wavelength λ along a horizontal interface between a vapor layer at velocity $\overline{u}_g$ and a liquid layer at velocity $\overline{u}_f$ in Earth gravity, with liquid situated beneath the vapor, instability will occur when the velocity difference satisfies the relation [41]

$$\left|\overline{u}_g - \overline{u}_f\right| > \left\{ \frac{\left[\sigma\left(\frac{2\pi}{\lambda}\right) + \frac{(\rho_f - \rho_g)g_e}{\left(\frac{2\pi}{\lambda}\right)}\right](\rho_f + \rho_g)}{\rho_f \rho_g} \right\}^{1/2} \tag{10}$$

Eq. (10) shows instability will occur when the inertia resulting from the velocity difference exceeds combined effects of surface tension and gravity. In microgravity, however, with $g \sim 0$, Eq. (10) can be simplified into the form

$$\left|\overline{u}_g - \overline{u}_f\right| > \left\{ \frac{\sigma\left(\frac{2\pi}{\lambda}\right)(\rho_f + \rho_g)}{\rho_f \rho_g} \right\}^{1/2} \tag{11}$$

which implied the instability is dominated entirely by a balance between the destabilizing effect of inertia and counter stabilizing effect of surface tension. Because of very low surface tension of cryogenic fluids, including LN_2, compared to conventional room-temperature fluids such as water, the interface would require smaller phase velocity difference to induce the instability. In other words, cryogenic flows in microgravity are more susceptible to interfacial instability. This behavior is captured in Fig. 9(a) for $q'' = 11.26$ kW/m^2, in the form of both appreciable instabilities in the interface between vapor core and annular liquid film as well as breakup of droplets from liquid crests of the wavy interface which are entrained into the vapor core. In the captured image, short and darker spots within the brighter vapor core indicate entrained droplets or liquid ligaments which are expected to influence heat transfer in the annular flow regime.

Fig. 9(b) depicts flow patterns up to and including CHF for $G = 547$ kg/m^{2}s, $P_{in} = 551.6$ kPa, and $\Delta T_{sub,in} = 2.93$ K. Here, because CHF is captured during experiment, lower heat flux conditions are given as percentage of the measured CHF. At 13 % CHF, active bubble nucleation occurs in the upstream heated tube and departed bubbles drift towards the core in the adiabatic glass tube. Migrated and accumulated bubbles are shown actively coalesced into discrete, oblong vapor structures. Absent body forces, these vapor structures float along the central core without stratification. At 27 % CHF, the elongated vapor structures merge together spanning the entire length of the adiabatic glass tube, indicating transition to annular flow. At 51 % and 76 % CHF, with increasing vapor quality, vapor core grows thicker pushing the liquid film towards the tube wall. The ensuing gradual thinning of the annular liquid film is further accentuated by continuous droplet entrainment into the vapor core, brought about by aforementioned interfacial instability. At CHF, liquid layer thickness remarkably attenuates, increasing the likelihood of partial dryout of liquid layer in the upstream heated tube and direct exposure of heated tube wall to the vapor core. This is deemed the obvious reason behind CHF occurrence, which is confirmed by a sudden unsteady excursion in the temperature of the heated tube.

Fig. 9(c) depicts flow patterns up to and including CHF for $G = 696$ kg/m^{2}s, $P_{in} = 482.6$ kPa, and $\Delta T_{sub\ in} = 1.23$ K. Here, increased mass velocity compared to the cases in Fig. 9(a) and 9(b), further compromises the resolution of video capture, albeit with similar flow pattern progression observed with increasing heat flux. With a larger heat flux range and greater CHF for this higher mass velocity case, more intermediate cases are captured and depicted in Fig. 9(c). At 4 % CHF, the entire upstream heated tube is under subcooled boiling state having outlet quality lower than unity, but the higher wall temperature is

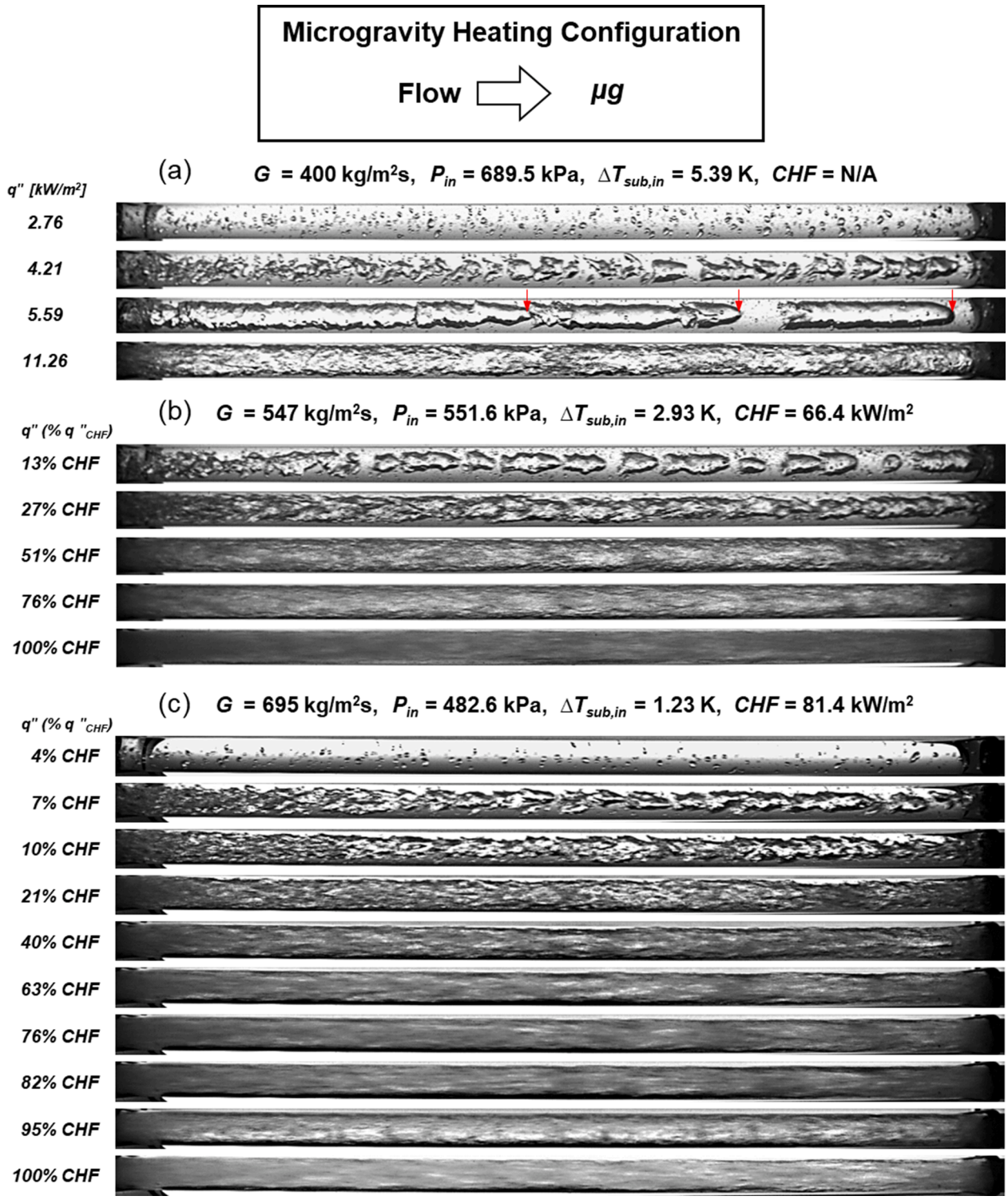

Fig. 9. Two-phase flow structure development along the boiling curve for near-saturated inlet at mass velocities of G = (a) 400, (b) 547, and (c) 695 kg/m^{2}s.

sufficiently superheated to initiate bubble nucleation. The images in Fig. 9(c) for this heat flux are ones observed in the adiabatic glass tube. Here, droplets varying is size are shown well dispersed in the liquid flow. At 7 % and 10 % CHF, with increased wall superheat in the upstream heated tube, a greater number of bubbles are generated which coalesce into the larger vapor structures captured in the adiabatic glass tube. At 21 % CHF, annular flow prevails along entire length of the adiabatic glass tube. Noticeable here are the drastic changes in flow structure and rapid transition to annular flow occurring over a relatively narrow heat flux range. This behavior is attributed to small latent heat of vaporization, h_{fg}, and surface tension, σ, causing higher frequency nucleation of smaller bubbles when compared to room-temperature fluids such as water. From 40 % to 90 % CHF, the annular flow regime persists but with decreasing liquid film thickness. Due to low h_{fg}, cryogens in general, including LN_2, sustain bubble nucleation even within the annular liquid film; this is observed in Fig. 9(c) for all heat flux between 40 % CHF and CHF. As heat flux increases, due to increasing vapor content, captured images become brighter near the wall implying lesser liquid.

3.2.2. Flow patterns for intermediate mass velocities

Fig. 10 shows flow visualization results for three sets of operating conditions with intermediate mass velocities. Fig. 10(a) exhibits interfacial behavior at steady state for increasing values of heat flux for G = 743 kg/m^{2}s, P_{in} = 482.6 kPa, and $\Delta T_{sub,in}$ = 3.61 K, conditions that did not reach CHF value. Due to the higher mass velocity compared to conditions captured in Figs. 9(a) and 10(a) exhibits lower void fraction. For example, in Fig. 10(a), with q'' = 8.46 kW/m^2, one can see dispersed

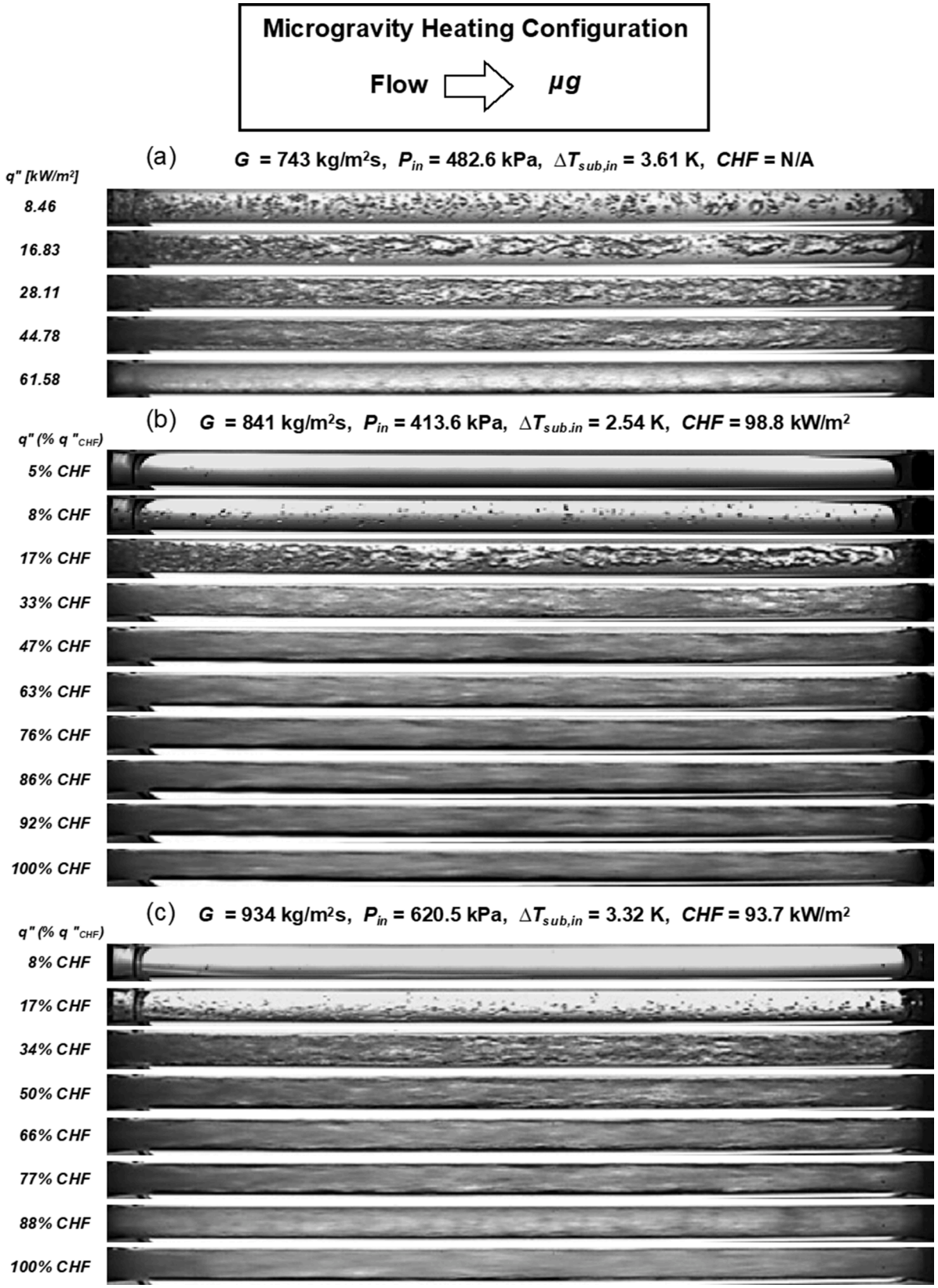

Fig. 10. Two-phase flow structure development along the boiling curve for near-saturated inlet at mass velocities of G = (a) 743, (b) 841, and (c) 934 kg/m^{2}s.

bubbly flow whereas in Fig. 9(a) with $q'' = 5.59$ kW/m^2, the flow has already transitioned to one dominated by elongated bubble structures. At $q'' = 16.83$ kW/m^2, with the increased wall superheat activating more nucleation cavities in the upstream heated tube, Fig. 10(a) captures bountiful large oblong bubbles flowing into the adiabatic glass tube. In the absence of boiling within the adiabatic glass tube, both mixing and turbulent effects are abated, which allow the oblong bubbles from the heated tube to merge into yet longer bubbles. And absent gravity, the long vapor bubbles are clustered around the central axis with no propensity to stratify within the tube's cross-section. At $q'' = 28.11$ kW/m^2,

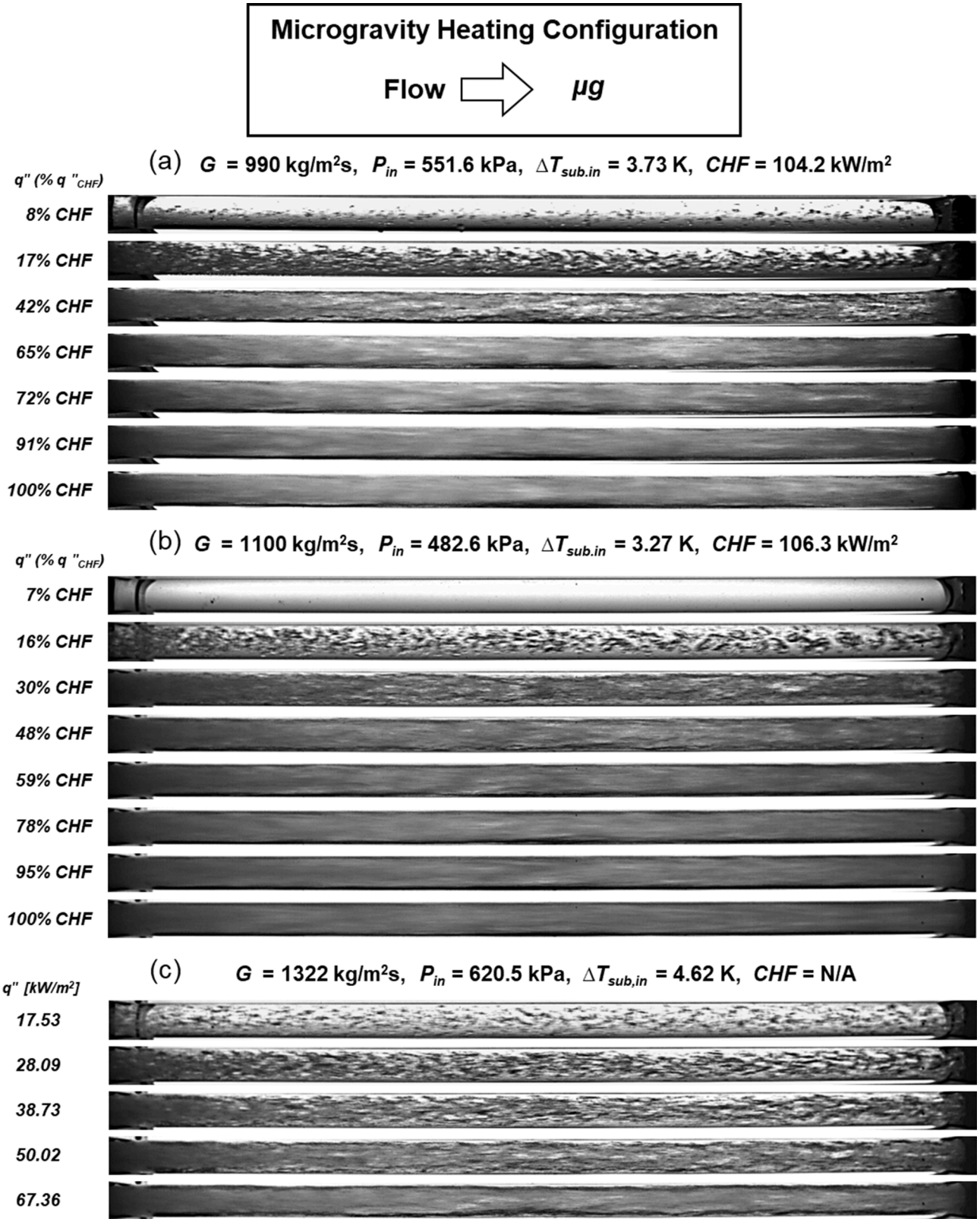

Fig. 11. Two-phase flow structure development along the boiling curve for near-saturated inlet at mass velocities of G = (a) 990, (b) 1100, and (c) 1322 kg/m^{2}s.

vapor structures grow both axially and radially and are fully jointed into one axially continuous vapor core, indicating the flow has transitioned to annular. At $q'' = 44.78$ kW/m^2, annular flow persists with a central vapor core surrounded by an annular liquid film. Careful inspection of this image shows small bubbles nucleating within and entrained along the annular liquid film. This is an obvious departure in annular flow structure for LN_2 as compared to room-temperature fluids and points to heat transfer benefits for LN_2 aside from liquid film evaporation alone. This persistent bubble nucleation in annular flow was also captured in high-speed visualization images from LN_2 chilldown experiments by Baek et al. [46], as well as recent 1-g_e horizontal LN_2 flow boiling experiments conducted by the present authors [42] using the same experimental payload as in the present study. At $q'' = 61.58$ kW/m^2, the liquid film, while continuing to cover the inner wall of the entire adiabatic glass tube, is now much thinner, evidenced by better backlight transmission and overall brighter image than those captured at lower heat fluxes. In the captured image, interspersed darker regions appear periodically, which represent crests (thick film portions) of the brighter long interfacial waves.

Fig. 10(b) illustrates interfacial structure for steady state conditions corresponding to heat flux increments up to and including CHF for $G =$ 841 kg/m^{2}s, $P_{in} = 413.6$ kPa, and $\Delta T_{sub,in} = 2.54$ K. At 5 % CHF, within the adiabatic glass tube, a few tiny bubbles are captured within the inlet region, remnants of mild subcooled boiling originating from the upstream heated tube. High-speed video showed the same bubbles to vanish altogether downstream in a few milliseconds by recondensing back to liquid. With slight increase of heat flux to 8 % CHF, a corresponding increase in wall superheat within the upstream heated tube activates a greater number of cavities and produces large number of bubbles which are shown as dispersed bubbly flow within the adiabatic glass tube. At 17 % CHF, numerous larger sized bubbles are entering the adiabatic glass tube. Closer inspection of this image shows incoming vapor bubbles clustering towards the core. With attenuating turbulent mixing in the adiabatic glass tube, aggregated bubbles in the core gradually merge into larger and longer vapor structures. From 33 % to 63 % CHF, annular flow is fully developed with the liquid film thickness getting thinner with increasing heat flux. From 76 % CHF to CHF, there are no observable features for the different heat fluxes due to fast vapor core motion with intermittent dark regions indicative of annular liquid film crests. Notice the higher CHF value when compared to cases in Fig. 9 due to increased mass velocity for the former.

Fig. 10(c) captures interfacial structure for a series of heat flux increments up to and including CHF for $G = 934$ kg/m^{2}s, $P_{in} = 620.5$ kPa, and $\Delta T_{sub,in} = 3.32$ K. Here, flow pattern transitions are similar to those captured for the low mass velocities but with lower void fraction for a given heat flux. For example, at 17 % CHF, Fig. 10(c) depicts a bubbly flow regime consisting of small, dispersed bubbles compared to large oblong bubbles for 17 % CHF in Fig. 10(b). Transition to annular flow is also delayed to high heat flux with the increased mass velocity. For example, annular flow is delayed to 50 % CHF for $G = 934$ kg/m^{2}s, Fig. 10(c), compared to 21 % CHF for $G = 695$ kg/m^{2}s, Fig. 9(c).

3.2.3. Flow patterns for high mass velocities

Fig. 11 shows flow visualization results for relatively high mass velocities. Here, flow pattern progression until CHF is similar to those captured for lower mass velocities and depicted in Figs. 9 and 10 except for a reduction in amount of vapor produced. Due to the high mass velocity, bubble nucleation is delayed to higher power input. For example, Fig. 11(b) shows single phase liquid flow prevailing at 7 % CHF with no bubbles entering the adiabatic glass tube. Here, even smaller discrete bubbles are stretched axially because of high flow inertia. Increasing the heat flux increases bubble populations in the adiabatic glass tube but because of strong turbulence mixing and flow inertia, bubble coalescence is suppressed, which is evidenced by chaotic bubbly flow (churn-like) clearly visible at 16 % CHF for $G = 1100$ kg/m^{2}s, Fig. 11(b), compared to one comprised of large oblong bubbles at 13 % CHF for $G =$ 547 kg/m^{2}s, Fig. 9(b). Also clearly apparent is that the high mass velocities in Fig. 11 are associated with rapid transition from bubbly to annular flow, bypassing altogether the large oblong bubble regime captured at the lower mass velocities in Figs. 9 and 10. However, bubble nucleation in the annular liquid film still persists for the highest mass velocity tested.

3.2.4. Flow visualization image sequences for low mass velocity

Fig. 12 provides high speed video image sequences for $G = 400$ kg/m^{2}s, $P_{in} = 689.5$ kPa, $\Delta T_{sub,in} = 5.39$ K, and four wall heat fluxes of $q'' =$ 2.76, 4.21, 5.59, and 11.26 kW/m^2. The images in each sequence are 15 ms apart.

In Fig. 12(a), with a heat flux of $q'' = 2.76$ kW/m^2, indicated with red arrows is a cluster of bubbles flowing from the upstream heated tube into the adiabatic glass tube are tracked with time. From the first image to the second, bubbles are approaching each other as distance in between decreases. Between the second image and third, congregated bubbles begin to collide. The colliding bubbles do not merge with each other but bounce away as captured in the third image. From the fourth image to the fifth, dispersed bubbles interact with surrounding bubbles and, once again, aggregate and collide. After the collision, from the sixth image to the seventh, bubbles disperse away from each other. The chain reaction of collision and dispersion of bubbles is repeated and prevalently observed via video. The observed behavior is very consistent with a hypothesis by Sharma et al. [47] who formulated the concept of "bubble collision dispersion force." He showed this force causes colliding or densely packed small bubbles to repel from one another resulting in well distributed bubble concentration across the flow area of the tube. The bubble collision dispersion force has been adapted in recent computational flow boiling simulations [36,47,48] and validated against experimental data. Effect of bubble collision dispersion force on flow structure was also visually captured in 1-g_e horizontal LN_2 flow boiling experiments by the present authors [42] who observed small bubbles suddenly dispersing after aggregation. This behavior is similar to one captured in the present microgravity experiments which culminates in a well-dispersed, almost uniform distribution of bubbles along the adiabatic glass tube, whereas in a horizontal tube in Earth gravity there is propensity for bubbles to stratify toward the top wall by buoyancy.

In Fig. 12(b), with a higher heat flux of $q'' = 4.21$ kW/m^2, nucleated bubbles grow larger on the wall of the of upstream heated tube and effective coalescence among bubbles produces even larger bubbles. Correspondingly, at the inlet of the adiabatic glass tube, compared to Fig. 12(a), a series of large bubbles can be observed. With time, incoming initially separated bubbles, marked by red boxes, merge into yet longer vapor structures. It is important to note that effectiveness of bubble merging following collision increases with increasing void fraction. Note that impact of the bubble collision dispersion force, which is very pronounced for clusters of small, dispersed bubbles, Fig. 12(a), diminishes appreciably for larger bubbles [42]. This may explain the fundamental differences in bubble merging characteristics for very small bubbles, Fig. 12(a), compared to those of large bubbles, Fig. 12(b).

In Fig. 12(c), with a yet higher heat flux of $q'' = 5.59$ kW/m^2, coalescence continues, here between very long bubbles. Red arrows indicate upstream front of a long bubble approaching and eventually colliding and merging with another oblong bubble ahead. An interesting outcome of the merging is indicated with blue arrows. During the bubble infusion process, as trailing bubble crashes into tail of leading bubble, vapor inside the trailing bubble, facing the impact force, is momentarily decelerated, which is evidenced by a transverse wave forming along interface of the trailing bubble, which propagates opposite to the flow direction for a brief duration before fading away.

In Fig. 12(d), with heat flux of $q'' = 11.26$ kW/m^2, about twice as that of Fig. 12(c), merging among long bubbles is now complete and the flow transitions to annular flow, comprised of fast vapor core surrounded by slow moving annular liquid film. As discussed earlier, interfacial

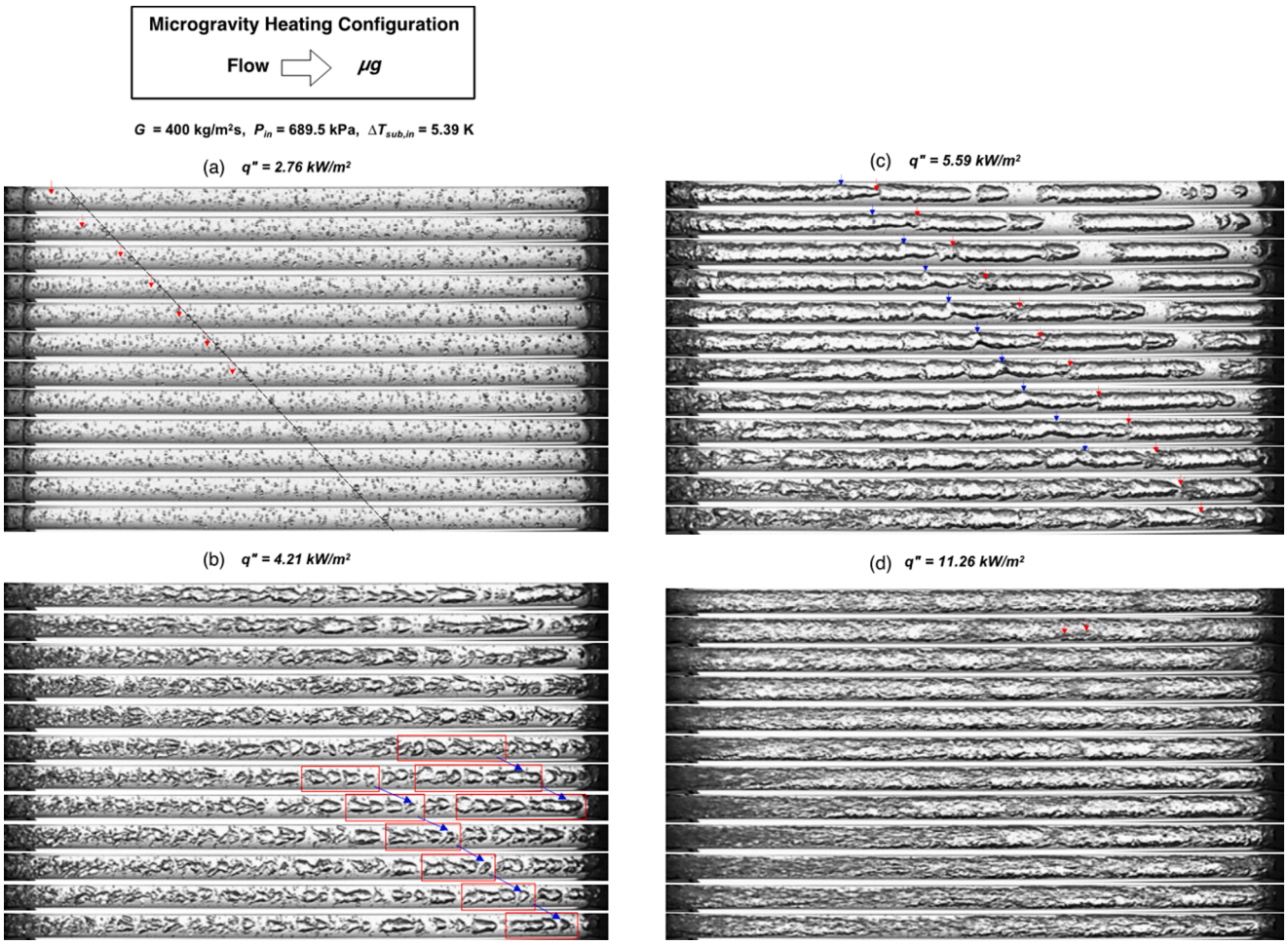

Fig. 12. Flow visualization image sequences for near-saturated inlet, mass velocity of $G = 400$ kg/m^{2}s, and $q'' =$ (a) 2.76 kW/m^2, (b) 4.21 kW/m^2, (c) 5.59 kW/m^2, and (d) 11.26 kW/m^2.

instability is shown inducing appreciable waviness in the liquid film's interface, coupled with shattering of droplets from wave crests generating liquid droplets that are entrained into the vapor core. Additionally, as indicated with red arrows in the second image, because of strong interfacial shear resulting from large velocity difference between vapor core and liquid film, potentially larger amounts of liquid are scooped up into the vapor core in form of liquid ligaments that are disconnected from the annular liquid film and captured amid the vapor core.

3.2.5. Flow visualization image sequences for high mass velocity

Fig. 13(a)–(d) include high speed image sequences for $G = 1300$ kg/m^{2}s, $P_{in} = 620.5$ kPa, $\Delta T_{sub,in} = 4.62$ K, and four heat fluxes of $q'' = 17.53$, 28.09, 38.73, and 50.02 kW/m^2. The images in each sequence are 15 ms apart. Due to much higher flow velocity under high mass velocity, captured image sequences are blurred due to limitations of the video camera. Nevertheless, important aspects of the interfacial structure and flow physics are still discernable.

In Fig. 13(a), with $q'' = 17.53$ kW/m^2, captured flow structure along the adiabatic glass tube is clearly bubbly, dominated by abundance of well dispersed small discrete bubbles. But, unlike the lower mass velocity cases in Fig. 12, vapor bubbles in Fig. 13(a) are stretched in flow direction because of stronger interfacial shear. Notice also how the discrete bubbly regime is maintained at a much higher heat flux than that for Fig. 12(a).

Fig. 13(b) shows image sequences for higher wall heat flux of $q'' =$ 28.09 kW/m^2. Here, bubbles, still comparatively small, grow larger and longer but have not culminated in a continuous vapor core. Note that this heat flux is nearly seven times larger than that of Fig. 12(b), which was dominated by very large oblong bubbles; flow pattern in Fig. 13(b) is dispersed bubbly. In Fig. 13(c), with $q'' = 38.73$ kW/m^2, bubbles are appreciably larger and densely packed along the core. And in Fig. 13(d), with $q'' = 50.02$ kW/m^2, flow transitions to annular, with thick vapor core surrounded by annular liquid film. Large velocity differences between the vapor core and liquid film are shown causing significant waviness along the film's interface. Additionally, tiny vapor bubbles are entrapped within the annular liquid film, evidence of persistent bubble nucleation within the annular liquid film in the upstream heated tube under high mass velocity.

3.3. Gravitational effects on flow structure

3.3.1. Flow pattern comparison for microgravity and hypergravity

Fig. 14 shows images captured in microgravity and hypergravity for identical flow conditions. Fig. 14(a) compares flow patterns for $G = 743$ kg/m^{2}s, $P_{in} = 482.6$ kPa, $\Delta T_{sub,in} = 3.61$ K, and four different wall heat flux conditions of $q'' = 16.83$, 28.11, 44.78, and 61.58 kW/m^2. At $q'' =$ 16.83 kW/m^2 and adequate wall superheat, in microgravity, large oblong vapor bubbles enter the adiabatic glass tube and gradually merge into yet longer bubbles. Absent gravity, there is obvious flow symmetry, with the long bubbles moving along the centerline of the tube with no signs of stratification. In contrast, for same operating conditions, interfacial structure captured in hypergravity is categorically different, dominated by a plug flow pattern. First, incoming bubbles are much smaller. Here, strong buoyancy causes stronger and earlier detachment

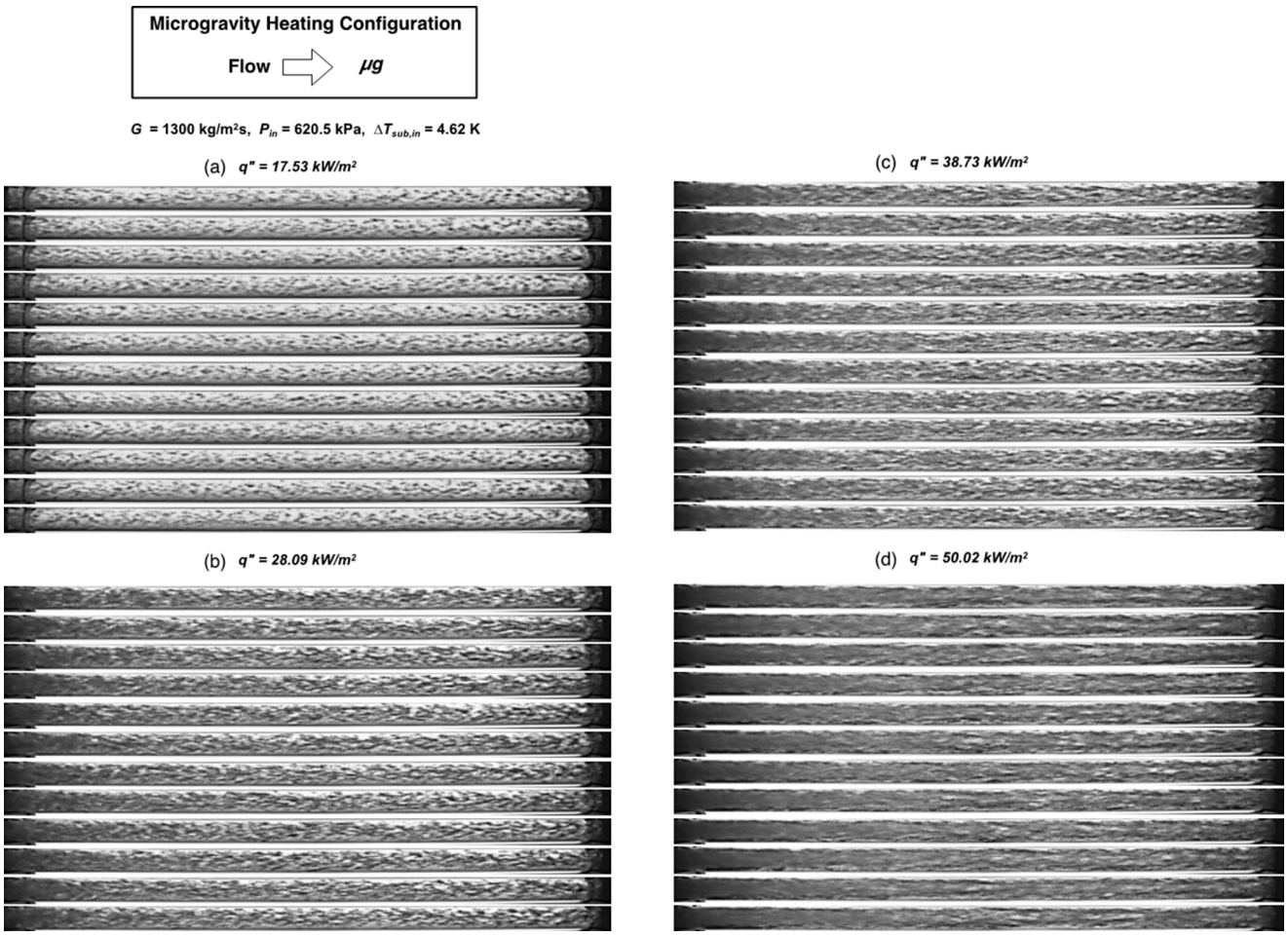

Fig. 13. Flow visualization image sequences for near-saturated inlet, mass velocity of $G = 1300$ kg/m^{2}s, and $q'' =$ (a) 17.53 kW/m^2, (b) 28.09 kW/m^2, (c) 38.73 kW/m^2, and (d) 50.02 kW/m^2.

of bubbles from the bottom of the upstream horizontal heated tube, coupled with distinct migration and accumulation toward the top of the tube. This behavior continues into the adiabatic glass tube as captured in Fig. 14(a). Additionally, buoyancy compresses the coalescent bubbles in the transverse direction, causing them to stretch axially into thin, long formations. And, overall, vapor void fraction in hypergravity is much smaller than in microgravity. At $q'' = 28.11$ kW/m^2, in microgravity, with increased vapor generation within the upstream heated tube, large oblong bubbles exhibit appreciable merging, albeit with symmetry about the central axis. In contrast, in hypergravity, stratification causes thin vapor formations arriving from the upstream heated tube to merge along the adiabatic glass tube into a thin continuous vapor layer pressed against the top. At $q'' = 44.78$ kW/m^2, annular flow is fully established in microgravity, with a thick central vapor core surrounded by a thin annular liquid film, with the flow displaying symmetry about the central axis. In contrast, in hypergravity, the flow is distinctly stratified annular, with a thick vapor layer adjoining the top and heavier liquid flowing underneath, but with a thin liquid layer dragged above the vapor. Similar differences are captured between the two gravitational environments are captured at $q'' = 61.58$ kW/m^2, with the primary difference compared to the case of $q'' = 44.78$ kW/m^2 being greater vapor content. In microgravity, as indicated by a brighter image and a thin liquid film, a high void fraction can be implied.

Fig. 14(b) compares interfacial structure for operating conditions with $G = 1100$ kg/m^{2}s, $P_{in} = 482.6$ kPa, $\Delta T_{sub,in} = 3.27$ K, and four wall heat fluxes of $q'' = 16.62$, 50.90, 66.65, and 112.21 kW/m^2. Similar characteristics in terms of impact of body force are observed as in Fig. 14 (a) but with some differences. At $q'' = 16.62$ kW/m^2, a clear discrepancy in bubble size is found among the two gravities. In hypergravity, incoming bubbles arriving from the upstream heated tube are tiny grain-like having departed from the heated wall much faster, because of higher mass velocity, and without having sufficient time of appreciable growth. In addition, bubbles in hypergravity are carried up toward the top but, because of strong axial inertia caused by the higher mass velocity, are less stratified than for the lower mass velocity, Fig. 14(a). At $q'' = 112.21$ kW/m^2, with an increased flow velocity because of greater vapor content, stratification in hypergravity is greatly abated, evidenced by a tendency toward symmetrical annular flow for both gravities.

3.3.2. Flow patterns for Lunar and Martian gravities

Subtle maneuvering of the aircraft can produce Lunar(0.18 g_e) and Martian(0.39 g_e) gravities, which were achieved in the present study for a subset of operating conditions. Fig. 15 presents interfacial behavior captured in these reduced gravities the flow patterns for $G = 766$ kg/m^{2}s, $P_{in} = 551.6$ kPa, and $\Delta T_{sub\ in} = 2.18$ K at three different wall heat fluxes. For $q'' = 8.2$ kW/m^2, only Lunar gravity conditions are achieved. Captured bubble size is smaller than that in microgravity, Fig. 10(a), due to earlier, albeit weak Lunar buoyancy assisted bubble departure from the heated wall from the upstream heated tube. However, due to small size of bubbles and weak buoyancy in Lunar gravity, bubbles appear well dispersed across the flow area with no discernible migration toward the top. With an increase in the wall heat flux to $q'' = 16.9$ kW/m^2, both Lunar and Martian gravities are achieved. For both gravities, large bubbles from the upstream heated tube can be seen entering the adiabatic glass tube and merging into yet larger vapor structures toward the centerline. Despite seemingly identical interfacial behavior for both

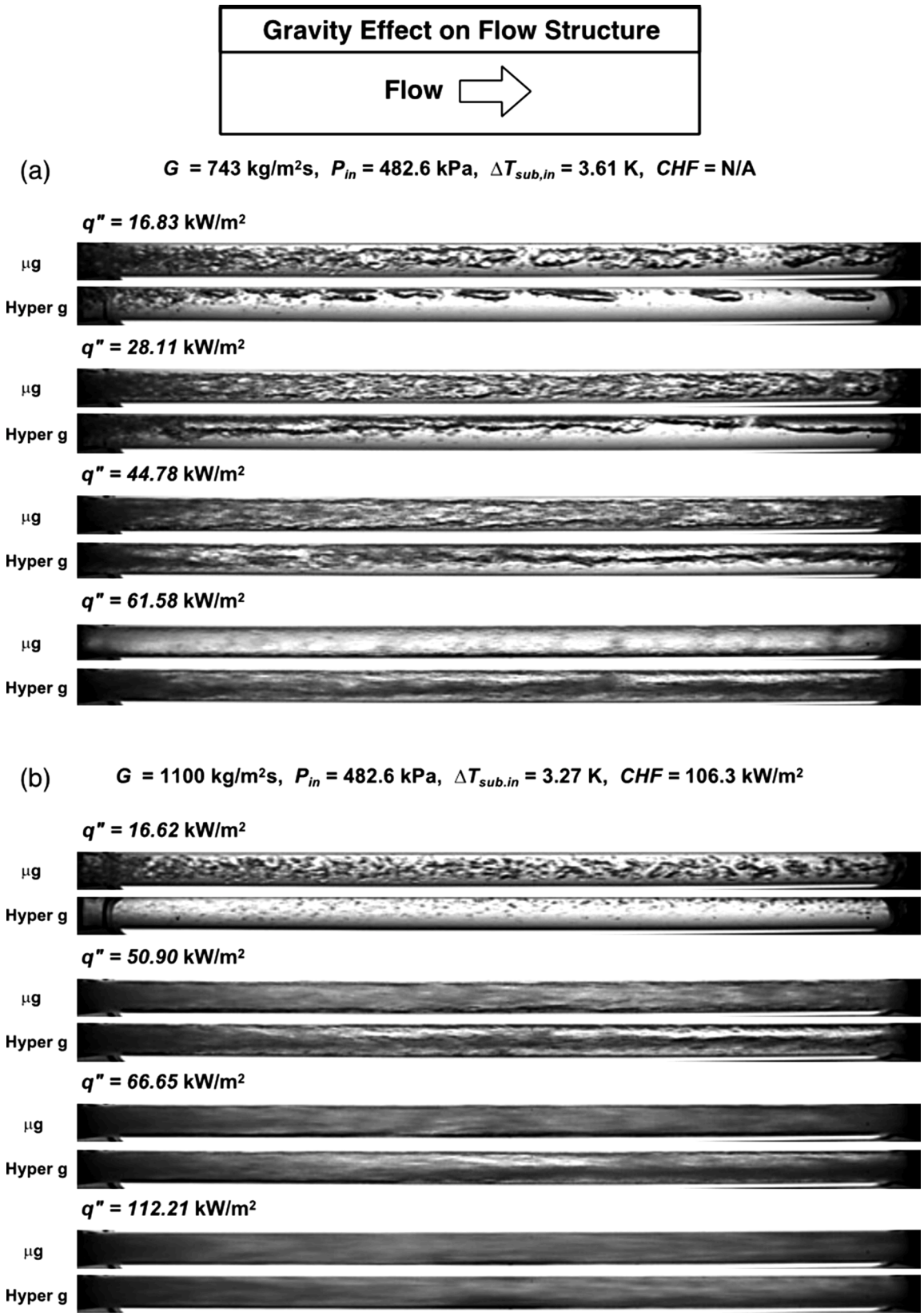

Fig. 14. Effects of gravity on two-phase flow structure for near-saturated inlet with (a) mass velocity of $G = 743$ kg/m^{2}s and heat fluxes of $q'' = 16.83$, 28.11, 44.78, and 61.58 kW/m^2, and (b) mass velocity of $G = 1100$ kg/m^{2}s and heat fluxes of $q'' = 16.62$, 50.90, 66.65, and 112.21 kW/m^2.

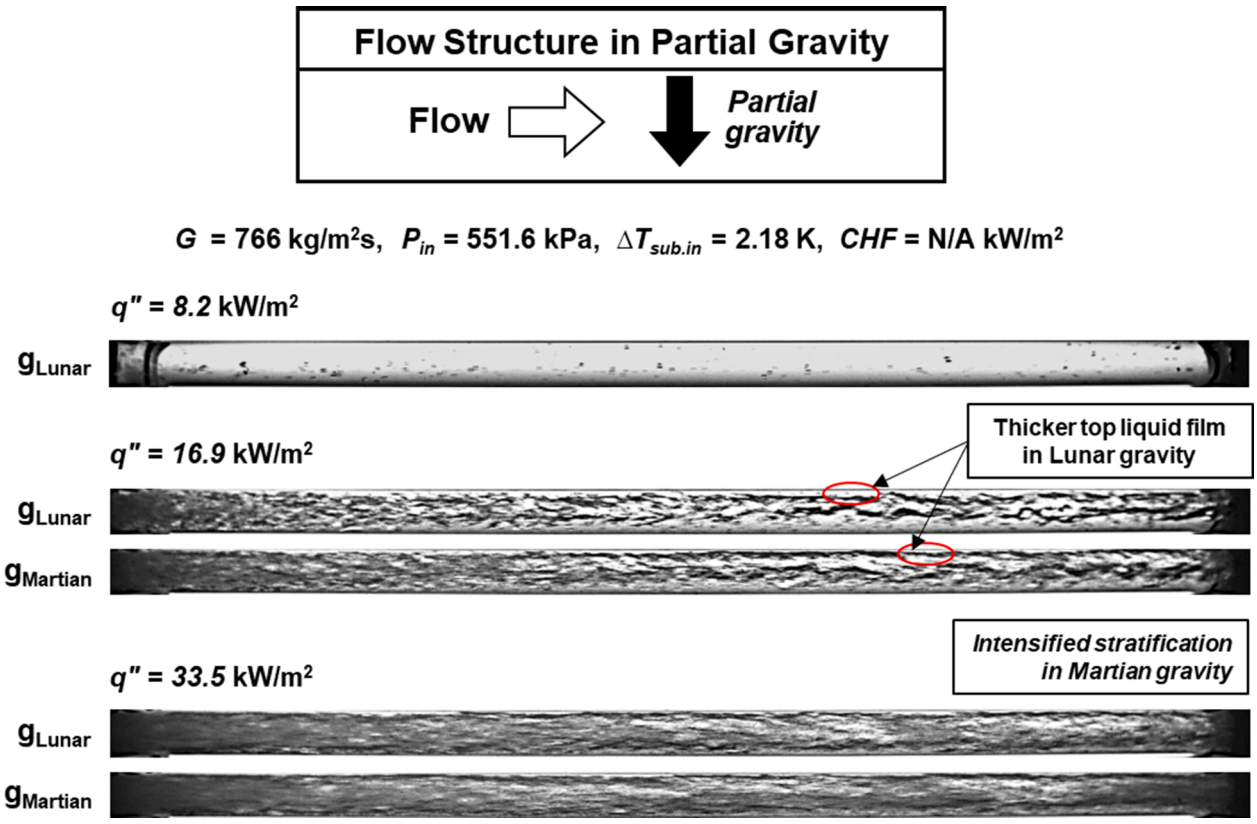

Fig. 15. Two-phase flow patterns in Lunar gravity and Martian gravity for near-saturated inlet, mass velocity of $G = 766$ kg/m^{2}s, and different heat fluxes.

gravities, there is minor shift of elongated vapor structures from the central axis in the weaker Lunar gravity, compared to more obvious stratification in Martian gravity, with the large vapor structures tending toward the top, which also causes thinning of the liquid layer trapped atop as indicated by red ellipses in the two images. At $q'' = 33.5$ kW/m^2, with more vapor generation and aggressive merging of vapor structures, flow patterns in Lunar and Martian gravities appear annular with only mild stratification as fast fluid motion and high inertia serve to symmetrize the flow structure. One subtle difference is that the annular liquid film appears more symmetrical for the weaker Lunar gravity.

3.3.3. *Flow regime transitions in microgravity*

Flow regime map is one of the popular methods to visualize the regime transition. Since the observed microgravity flow patterns, discussed in previous sections, are similar to those observed in vertical upflow from Earth based experiments, vertical upflow regime map is selected for the comparison. Taitel et al. [49] formulated a flow regime map for vertical upflow and proposed a semi-theoretical model outlining regime transition curves for air-water mixture flow. The model was selected for the comparison due to the improved generality achieved by the theoretical formulation. Eqs. (12) – (16) provides the relations developed by Taitel et al. [49] for dispersed bubbly to bubbly, bubbly to slug, slug to churn, and churn to annular, respectively.

$$j_f + j_g = 4.0\left[\frac{D^{0.429}(\sigma/\rho_f)^{0.089}}{\nu_f^{0.072}}\left(\frac{g(\rho_f-\rho_g)}{\rho_f}\right)^{0.446}\right] \tag{12}$$

$$j_f = 3.0 j_g - 1.15\left(\frac{\sigma g(\rho_f-\rho_g)}{\rho_f^2}\right)^{1/4} \tag{13}$$

$$\frac{L_H}{D} = 40.6\left(\frac{j_f+j_g}{\sqrt{gD}} + 0.22\right) \tag{14}$$

$$\frac{j_g\rho_g^2}{[\sigma g(\rho_f-\rho_g)]^{1/4}} = 3.1 \tag{15}$$

Concurrently, the experimentally observed flow patterns are

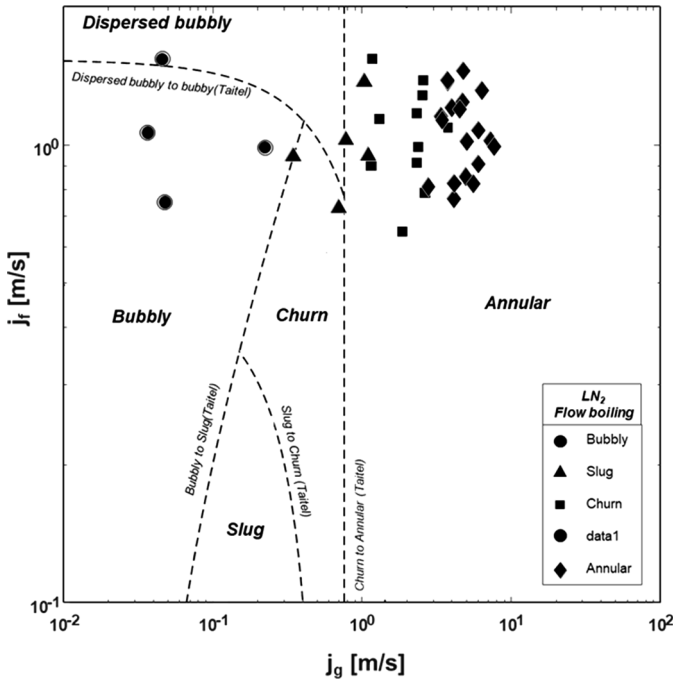

Fig. 16. Flow regime map based on superficial velocities, along with experimentally discerned flow patterns and transition lines predicted by Taitel et al. [49].

distinctly delineated and depicted in Fig. 16 using superficial velocities. Note that while evaluating the model against microgravity experimental data, the standard Earth gravity value for gravitational acceleration (g) was utilized, as applying microgravity acceleration (10^{-4} m/s^2) renders the model's predictions non-physical (negative values).

Multiple interesting observations arise from this assessment. First, the predictions with dispersed bubbly and bubbly transition model well coincides with the experimentally observed bubbly flow patterns where small size bubbles were uniformly distributed at large mass velocity, as confirmed by the captured flow images in Fig. 11. Second, the predicted bubbly to slug regime transition by Taitel et al. [49], aligns effectively with the experimental observations. Notice the distinct region where bubbly flow transitions directly into annular flow, bypassing slug or churn flow. This phenomenon is adeptly captured by the present experimental setup, as depicted in Fig. 11, where annular flow directly emerges as the population of bubbles increases. Third, the model suggested for churn to annular transition deviates from the experimental observation. However, it's intriguing to note that the observed experimental transition line also maintains a vertical alignment, coinciding with the model's trend. It is evident that the predictive capability can be improved by adjusting the empirical constant in Eq. (15), to a higher value. Further improvement should be pursued with additional flow visualizations data for multiple flow orientations.

4. Heat transfer results and discussion

4.1. Flow boiling curves

4.1.1. Microgravity boiling curves

The heat transfer results presented in this section draw fundamental distinctions between microgravity pool boiling and microgravity flow boiling. In microgravity pool boiling studies, bubbles, having longer residence time on the heated wall due to absence of buoyancy, have been reported to grow into a few enormously sized coalescent vapor masses compared to many smaller, more discrete bubbles in terrestrial gravity [28]. Absent such behavior for flow boiling illustrates a fundamental difference between microgravity pool boiling and microgravity flow boiling. In microgravity flow boiling, flow inertia exerts a shear lift force on nucleating bubbles [36] causing them to detach from the heated wall rather than incur appreciable near-wall growth. For cryogenic

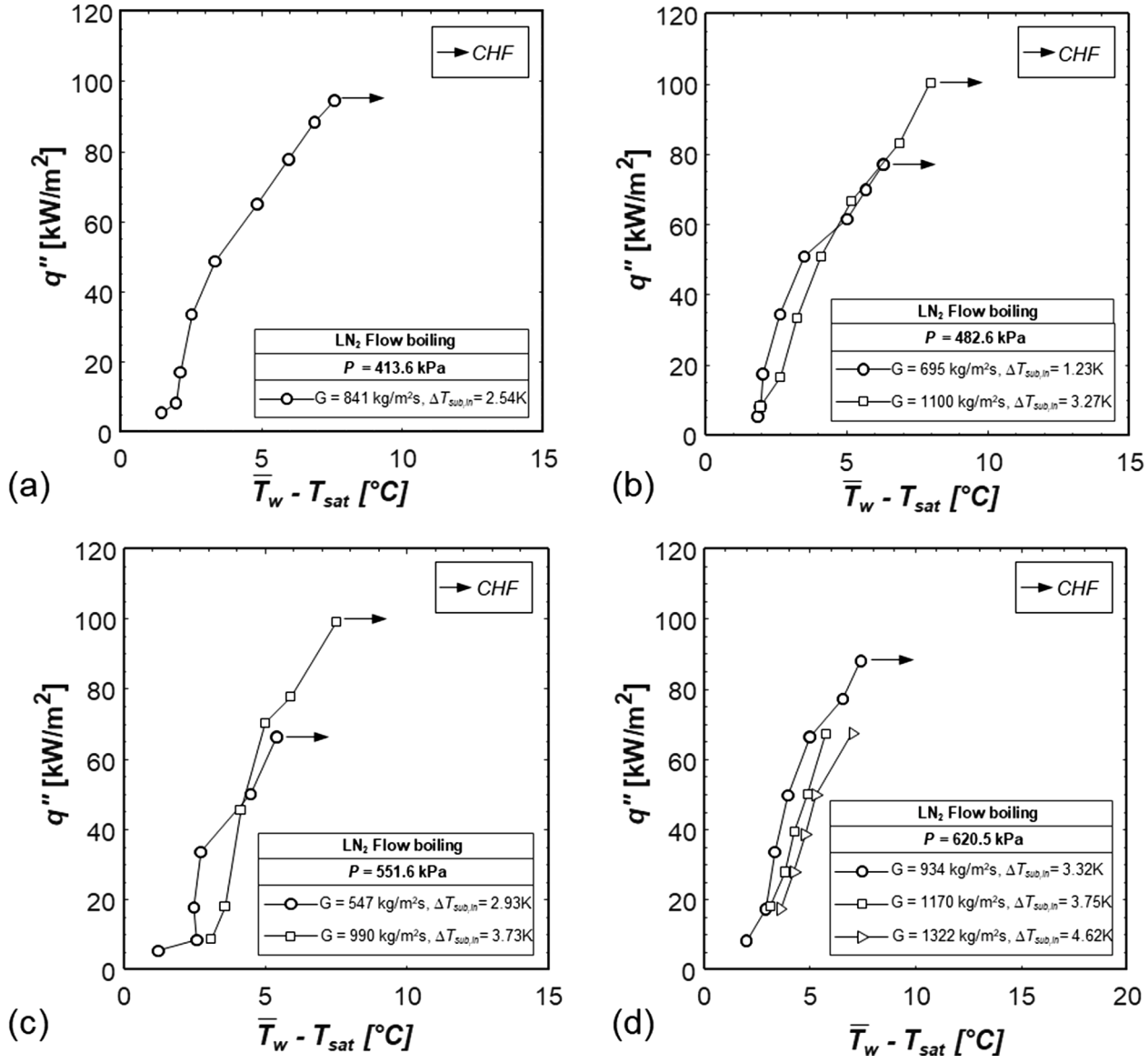

Fig. 17. Microgravity boiling curves for different operating conditions: (a) P_{in} = 413.6 kPa, G = 841 kg/m^{2}s, (b) P_{in} = 482.6 kPa, G = 695 and 1100 kg/m^{2}s, (c) P_{in} = 551.6 kPa, G = 547 and 990 kg/m^{2}s, and (d) P_{in} = 620.5 kPa, G = 934, 1170, and 1322 kg/m^{2}s.

fluids, owing to their low surface tension, the force needed to lift the bubbles from the wall is smaller than for room-temperature fluids. This points to the enormous advantages of cryogenic flow boiling over cryogenic pool boiling for in-space microgravity thermal management applications in terms of better ability to maintain nucleate boiling to much higher fluxes and resist early dryout.

A boiling curve provides graphical representation of relationship between wall heat flux and wall superheat, which is very useful for understanding heat transfer characteristics. Fig. 17 shows multiple sets of boiling curves acquired in the present microgravity flow boiling experiments for various operating conditions under four different system pressures. Fig. 17(a) displays a boiling curve based on average wall temperature for $G = 841$ kg/m^{2}s, and $\Delta T_{sub,in} = 2.54$ K, at $P_{in} = 413.6$ kPa. The initial short segment of the curve features small slope, outcome of dominance of ineffective single-phase liquid cooling, which corresponds to 5 % CHF as captured earlier in Fig. 10(b). A further increase in heat flux triggers ONB, which is followed immediately by a large increase in the slope, as single-phase heat transfer is overwhelmed by bubble formation and latent heat transfer. As heat flux is increased further, the boiling curve slope gradually deviates from "nearly-vertical" to more slanted, indication of heat degradation resulting from a transition from wall bubble nucleation to elongated bubble and annular regimes. However, there is clear distinction between heat transfer behavior of LN_2 (and cryogens in general) in the annular regime compared to that for room-temperature fluids such as water. As shown in the numerous flow visualization images presented earlier, nucleate boiling persists well into the annular regime, occurring within the annular film. This behavior is attributed to low surface tension and low latent heat of vaporization, causing cryogens to require small superheat to initiate bubble nucleation. But eventually, as the annular liquid film becomes very thin, intermittent dryout commences as partial breakup of the film exposes the heated wall to core vapor. Lacking sufficient liquid replenishment to the heated wall, the wall temperature then increases uncontrollably once CHF is reached, which is indicated by a horizontal arrow in the figure. Fig. 17(b) shows, for same pressure of $P_{in} = 482.6$ kPa, microgravity boiling curves for two different mass velocities: $G = 695$ kg/m^{2}s (with $\Delta T_{sub,in} = 1.23$ K) and $G = 1100$ kg/m^{2}s (with $\Delta T_{sub,in} = 3.27$ K). Clearly captured here are the important effects of increasing the mass velocity, first and foremost of which is a profound increase in CHF. This is an obvious outcome of higher mass flow both reducing vapor void and granting more liquid access to the wall. Fig. 17(b) shows slight offset between the curves in the lower heat flux range, followed a crossover with the higher flow rate sustaining boiling at much higher heat fluxes. Fig. 17(c) shows, for same pressure of $P_{in} = 551.6$ kPa, microgravity boiling curves for $G = 547$ kg/m^{2}s (with $\Delta T_{sub,in} = 2.93$ K) and $G = 990$ kg/m^{2}s (with $\Delta T_{sub,in} = 3.73$ K). Here, mass velocity trends are similar to those from Fig. 17(b). Lastly, Fig. 17(d) shows, for $P_{in} = 620.5$ kPa, boiling curves for three mass velocities of $G = 934$ kg/m^{2}s (with $\Delta T_{sub,in} = 3.32$ K), $G = 1170$ kg/m^{2}s (with $\Delta T_{sub,in} = 3.75$ K), and $G = 1322$ kg/m^{2}s (with $\Delta T_{sub,in} = 4.62$ K). Note that the boiling curves corresponding to the two higher mass velocities did not reach completion up to CHF because of the limited number of parabolas that were available during flight experiments for these operating conditions.

4.1.2. Critical heat flux under microgravity

Fig. 18 shows measured q''_{CHF} versus mass velocity acquired from the microgravity flow boiling experiments along with predicted q''_{CHF}, calculated using correlations recently developed by Ganesan et al. [50] for CHF resulting from both Dryout and Departure from Nucleate Boiling (DNB) in terrestrial gravity. For flow boiling in tubes, two primary types of CHF are commonly encountered. Dryout CHF occurs when the thickness of the annular liquid layer eventually vanishes, leading to complete wall exposure to the vapor core. For DNB, which typically occurs when the coolant is supplied to the tube in highly subcooled state and high mass velocity and is subjected to high wall heat flux, nucleating bubbles near the heated wall coalesce locally, forming an oblong vapor

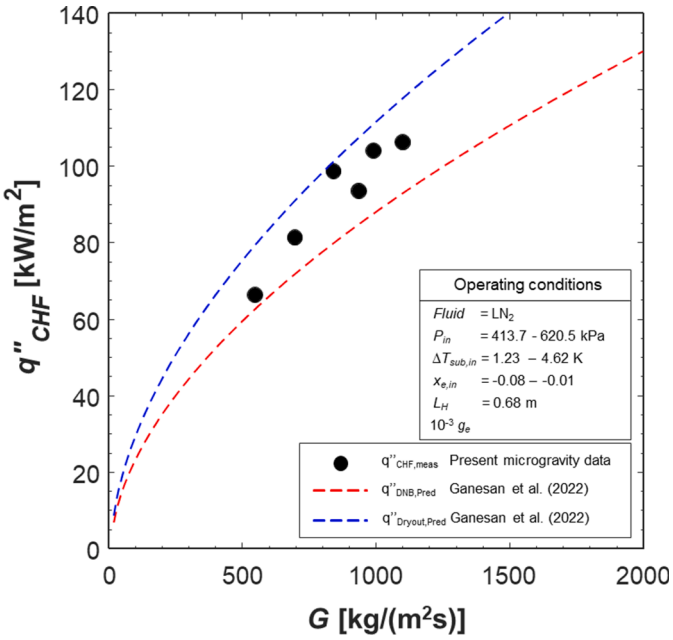

Fig. 18. Variation of measured microgravity CHF with mass velocity compared to predictions of terrestrial-based CHF correlations corresponding to Dryout and DNB.

blanket, efficiently blocking liquid replenishment and causing a significant escalation in wall temperature. Note that, while a single DNB correlation was proposed, different Dryout correlations were recommended for vertical versus horizontal flows in terrestrial gravity. The measured q''_{CHF} in Fig. 18 is calculated as average of the heat flux that instigated the unsteady wall temperature excursion and the previous stable boiling heat flux, since actual q''_{CHF} value falls in between. Also, note that the Dryout correlation used in Fig. 18 is for vertical flow in Earth gravity since, as witnessed from the flow visualization results in earlier sections, microgravity flow structure at or near CHF more closely resembles that of terrestrial vertical upflow than horizontal flow. For the comparison, predicted q''_{CHF} is evaluated at $P_{in} = 517.1$ kPa and $\Delta T_{sub,in} = 2.93$ K, which are arithmetic averages of operating conditions for measured q''_{CHF}. Measured microgravity CHF is shown increasing with increasing mass velocity, but not in a linear fashion. Rather, there is some attenuation in the measured CHF with increasing mass velocity. As described earlier, annular flow commences for lower mass velocities at much lower heat fluxes than for high mass velocities. For lower mass velocities, there is propensity for the thin annular liquid film to undergo local or partial dryout because of diminished liquid content. In contrast, for high mass velocities, transition to annular flow is delayed to much higher heat fluxes, meaning the heat flux required to greatly thin the annular film and eventually instigate partial dryout is also increased, which results in higher CHF. When compared to the predicted trendlines of DNB and Dryout, the measured microgravity CHF is larger than predicted by the terrestrial DNB correlation but lower than by the one for terrestrial Dryout. Qualitatively, Fig. 18 shows microgravity CHF can be predicted with reasonable accuracy using Ganesan et al.'s terrestrial-based CHF correlations.

4.1.3. Effects of gravity on boiling curve

To better understand effects of gravity on the boiling curve, boiling curves acquired both in terrestrial gravity and microgravity are compared for three different sets of operating conditions. Note that all the terrestrial data discussed here were acquired by the present authors [42] in the horizontal flow orientation using the same experimental facility used in the present parabolic flight experiments. In the terrestrial horizontal flow experiments pronounced stratification led to drastic

differences between flow patterns at the top versus bottom of the tube's cross-section, with relatively large vapor structures amassing near the top and more nucleate boiling persisting near the bottom. This is why all the terrestrial data utilized here are for the bottom wall.

Fig. 19(a) shows boiling curves for microgravity and terrestrial gravity for $G = 696$ kg/m^{2}s and $P_{in} = 482.6$ kPa. At low heat fluxes, the curves show no significant difference in wall superheat, which indicates limited gravitational effects in a region where heat transfer is dominated by combination of single-phase liquid and mild nucleate boiling. However, with a slight increase in heat flux, the boiling curves take on distinct trajectories, with the microgravity curve exhibiting a notably steeper slope than in terrestrial gravity. This discrepancy in slope translates to significantly higher wall superheat values in the 1-g_e horizontal flow. The elevated wall temperatures in the horizontal flow under terrestrial gravity can be elucidated through various contributing factors. First, in the low heat flux range, the earlier initiation of bubble nucleation and faster bubble growth in microgravity compared to terrestrial gravity fosters a more efficient cooling via latent heat, thereby sustaining lower wall temperatures in microgravity. Second, the higher wall temperatures of 1-g_e horizontal flow in the intermediate heat flux range primarily arise from the asymmetrical flow patterns with vapor stratification observed in the horizontal flow. Due to the vapor concentration towards the top surface, an uneven circumferential wall temperature profile emerges, with the upper surface temperatures surpassing those of the bottom surface. Consequently, and imperatively, circumferential heat conduction occurs, aiming to equalize the temperature distribution, ultimately elevating the temperature at the bottom surface. In contrast, under the same heat flux conditions, microgravity leads to symmetrical flow patterns due to the absence of buoyancy force, as can be confirmed in Fig. 9. With both walls in contact with liquid to cool down the walls effectively, resulting wall superheat shall be lower than those of 1-g_e horizontal flow. At high heat flux region, as annular flow pattern develops in both gravity levels, the differences in slope gradually subside ultimately resulting in equal wall temperatures at about $q'' = 60$ kW/m^2. Whilst, in terrestrial gravity, CHF occurs at $q'' = 60$ kW/m^2 because of conditions not on the bottom but near the top where CHF is triggered earlier by massive vapor stratification. This is proof of negative impact of body force for horizontal flow boiling in terrestrial gravity. In contrast, in microgravity, absent any stratification, symmetrical interfacial structure allows boiling conditions to persist to significantly higher CHF value.

Fig. 19(b) boiling curve comparison for a higher mass velocity of $G = 840$ kg/m^{2}s with $P_{in} = 413.7$ kPa. Like Fig. 19(a), the two curves overlap in the lowest heat flux range indicating no significant effect of gravity on single-phase or bubbly flow regime, which can be confirmed by the equal values of wall superheat for both gravities. For microgravity, a sudden increase in slope appears following the second heat flux signifying the appearance of differences in flow structure produced in each gravity level. However, as observed from Fig. 19(a), with further increases in heat flux, the boiling curves for microgravity and terrestrial gravity overlap resulting in similar wall superheat for identical heat flux conditions. Interfacial structure in the overlapping range for the two gravities is predominantly annular. Additionally, as discussed in [42] and earlier in the present study, high flow inertia at $G = 840$ kg/m^{2}s dwarfs buoyancy force effects in terrestrial horizontal flow, which both diminishes differences in both boiling heat transfer and CHF between the two gravitational environments. Nevertheless, CHF in microgravity is still greater because of superior symmetry, compared to slight asymmetry and more top vapor accumulation in terrestrial horizontal flow.

Lastly, Fig. 19(c) compared boiling curves for a yet higher mass velocity of $G = 1100$ kg/m^{2}s with $P_{in} = 482.6$ kPa. Because of much enhanced inertia and therefore better flow symmetry, the two curves overlap one another over broad range of heat fluxes and culminate in close CHF values. The trends from Fig. 19 prove understanding microgravity flow boiling performance for large mass velocities can benefit greatly from terrestrial findings.

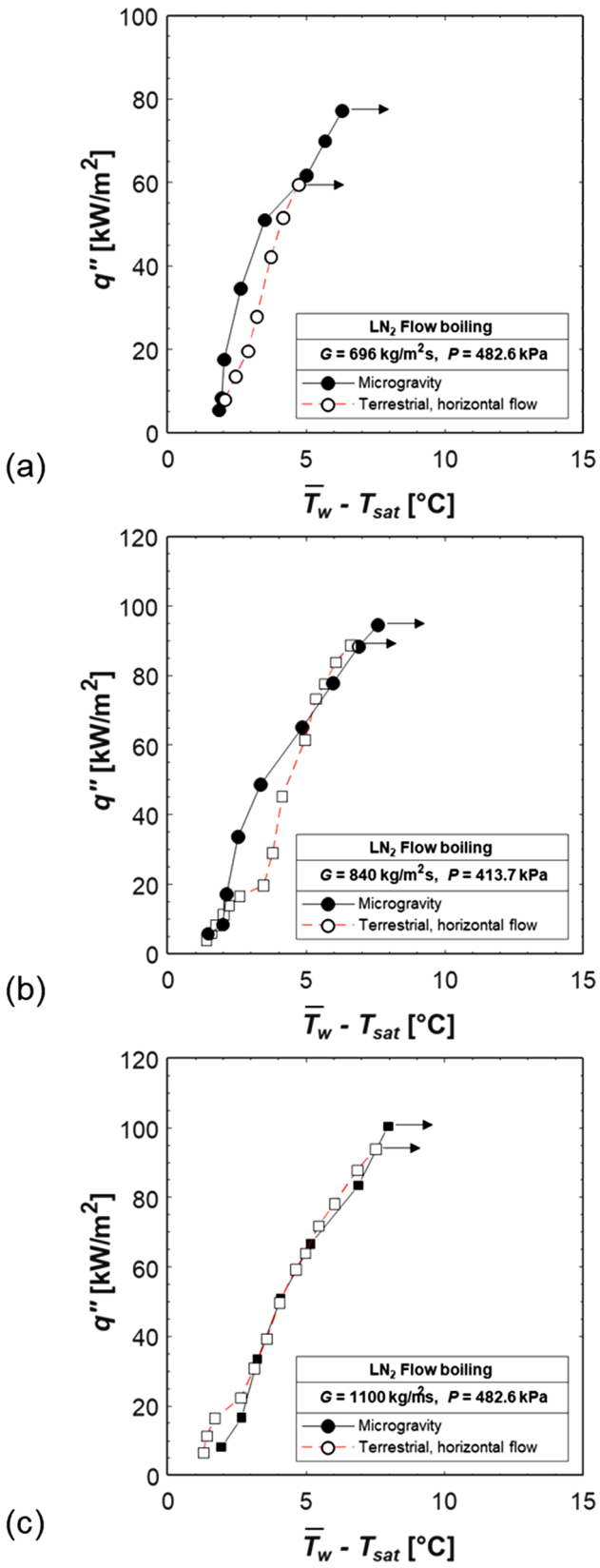

Fig. 19. Comparison of boiling curves for microgravity and horizontal flow in terrestrial gravity for G = (a) 695, (b) 840, and (c) 1100 kg/m^{2}s.

4.2. Wall temperature

Fig. 20 shows axial variations of heated tube outer wall temperature, $T_{w,z}$, recorded from the parabolic flight experiments for different heat fluxes and six sets of operating conditions. For all conditions tested, $T_{w,z}$ is shown increasing monotonically with increasing heat flux, with highest values measured in the inlet region, presumably because of higher contribution of less efficient single-phase liquid heat transfer. Excepting the inlet region, axial profiles are rather flat for the lowest heat flux, implying prevalence of identical interfacial behavior along entire length of the heated tube.

In Fig. 20(a), wall temperature profiles for $G = 695$ kg/m^{2}s and $P_{in} = 482.6$ kPa are shown overlapping one another for the two lowest heat fluxes despite a doubling of heat flux. Examination of video images from Fig. 9(c) reveals both conditions correspond to fairly similar interfacial structure comprising large oblong bubbles. In the higher heat flux range, flow regime develops into annular, wherein a thin annular liquid film surrounds a thick central vapor core. However, as discussed earlier, residual bubble nucleation persists even within the annular film, outcome of LN_2's low surface tension and low latent heat of vaporization. This, along with gradual thinning of the annular film by evaporation, may explain the small downstream decrease in $T_{w,z}$. Notice how this downstream trend is reversed at 94.9 % CHF with loss of bubble nucleation coupled with onset of partial film dryout before CHF is ultimately reached.

Fig. 20(b) shows axial variations of $T_{w,z}$ for same inlet pressure as Fig. 20(a) but a much higher mass velocity of $G = 1100$ kg/m^{2}s. Overall, trends relative to increasing heat flux are similar to those from Fig. 20 (a). However, temperatures in the lower heat flux range are lower for $G = 1100$ kg/m^{2}s compared to $G = 695$ kg/m^{2}s; this is where the higher mass velocity reduces vapor generation, resulting in more abundant nucleate boiling aided by faster moving fluid.

Fig. 20(c) and (d) show similar $T_{w,z}$ trends with increasing heat flux for $G = 547$ and 990 kg/m^{2}s, respectively, but equal pressure of $P_{in} = 551.6$ kPa. Fig. 20(e) and (f) show similar $T_{w,z}$ trends with increasing heat flux for $G = 841$ and 934 kg/m^{2}s, respectively, but equal pressure of $P_{in} = 620.5$ kPa. Notably, some of the cases do not capture the wall temperature rise near the outlet for near-CHF heat fluxes, but, instead, shows a rather flat axial profile, indicating stable annular liquid film flow persisting without measurable dryout until eventual attainment of CHF.

4.3. Heat transfer coefficient

4.3.1. Local heat transfer coefficient

Fig. 21 shows variations of heat transfer coefficient, $h_{tp,z}$, with respect to equilibrium vapor quality for different heat fluxes and six sets of operating conditions. The layout of the overall figure along with the operating conditions and heating configurations of each plot are consistent with Figs. 20. Note that local equilibrium vapor qualities were calculated using Eq. (3), and local fluid temperatures were retrieved using Eq. (4). Common trends can be observed throughout the cases with various operating conditions: (i) general improvement in heat transfer with increasing heat flux, (ii) compromised heat transfer effectiveness in the inlet region because of stronger contribution of less effective single-phase liquid heat transfer, (iii) general enhancement at high vapor quality region due to thin annular film evaporation coupled with residual bubble nucleation within the film, and (iv) eventual downstream decline in heat transfer performance at the highest heat flux tested (for three of the cases) because of partial dryout of the film before eventual attainment of CHF.

Notice the consistent pattern of a transition in slope occurring within the vapor quality range of 0 - 0.05 under intermediate to high heat flux conditions. Under intermediate heat fluxes, approximately 50 % CHF, the heat transfer coefficient curves show an ascending slope at lower vapor qualities, followed by a nearly constant slope at intermediate vapor qualities, and ultimately, a further increase at higher vapor qualities. The plateau in the curve's slope signifies the transition from bubbly or slug flow to annular flow, with the subsequent increase at higher vapor qualities attributed to intensified convective boiling effects. Interestingly, the vapor quality at which this regime transition occurs remains relatively consistent across increasing heat fluxes, typically between 0 - 0.05. Furthermore, and of utmost significance, the sustained high heat transfer coefficients at elevated heat fluxes and high vapor quality regions underscore the distinct characteristics of cryogens, characterized by the persisting nucleate boiling without complete suppression.

4.3.2. Average heat transfer coefficient

Fig. 22 shows variations of average heat transfer coefficient, $h_{tp,ave}$, with heat flux measured during the microgravity experiments for different sets of operating conditions with overall layout of individual plots consistent with that from Fig. 17. For all operating conditions, $h_{tp,ave}$ increases with increasing heat flux first sharply in the lower heat flux range, then more moderately in the middle heat flux range, before eventually degrading in the higher range as CHF is approached. Arrows indicate the drastic decline in performance associated with CHF.

Fig. 22(a) shows $h_{tp,ave}$ variation for $P_{in} = 413.6$ kPa, $G = 841$ kg/m^{2}s, and $\Delta T_{sub,in} = 2.18$ K. The two lowest heat flux points are clustered together; this is also where $h_{tp,ave}$ is lowest. Cross examination with Fig. 10(b) shows these are conditions of minuscule nucleation as well as dominance of inefficient single-phase liquid heat transfer. With increasing heat flux, $h_{tp,ave}$ begins to increase drastically as the flow transitions to one comprised of oblong bubbles with aggressive mixing and turbulence assisting replenishment of the heated wall with liquid. The increase ceases at $q'' = 48.69$ kW/m^2, where the flow pattern transitions to annular, as confirmed from Fig. 10(b). In annular flow, nucleate boiling is gradually suppressed, decreasing $h_{tp,ave}$ as the dominant heat transfer mechanism shifts from nucleate boiling to convective boiling. However, as indicated earlier, the bubble nucleation is not completely suppressed in annular flow but persists within the annular film for a broad range of heat fluxes until it ceases very close to CHF. A more useful discussion on suppression of nucleation in cryogenic flow boiling can be found in [42].

Fig. 22(b) shows $h_{tp,ave}$ variations for two sets of operating conditions: $G = 695$ kg/m^{2}s with $\Delta T_{sub,in} = 1.23$ K and $G = 1100$ kg/m^{2}s with $\Delta T_{sub,in} = 3.27$ K for identical pressures of $P_{in} = 482.6$ kPa. Here, effect of increased mass velocity in microgravity is depicted. For the lower mass velocity of 695 kg/m^{2}s and heat fluxes up to 50 kW/m^2, with the rapid increase of vapor bubble size resulting from longer residence time on the heated wall and appreciable mixing, heat transfer is strongly ameliorated. In contrast, for the higher mass velocity of 1100 kg/m^{2}s, with the overwhelmingly intensified flow inertia sweeping nucleated bubbles away from the heated wall, bubble nucleation is suppressed, resulting in lower heat transfer coefficient than for the lower mass velocity under the same heat flux. However, as nucleate boiling is interrupted around 50 kW/m^2 for the lower mass velocity, the corresponding heat transfer coefficient curve incurs a sharp decline to below that for the high mass velocity, eventually also culminating in lower CHF. Similar trends regarding effects of mass velocity on $h_{tp,ave}$ are captured in Fig. 22(c) and (d) for $P_{in} = 551.6$ and 620.5 kPa, respectively.

4.3.3. Effects of gravity on average heat transfer coefficient

To better understand effects of gravity on flow boiling heat transfer, variations of average heat transfer coefficient with wall heat flux based on present microgravity data are compared in Fig. 23 to those for horizontal flow in terrestrial gravity for three sets of operating conditions. Note that all the terrestrial data were acquired previously by the present authors [42] with the same payload used in the present parabolic flight experiments. The overall layout of Fig. 23 and the operating conditions of each sub-plot mirror those of Fig. 19.

Fig. 23(a) shows the comparison between microgravity and

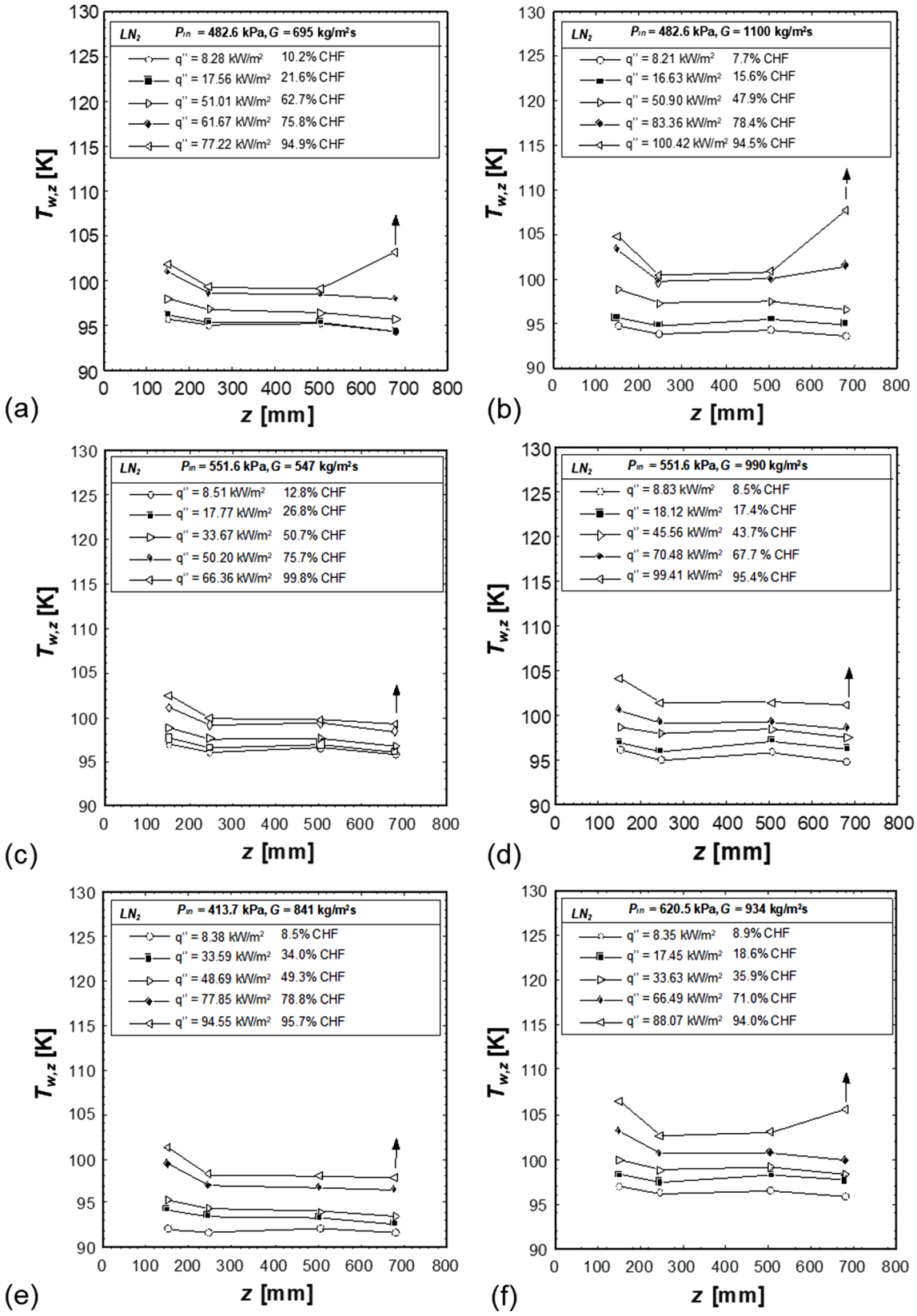

Fig. 20. Streamwise variations of wall temperature for different heat fluxes and (a) $P_{in} = 482.6$ kPa, $G = 695$ kg/m^{2}s, (b) $P_{in} = 482.6$ kPa, $G = 1100$ kg/m^{2}s, (c) $P_{in} = 551.6$ kPa, $G = 547$ kg/m^{2}s, (d) $P_{in} = 551.6$ kPa, $G = 990$ kg/m^{2}s, (e) $P_{in} = 413.7$ kPa, $G = 841$ kg/m^{2}s, and (f) $P_{in} = 620.5$ kPa, $G = 934$ kg/m^{2}s.

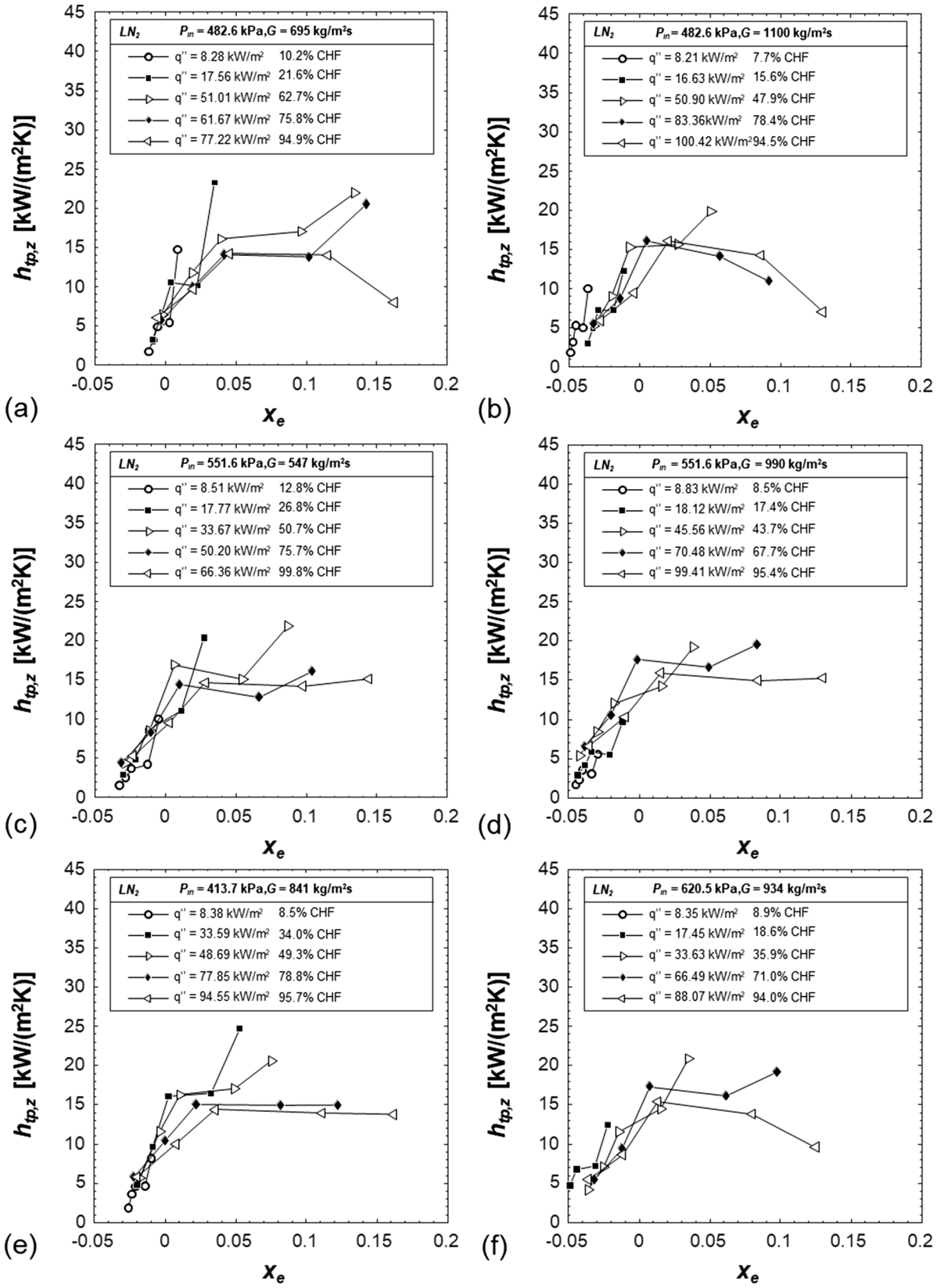

Fig. 21. Variations of local heat transfer coefficient with respect to thermodynamic equilibrium quality for different heat fluxes and (a) P_{in} = 482.6 kPa, G = 695 kg/m^{2}s, (b) P_{in} = 482.6 kPa, G = 1100 kg/m^{2}s, (c) P_{in} = 551.6 kPa, G = 547 kg/m^{2}s, (d) P_{in} = 551.6 kPa, G = 990 kg/m^{2}s, (e) P_{in} = 413.7 kPa, G = 841 kg/m^{2}s, and (f) P_{in} = 620.5 kPa, G = 934 kg/m^{2}s.

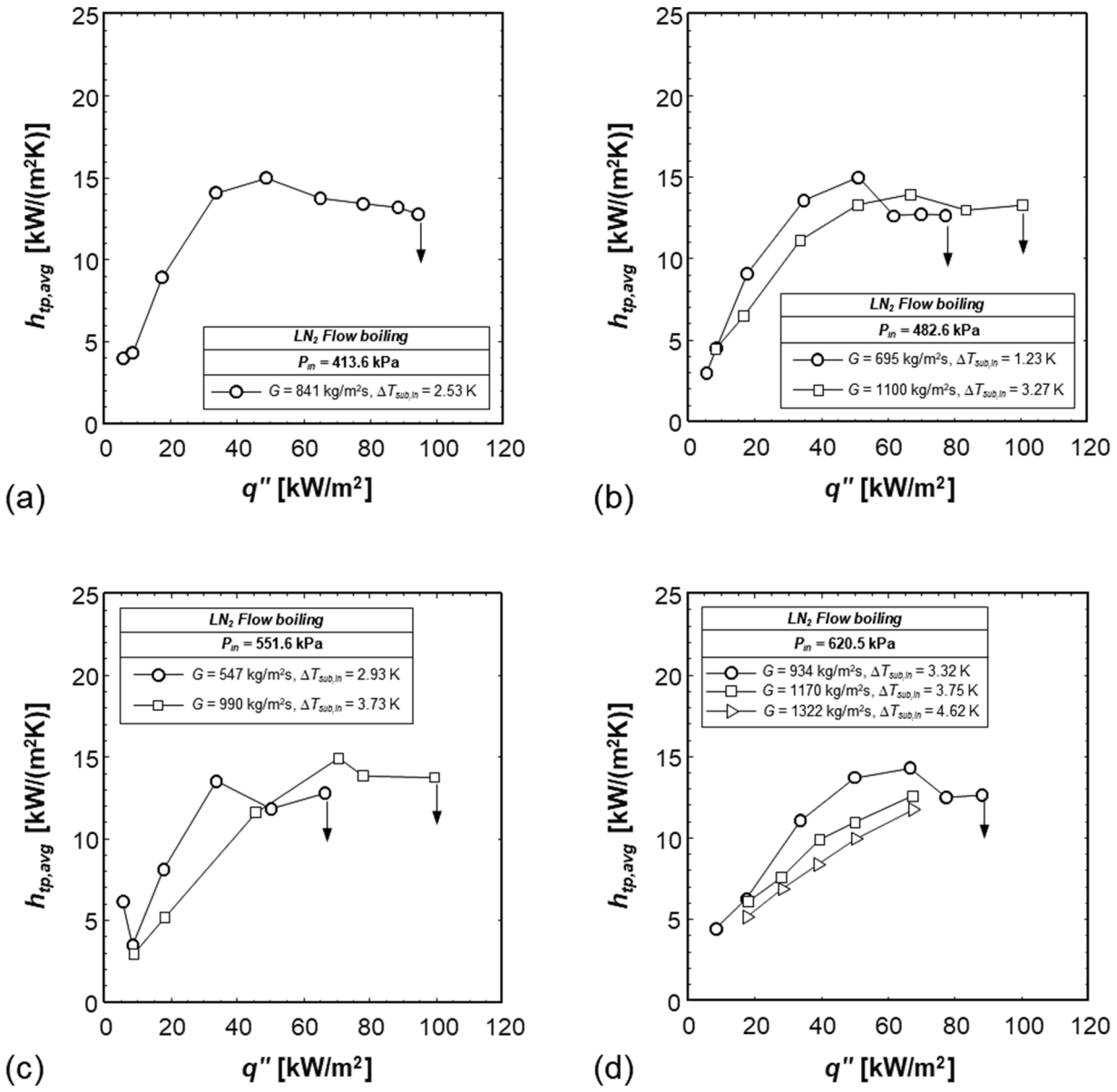

Fig. 22. Variation of average heat transfer coefficient with heat flux for (a) P_{in} = 413.6 kPa, G = 841 kg/m^{2}s, (b) P_{in} = 482.6 kPa, G = 695 kg/m^{2}s and G = 1100 kg/m^{2}s, (c) P_{in} = 551.6 kPa, G = 547 and 990 kg/m^{2}s, (d) P_{in} = 620.5 kPa, G = 934, 1170, and 1322 kg/m^{2}s.

terrestrial gravity data for G = 696 kg/m^{2}s and P_{in} = 482.6 kPa, representing low mass velocity cases. The plot is segmented into four sections that are marked with numbered rectangular boxes to clarify trends for different heat flux ranges. In Section 1, a low heat flux region, no significant gravity effects are observed, indicating bubble nucleation and cavity activation are local phenomena governed by local near-wall fluid temperature. In Section 2, a low to intermediate heat flux region, differences between the two gravities intensify, with heat transfer coefficient in microgravity being better than in terrestrial gravity. Notice here the drastic differences between the top and bottom of the horizontal tube in terrestrial gravity, with the former yielding relatively poor heat transfer performance because of buoyancy-induced stratification of vapor atop. Overall, differences in heat transfer performance between the two gravities are rooted in difference in flow regimes for same heat flux. As discussed earlier and confirmed from the flow visualizations, absent buoyancy effects, earlier bubble nucleation and faster bubble growth rate are characteristic traits of nucleate boiling in microgravity flow boiling. This interfacial behavior propagates along the tube further influencing flow pattern transition in microgravity. With earlier bubble generation and faster growth rate, detached bubbles coalesce into large oblong vapor structures in microgravity, with nucleation persisting along the wall, while, for same heat flux in terrestrial gravity, the flow pattern remains bubbly and comprised of small, well-dispersed bubbles. Ensuing fluid acceleration resulting from increased vapor generation, coupled with appreciable mixing and turbulence, appears to contribute appreciable enhancement in microgravity. Delayed flow pattern development in terrestrial gravity has also been reported in previous microgravity experiments with conventional room temperature fluids. For example, Ohta and Baba [28] reported markedly larger bubble size in microgravity than in both terrestrial gravity and hypergravity, especially for low mass velocities. In addition, they reported that void fraction increases dramatically near the inlet, which in turn promotes greater vapor generation and faster transition to annular flow whereas, in terrestrial gravity, flow pattern transitions are slower with a more gradual increase of void fraction along the heated tube. Narcy et al. [51] also reported larger and undeformed spherical bubbles in microgravity compared to smaller and deformed bubbles in terrestrial gravity, which enhanced heat transfer in microgravity mirroring the enhancement

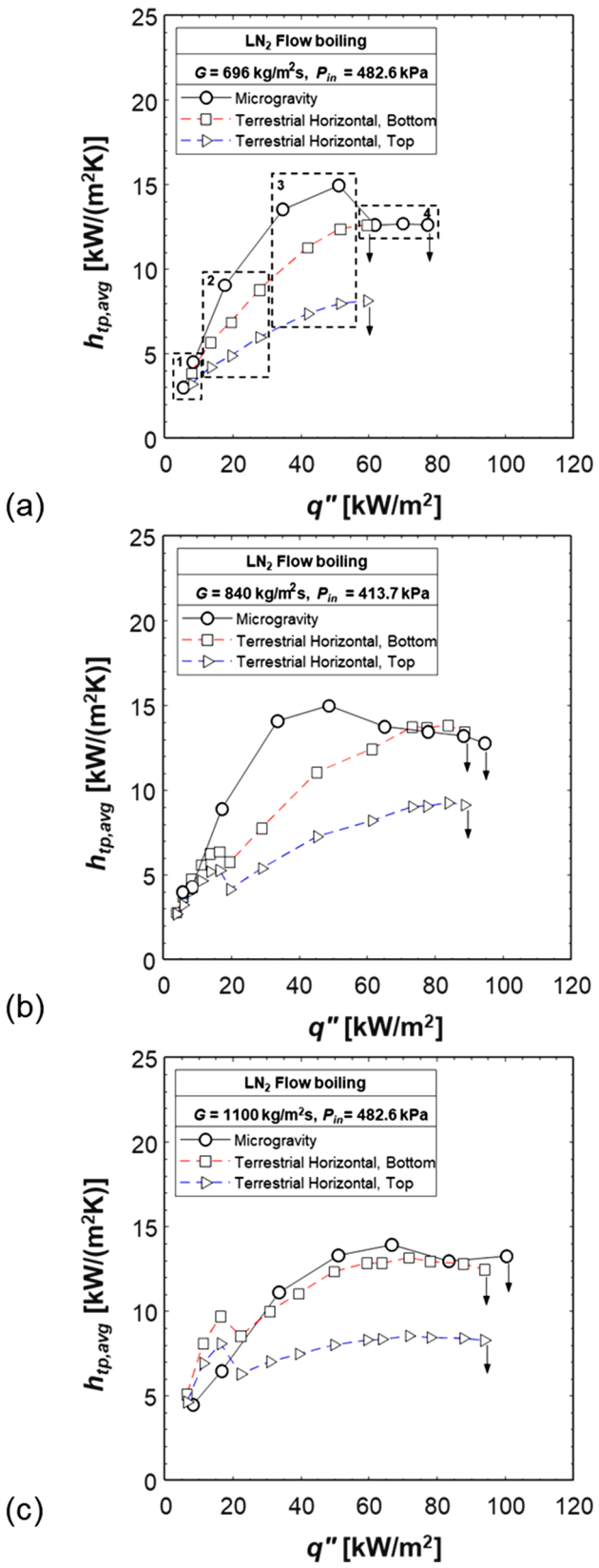

Fig. 23. Effects of gravity on average heat transfer coefficient for near-saturated inlet and mass velocities of G = (a) 695, (b) 840, and (c) 1100 kg/m^{2}s.

captured in Section 2 of Fig. 23(a). A similar increase in heat transfer performance in microgravity at low heat flux conditions was also observed in experiments by Baltis et al. [52] who reported distinct difference in flow pattern: bubbly in terrestrial gravity and intermittent (i.e., transitioning to annular) in microgravity, with the latter yielding better heat transfer because of faster flow and intensified turbulence. In Section 3 in Fig. 23(a), an intermediate heat flux region, the microgravity heat transfer coefficient exceeds that of terrestrial gravity. Here, there are important differences in flow pattern between the two gravities: large oblong bubbles and/or annular flow for microgravity versus stratified plug flow for terrestrial gravity. For microgravity, the vapor coalesces into a high void, high velocity central core pressing a thin annular liquid film against the heated wall. With such interfacial structure, heat transfer performance in microgravity is enhanced by a combination of (i) small thermal resistance across the thin film, (ii) residual bubble nucleation occurring within the liquid film, (iii) increased velocity of both vapor core and annular film (because of high void fraction), and (iv) enhanced mixing and turbulence. In contrast, for terrestrial gravity, with plug flow, heat transfer along the bottom is compromised by formation of a comparatively slow liquid layer with limited mixing, while heat transfer along the top is greatly reduced due to formation of large oblong vapor structures that shield the wall from effective liquid replenishment. In Section 4 in Fig. 23(a), a high heat flux region, the microgravity heat transfer coefficient is seen overlapping with the last steady state point for terrestrial gravity's bottom region. As discussed earlier, the decrease in microgravity heat transfer coefficient with increasing heat flux in the high heat flux region is attributed to suppression of nucleate boiling, including within the annular film. Meanwhile, the flow pattern in terrestrial gravity has also transitioned into annular flow, characterized by a thick vapor core and an annular liquid film around the tube's inner wall, bearing some similarity to the microgravity situation, albeit for only the bottom wall region. This attenuated gravity effect at high qualities was observed and reported in prior flow studies involving room temperature fluids. For example, Lebon et al. [53], who conducted microgravity HFE-7000 flow boiling experiments in parabolic flight, reported independence of heat transfer coefficient from gravity level for their highest heat flux cases where flow pattern transitioned to annular. Baltis et al. [52] also did not observe differences in heat transfer coefficient between microgravity and terrestrial gravity for high quality annular flow. Interestingly, Section 4 in Fig. 23(a) also captures appreciable discrepancy in CHF between the two gravities, with microgravity yielding much higher value. Early CHF attainment for terrestrial gravity is the direct outcome of vapor amassing in the top region of the horizontal tube rather than interfacial conditions in the bottom region.

In Fig. 23(b), average heat transfer coefficient variations with heat flux for microgravity and terrestrial gravity are compared for G = 840 kg/m^{2}s and P_{in} = 413.7 kPa. Overall, trends in the low, low to intermediate middle, and intermediate heat flux regions mirror those for G = 696 kg/m^{2}s, Fig. 23(a), because of similarities in both flow structure and transitional characteristics. And weakened gravity effects in the high heat flux region are reflected by nearly equal performance between microgravity and the bottom region for terrestrial gravity. The attenuated difference of HTC between gravity levels is an outcome of flow acceleration in the high quality annular region. However, a noticeable difference between Fig. 23(a) and 23(b) is closer CHF values for the latter. With higher mass velocity of G = 840 kg/m^{2}s, intensified flow inertia became the dominant force over body force and increased maximum allowable heat flux, CHF, for 1-g_e horizontal flow.

In Fig. 23(c), for G = 1100 kg/m^{2}s and P_{in} = 482.6 kPa, there is continuation of trends captured in Fig. 23(b) for the lower mass velocity of G = 840 kg/m^{2}s, but with the stronger flow inertia for the higher mass velocity yielding further attenuation of gravity effects, leading to near identical heat transfer performance as well as closer CHF values between microgravity and bottom region for terrestrial horizontal flow.

4.3.4. Effects of gravity on local heat transfer coefficient

To delve deeper into the effects of gravity on flow boiling heat transfer, variations of local heat transfer coefficient with wall heat flux based on present microgravity data are compared in Fig. 24 to those for horizontal flow in terrestrial gravity for three sets of operating conditions at two different axial locations of $z = 245$ and 505 mm.

Fig. 24(a) shows the comparison between microgravity and terrestrial gravity data for $G = 696$ kg/m^{2}s and $P_{in} = 482.6$ kPa, representing low mass velocity cases, at two different axial locations. The plots are segmented into four sections, and the sections are numbered to clarify trends for different heat flux regions. At the axial location of $z = 245$ mm, the microgravity heat transfer coefficient curve constantly lies above those under terrestrial gravity, indicating enhanced heat transfer performance in microgravity. The primary basis of the enhancement stems from discrepancies in flow regime, arising from (i) faster bubble growth and prolonged bubble-to-wall contact in microgravity, (ii) the presence of non-stratified and symmetrical vapor structure in microgravity, and (iii) the occurrence of flow stratification resulting in asymmetrical vapor structure in terrestrial gravity. In Section 1, a low heat flux region, no significant effect of gravity is observed, accentuating the constrained impact of gravity on localized bubble dynamics such as bubble nucleation and cavity activation. On the contrary, the influence of gravity becomes more pronounced as the heat flux increases, particularly within Sections 2 and 3. In Section 2, the absence of buoyancy effects in microgravity leads to an enhanced heat transfer efficiency. This enhancement is achieved by facilitating prolonged contact between bubbles and the heated wall in microgravity, thereby extending the duration of latent heat transfer. In contrast, terrestrial environments experience faster bubble detachment due to the continuous presence of buoyancy force, which curtails the time available for bubbles to dissipate heat load through latent heat processes. The explanation provided is endorsed by the larger bubble size observed in microgravity when compared to hypergravity under same operating condition, as visually captured in Fig. 14. Moreover, in Section 3 under the higher heat flux condition, substantial disparities in vapor structures lead to a more pronounced discrepancy in heat transfer coefficients between the two gravity levels. Under microgravity, due to the absence of buoyancy, accumulated and coalesced vapor aligns at the core without stratification. Conversely, terrestrial gravity prompts heavier liquid to descend toward to the bottom surface due to the buoyancy force, resulting in lighter vapor structures floating atop the liquid and forming stratified flow patterns. Consequently, lower wall temperatures are achieved in microgravity where the heated tube is in continuous contact with liquid, translating to higher heat transfer coefficients. In Section 4, at the highest heat flux segment, the microgravity heat transfer coefficient diminishes as nucleate boiling becomes suppressed, aligning more closely with the heat transfer coefficient measured under terrestrial gravity conditions. Similar trends and the effects induced by gravity are also evident at the downstream axial location of $z = 505$ mm.

Fig. 24(b) and 24(c) show comparisons between microgravity and terrestrial gravity data for $G = 840$ kg/m^{2}s and $P_{in} = 413.7$ kPa, and $G = 1100$ kg/m^{2}s and $P_{in} = 482.6$ kPa, representing intermediate and high mass velocity cases, respectively. Similar to Fig. 24(a), local heat transfer coefficients are compared at two different axial locations of $z = 245$ and 505 mm. As mass velocity increases, intensified flow inertia serves to mitigate the influence of gravity. As a result, the disparities in heat transfer performance between the two gravity levels diminish progressively with higher mass velocity, as shown in Fig. 24(b) and 24(c). Notably, at high heat flux regions, the microgravity heat transfer coefficients gradually decrease and nearly align with those measured in terrestrial gravity. This convergence can be attributed to the flow acceleration, which effectively supersedes the influence of gravity, especially under annular flow regime.

4.4. Evaluation of seminal correlations

4.4.1. Flow boiling correlations

The performances of seminal flow boiling HTC correlations are tested and compared to the present microgravity local heat transfer coefficient data as well as the authors' prior data [42] for terrestrial gravity horizontal flow boiling acquired using the same experimental facility. Predictive capability is evaluated via mean absolute error (MAE) which is defined as

$$MAE = \frac{1}{N}\sum \frac{\left|h_{tp,pred} - h_{tp,meas}\right|}{h_{tp,meas}} \times 100\ [\%] \tag{16}$$

Table 3 shows results for seven prior correlations. Note that, being derived from terrestrial gravity data, none of these correlations are intended for microgravity. They are presented as h_{tp} as a function of several parameters, key among them are pool boiling HTC, h_{pb}, accounting for contribution of nucleate boiling, convective boiling HTC, h_{cb}, accounting for heat transfer across annular film, "suppression factor", S, measure of attenuation of nucleate boiling with increasing quality, and "two-phase multiplier", F, measure of enhanced convection in annular flow with increasing quality. Fig. 25 shows parity plots for the different correlations evaluated.

One of the earliest in the heat transfer literature, the Chen correlation [54] employs a formulation for h_{nb} derived earlier by Forster and Zuber [61] from pool boiling data along with an h_{cb} correlation for single-phase liquid convection. The contributions of h_{nb} and h_{cb} are weighted via the multipliers S and F. Fig. 25(a) shows this correlation provides very good predictions of both the microgravity and terrestrial gravity data, with MAEs of 17.81 and 19.90 %, respectively. Results for the Shah correlation [55], Fig. 25(b), are also quite good albeit with better accuracy relative to the microgravity data. Lesser accuracy is realized for both microgravity and terrestrial gravity by Gungor and Winterton's correlation [56] as shown in Fig. 25(c). Fig. 25(d) shows the correlation by Klimenko [57] yields very high deviation against microgravity data (MAE = 110.50 %) despite good predictions of terrestrial data (MAE = 19.57 %). Figs. 25(e) and (f) show correlations by Steiner and Taborek [59] and Kim and Mudawar [60] provide acceptable results for both gravities. A notable weakness of Steiner and Taborek's is, by using different empirical constants for different cryogenic fluids, unlike the other correlations evaluated, it is not a universal correlation.

Table 3 also provides evaluations of two seminal pool boiling HTC correlations, namely those by Foster and Zuber [61] and Cooper [62], parity plots for which are shown in Fig. 26(a) and (b). Surprisingly, both correlations show good accuracies against both the microgravity and terrestrial gravity flow boiling data despite being derived entirely from pool boiling data.

4.4.2. New HTC correlation for microgravity

In a precursor to the present study, Ganesan et al. [45] recently explored flow boiling HTC data trends for different cryogens based on a consolidated database they amassed from prior published literature. Like several formulations, they proposed the HTC involves contributions of both nucleate boiling and convective boiling via appropriate expressions for h_{nb} and h_{cb}, respectively. For h_{nb}, they suggested a dependence on single-phase heat transfer coefficient (based on total flow comprised entirely of liquid), $h_{sp,f}$, along with three other dimensionless parameters: boiling number, Bo (= q''/Gh_{fg}), pressure ratio, P_R (= P/P_{crit}), and local quality, $x_{e,z}$. And, for h_{cb}, they proposed a dependence on single-phase heat transfer coefficient (based on total flow comprised entirely of liquid), Lockhart-Martinelli parameter, X_{tt}, density ratio, and Confinement number, Co. Despite superior performance of the correlation against 1-g_e terrestrial HTC data, as evaluated in Kim et al. [42], inclusion of Confinement number (which is inversely proportional to square root of gravity) precludes its direct use for microgravity. Therefore, modified correlation form excluding Co is adopted to facilitate

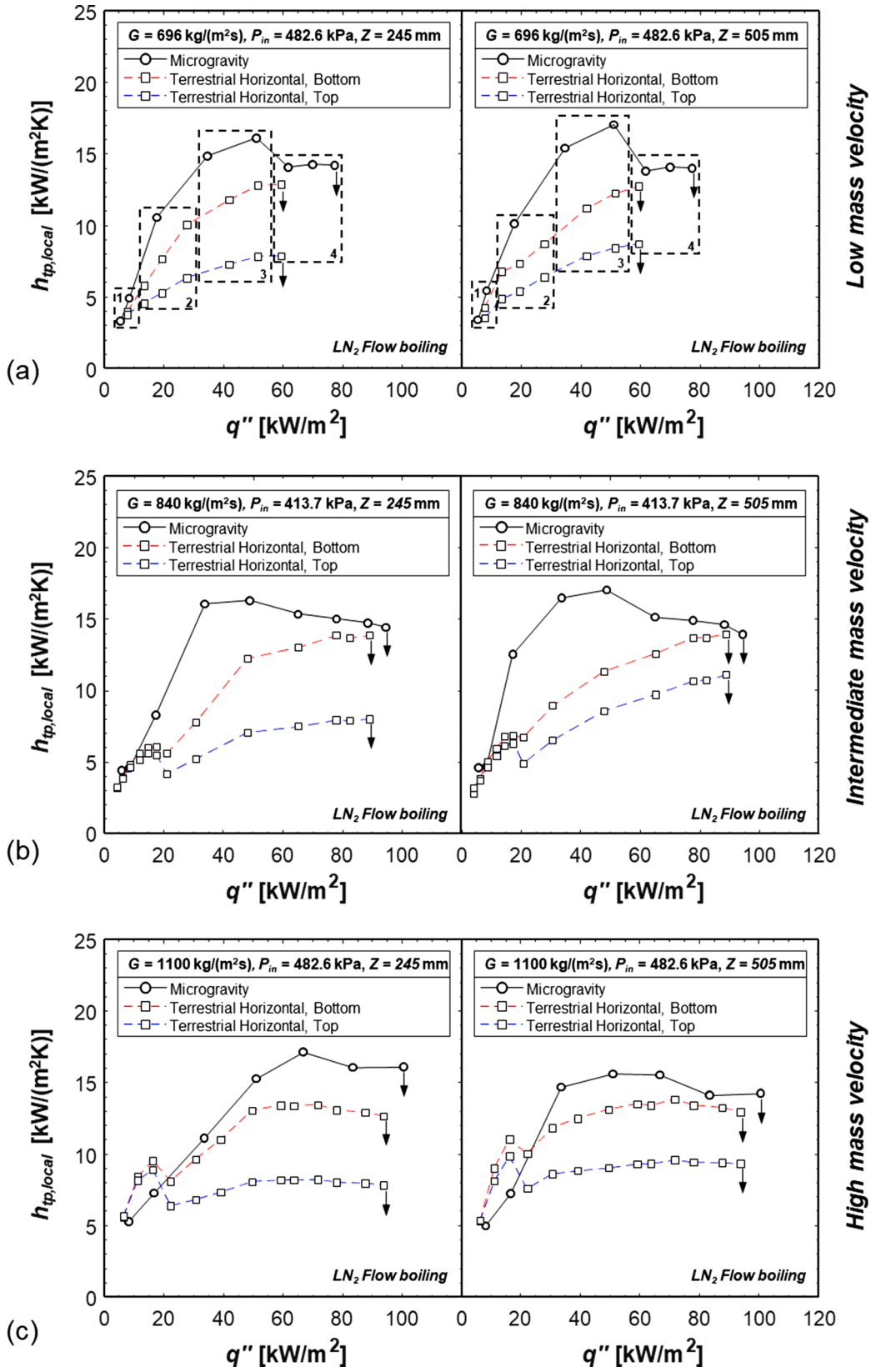

Fig. 24. Effects of gravity on local heat transfer coefficient for near-saturated inlet and mass velocities of G = (a) 695, (b) 840, and (c) 1100 kg/m^{2}s at two different axial location of z = 245 and 505 mm.

Table 3
Evaluation results for seminal flow boiling and pool boiling HTC correlations against present microgravity data and author's prior bottom-wall terrestrial horizontal flow data [42].

Authors	Year	MAE [%] (Microgravity)	MAE [%] (1 g_e Horizontal)	Functional form	Remarks
			Flow boiling correlations		
Chen [54]	1966	17.81	19.90	$h_{tp} = h_{pb}.S + h_{cb}.F$	
Shah [55]	1984	21.90	25.90	$h_{tp} = \max\{h_{nb},\ h_{cb}\}$	
Gungor & Winterton [56]	1987	28.18	37.17	$h_{tp} = h_{nb} + h_{cb}.F$	
Klimenko [57]	1990	110.50	19.57	$h_{tp} = \max\{h_{nb},\ h_{cb}\}$	Developed for cryogenic fluids; gravity reliant
Liu & Winterton [58]	1991	24.21	15.57	$h_{tp} = h_{pb}.S + h_{cb}.F$	
Steiner & Taborek [59]	1992	20.02	14.90	$h_{tp}^3 = h_{nb}^3 + h_{cb}^3$	Involves use of non-universal constants for different fluids
Kim & Mudawar [60]	2013	25.52	21.61	$h_{tp}^2 = h_{nb}^2 + h_{cb}^2$	
Present study	2022	19.77	20.36	$h_{tp}^2 = h_{nb}^2 + h_{cb}^2$	Modified correlation
			Pool boiling correlations		
Forster & Zuber [61]	1955	19.90	15.67	$h_{tp} = h_{pb}$	
Cooper [62]	1984	23.42	23.50	$h_{tp} = h_{pb}$	

accurate prediction of the present microgravity HTC data.

$$h_{tp}^2 = h_{nb}^2 + h_{cb}^2 \tag{17}$$

where

$$h_{nb} = \left[c_1 Bo^{c_2} P_R^{c_3} (1 - x_e)^{c_4}\right].h_{sp,f} \tag{18}$$

$$h_{cb} = \left[c_5 \left(\frac{1}{X_{tt}}\right)^{c_6} \left(\frac{\rho_f}{\rho_g}\right)^{c_7}\right].h_{sp,f} \tag{19}$$

$$h_{sp,f} = \frac{\left(4f_{sp,fo}/8\right)\left(Re_{fo,D} - 1000\right)Pr_f}{1 + 12.7\left(\frac{4f_{sp,fo}}{8}\right)^{0.5}\left(Pr_f^{2/3} - 1\right)} \frac{k_f}{D} \tag{20}$$

$$x_{e,z} = \frac{h - h_f}{h_{fg}} \tag{21}$$

To determine optimal values for empirical coefficients and exponents, a non-linear constrained minimization scheme was formulated in MATLAB, with the aim of minimizing MAE while avoiding non-physical trends. The optimization procedure yielded the final correlation

$$\frac{h_{tp}^2}{h_{sp,f}^2} = \left[210 Bo^{0.5} P_R^{0.1} (1 - x_e)^{-0.5}\right]^2 + \left[11 \left(\frac{1}{X_{tt}}\right)^{0.3} \left(\frac{\rho_f}{\rho_g}\right)^{-0.3}\right]^2 \tag{22}$$

which has a MAE of 19.77 % against the present local microgravity HTC data as depicted in Fig. 27. Notice the absence of gravity term from Eq. (18). To address ability to consider a variety of gravities, efforts are presently underway to supplement the microgravity data with terrestrial gravity data obtained at different flow orientations. This is expected to yield an improved correlation capable of capturing the fluid physics of cryogenic fluids for different gravitational environments, including microgravity.

5. Conclusions

The present study investigated microgravity flow boiling of LN_2 with a near-saturated inlet, utilizing data obtained from reduced gravity parabolic flight experiments. Comparisons of heat transfer data for both microgravity and terrestrial gravity, along with captured flow visualizations, provided insight into the effects of gravity on cryogenic flow boiling performance. Predictive accuracies of seminal HTC correlations were assessed relative to the microgravity data. Finally, a new HTC correlation was proposed to improve accuracy of microgravity HTC predictions. Key contributions from the study are as follows:

(1) High-speed video images revealed the following dominant flow regimes in microgravity: dispersed bubbly, large-oblong bubbly, and annular. Absence of buoyancy resulted in symmetrical flow structures regardless of operating conditions.
(2) Compared to 1-g_e and hypergravity, greater void fraction was observed in microgravity because of longer residence time on the heated wall.
(3) Additional insights were gained from video-captured temporal variations of flow structure, including (a) bubble size as well as bubble dynamics, such as collision followed by either coalescence or dispersion, (b) interface rupture and reconstruction during oblong bubble merging, and (c) liquid wave crest shattering and liquid droplet or ligament entrainment.
(4) Heat transfer data supported by flow visualization indicated transition from weak single phase liquid convection to more effective two-phase heat transfer occurs early along the boiling curve. Increasing the heat flux eventually culminates in annular flow wherein, because of low surface tension and low latent heat of vaporization for LN_2, heat transfer was augmented by bubble nucleation within the liquid film, a phenomenon rarely observed with room temperature fluids. Ultimately, partial dryout of the annular liquid film instigated CHF.
(5) Comparison of boiling curves and axial HTC profiles for microgravity and 1-g_e unveiled important effects of gravity on LN_2 flow

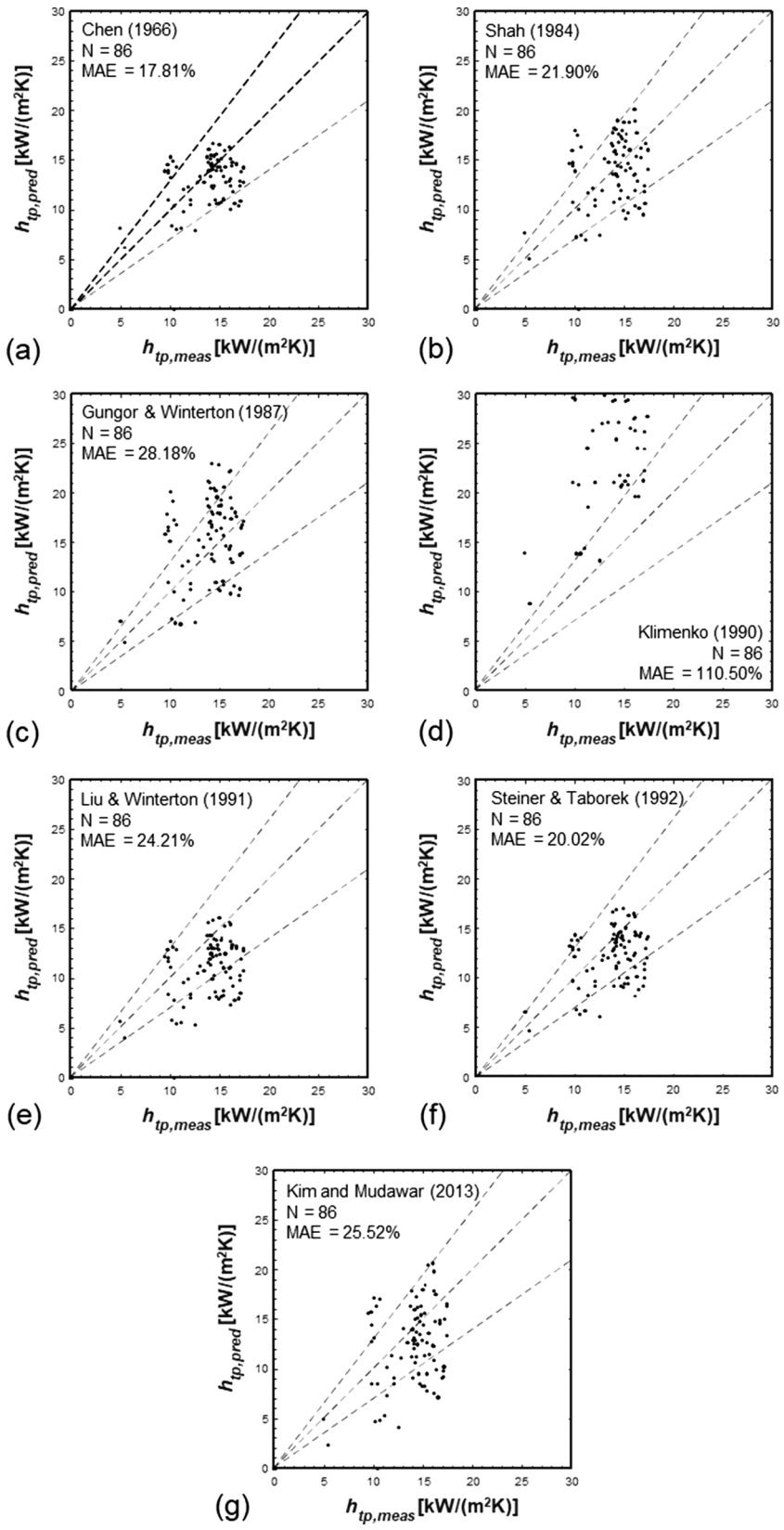

Fig. 25. Performance of seminal flow boiling HTC correlations against present measured microgravity HTC data.

boiling heat transfer performance. At very low heat fluxes, no significant gravity effects were observed, with bubble nucleation and cavity activation maintained close to the heated wall. At intermediate heat fluxes, HTC for microgravity was superior as large bubbles induced significant turbulence and mixing. However, the enhancement in microgravity HTC attenuated at high heat fluxes as flow pattern transitioned to annular. Overall,

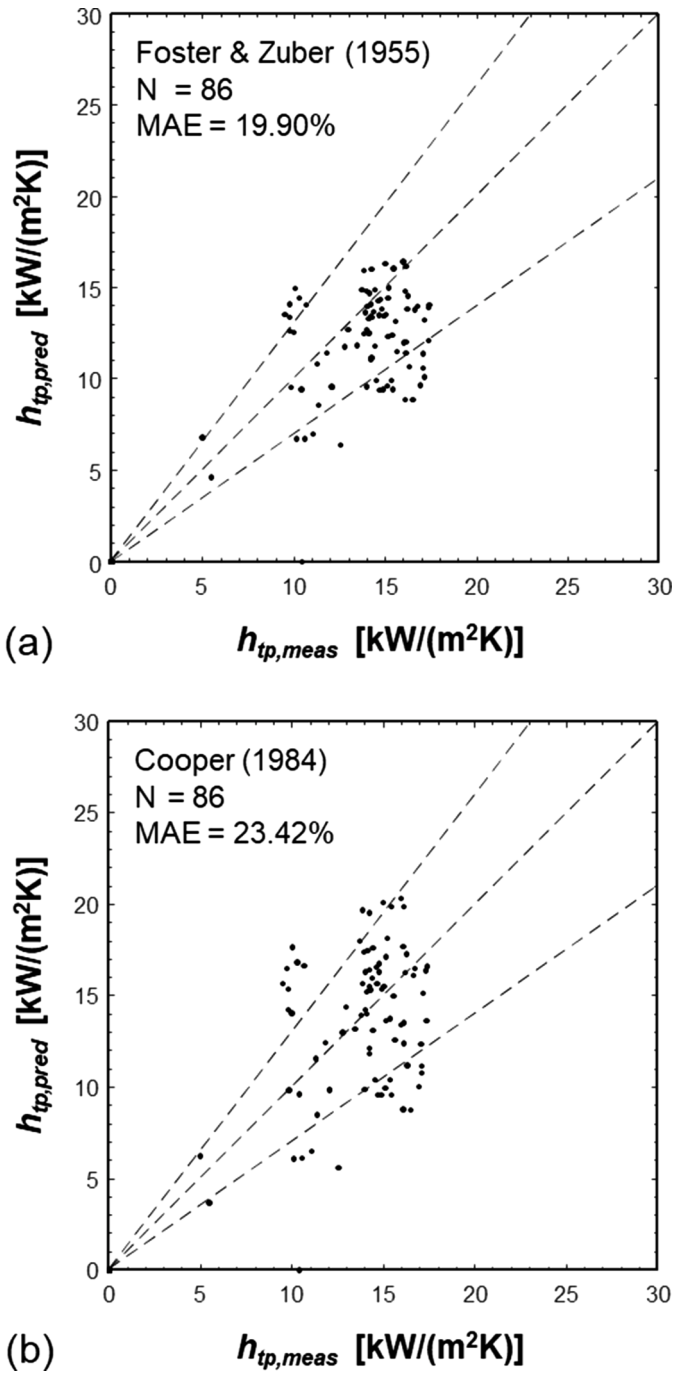

Fig. 26. Performance of seminal pool boiling HTC correlations against present measured microgravity HTC data.

differences in heat transfer performance and CHF between the two gravities gradually subsided with increasing mass velocity.

(6) Seminal HTC correlations were evaluated against the present microgravity HTC data, among which the correlation by Chen [54], with an MAE of 17.81 %, offers the best predictions. A new HTC correlation was also constructed to facilitate accurate prediction of the present microgravity HTC data.

(7) Several distinguishable behaviors of cryogens were observed all of which rooted from low surface tension and low latent heat of vaporization of cryogens: cryogenic flows in microgravity are (i) more susceptible to interfacial instability, (ii) able to sustain bubble nucleation within annular liquid film, (iii) able to persist high heat transfer coefficient at annular flow, and (iv) requires less lift force for bubble departure from the wall.

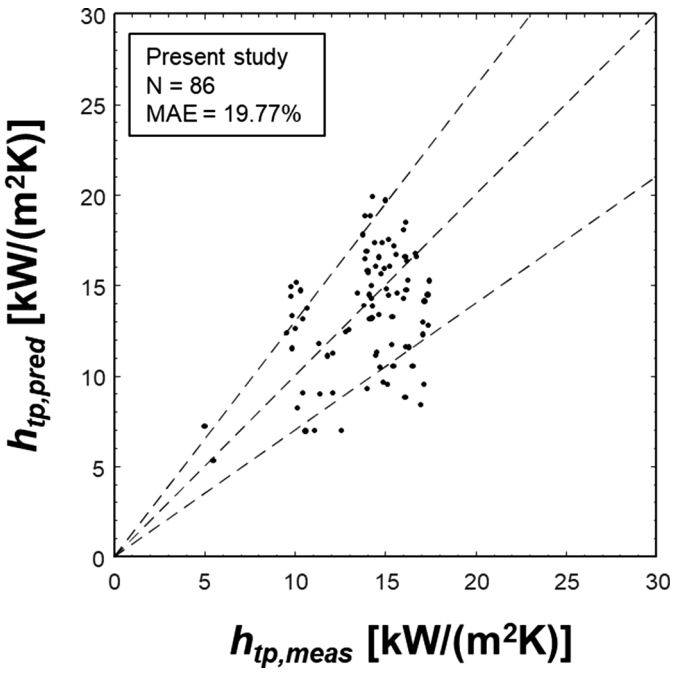

Fig. 27. Performance of new flow boiling HTC correlation against present measured microgravity HTC data.

Declaration of Competing Interest

The authors declare the following financial interests/personal relationships which may be considered as potential competing interests: Issam Mudawar reports financial support was provided by NASA John H Glenn Research Center.

Data availability

The authors are unable or have chosen not to specify which data has been used.

Acknowledgement

The authors are appreciative of the support of the National Aeronautics and Space Administration (NASA) under grants 80NSSC21K0500 and 80GRC018C0055.

References

[1] J.V. Noord, A heat transfer investigation of liquid and two-phase methane, NASA/TM-2010-216918, Cleveland, Ohio, 2010.
[2] A. Trejo, C. Garcia, A. Choudhuri, Experimental investigation of transient forced convection of liquid methane in a channel at high heat flux conditions, Exp. Heat Transf. 29 (1) (2016) 97–112.
[3] A. Trejo, A. Trujillo, M. Galvan, A. Choudhuri, J.C. Melcher, J.J. Bruggemann, Experimental investigation of methane convection and boiling in rocket engine cooling channels, J Thermophys Heat Trans 30 (4) (2016) 937–945.
[4] M.L. Meyer, L.A. Arrington, J.E. Kleinhenz, W.M. Marshall, Testing of a liquid oxygen/liquid methane reaction control thruster in a new altitude rocket engine test facility, NASA/TM-2012-217643, Cleveland, Ohio, 2012.
[5] W.H. Robbins, H.B. Finger, An historical perspective of the nerva nuclear rocket engine technology program, NASA contractor report 187154/AIAA-91-3451, NASA Lewis Research Center, Cleveland, Ohio, 1991.
[6] J.L. Felder, H.D. Kim, G.V. Brown, Turboelectric distributed propulsion engine cycle analysis for hybrid-wing-body aircraft, in: Proceedings of the 47th AIAA Aerospace Sciences Meeting Including the New Horizons Forum and Aerospace Exposition, Orlando, Florida, 2009.

[7] K. Parrish, S. Glazer, S. Thomson, The cryogenic thermal system design of NASA's James Webb Space Telescope (JWST) Integrated Science Instrument Module (ISIM), in: Proceedings of the SAE Technical Paper 22005-01-3041, 2005.

[8] M.L. Meyer, J.W. Hartwig, S.G. Sutherlin, A.J. Colozza, Recent concept study for cryogenic fluid management to support opposition class crewed missions to Mars, Cryogenics 129 (2023), 103622 (Guildf).

[9] J. Hartwig, J.N. Chung, J. Dong, B. Han, H. Wang, S. Darr, M. Taliaferro, S. Jain, M. Doherty, Nitrogen flow boiling and chilldown experiments in microgravity using pulse flow and low-thermally conductive coatings, NPJ Microgravity 8 (1) (2022) 1–33.

[10] W.L. Johnson, J.R. Stephens, NASA's cryogenic fluid management technology development roadmaps, in: Proceedings of the Joint Army-Navy-NASA-Air Force (JANNAF) In-Space Chemical Propulsion Technical Interchange Meeting (TIM), Huntsville, Alabama, 2018.

[11] J. Hartwig, J. Vera, Numerical modeling of the transient chilldown of a cryogenic propellant transfer line, J Thermophys Heat Trans 30 (2) (2016) 1–7.

[12] J. Hartwig, S. Darr, A. Asencio, Assessment of existing two phase heat transfer coefficient and critical heat flux correlations for cryogenic flow boiling in pipe quenching experiments, Int. J. Heat Mass Transf. 93 (2016) 441–463.

[13] D.J.H. Levack, J.F. Horton, T.R. Jennings, C.R. Joyner, T. Kokan, J.L. Mandel, B. J. Muzek, C. Reynolds, F.W. Widman, Evolution of low enriched uranium nuclear thermal propulsion vehicle and engine design, in: Proceedings of the AIAA Propulsion and Energy Forum, Indianapolis, Indiana, 2019.

[14] M. Mercado, N. Wong, J. Hartwig, Assessment of two-phase heat transfer coefficient and critical heat flux correlations for cryogenic flow boiling in pipe heating experiments, Int. J. Heat Mass Transf. 133 (2019) 295–315.

[15] T.J. LaClair, I. Mudawar, Thermal transients in a capillary evaporator prior to the initiation of boiling, Int. J. Heat Mass Transf. 43 (2000) 3937–3952.

[16] I. Mudawar, T.M. Anderson, Parametric investigation into the effects of pressure, subcooling, surface augmentation and choice of coolant on pool boiling in the design of cooling systems for high-power-density electronic chips, J. Electron. Packag. 112 (1990) 375–382.

[17] I. Mudawar, R.A. Houpt, Mass and momentum transport in smooth falling liquid films laminarized at relatively high Reynolds numbers, Int. J. Heat Mass Transf. 36 (1993) 3437–3448.

[18] I. Mudawar, D.E. Maddox, Enhancement of critical heat flux from high power microelectronic heat sources in a flow channel, J. Electron. Packag. 112 (1990) 241–248.

[19] C.O. Gersey, I. Mudawar, Effects of heater length and orientation on the trigger mechanism for near-saturated flow boiling critical heat flux-II. Critical heat flux model, Int. J. Heat Mass Trans. 38 (1995) 643–654.

[20] S. Mukherjee, I. Mudawar, Pumpless loop for narrow channel and micro-channel boiling, J. Electron. Packag. 125 (2003) 431–441.

[21] J. Lee, I. Mudawar, Fluid flow and heat transfer characteristics of low temperature two-phase micro-channel heat sinks –part 2: subcooled boiling pressure drop and heat transfer, Int. J. Heat Mass Transf. 51 (2008) 4327–4341.

[22] M.E. Johns, I. Mudawar, An ultra-high power two-phase jet-impingement avionic clamshell module, J. Electron. Packag. 118 (1996) 264–270.

[23] J.R. Rybicki, I. Mudawar, Single-phase and two-phase cooling characteristics of upward-facing and downward-facing sprays, Int. J. Heat Mass Transf. 49 (2006) 5–16.

[24] M.K. Sung, I. Mudawar, Single-phase and two-phase heat transfer characteristics of low temperature hybrid micro-channel/micro-jet impingement cooling module, Int. J. Heat Mass Transf. 51 (2008) 3882–3895.

[25] M.K. Sung, I. Mudawar, Single-phase and two-phase hybrid cooling scheme for high-heat-flux thermal management of defense electronics, J. Electron. Packag. 131 (2009), 021013.

[26] M. Saito, N. Yamaoka, K. Miyazaki, M. Kinoshita, Y. Abe, Boiling two-phase flow under microgravity, Nucl. Eng. Des. 146 (1994) 451–461.

[27] M. Misawa, An Experimental and Analytical Investigation of Flow Boiling Heat Transfer Under Microgravity Conditions, University of Florida, Gainesville, Florida, USA, 1993. Ph.D. thesis.

[28] H. Ohta, S. Baba, Boiling experiments under microgravity conditions, Exp. Heat Trans. 26 (2013) 266–295.

[29] H. Zhang, I. Mudawar, M.M. Hasan, Flow boiling CHF in microgravity, Int J. Heat Mass Transf. 48 (2005) 3107–3118.

[30] C. Konishi, H. Lee, I. Mudawar, M.M. Hasan, H.K. Nahra, N.R. Hall, J.D. Wagner, R. L. May, J.R. Mackey, Flow boiling in microgravity: part 1 - Interfacial behavior and experimental heat transfer results, Int. J. Heat Mass Transf. 81 (2015) 705–720.

[31] C. Konishi, H. Lee, I. Mudawar, M.M. Hasan, H.K. Nahra, N.R. Hall, J.D. Wagner, R. L. May, J.R. Mackey, Flow boiling in microgravity: part 2 - Critical heat flux interfacial behavior, experimental data, and model, Int. J. Heat Mass Transf. 81 (2015) 721–736.

[32] D.M. Iceri, G. Zummo, L. Saraceno, G. Ribatski, Convective boiling heat transfer under microgravity and hypergravity conditions, Int. J. Heat Mass Transf. 153 (2020), 119614.

[33] O. Kawanami, H. Azuma, H. Ohta, Effect of gravity on cryogenic boiling heat transfer during tube quenching, Int. J. Heat Mass Transf. 50 (2007) 3490–3497.

[34] K. Yuan, Y. Ji, J.N. Chung, W. Shyy, Cryogenic boiling and two-phase flow during pipe chilldown in Earth and reduced gravity, J. Low Temp. Phys. 150 (2008) 101–122.

[35] S. Darr, J. Dong, N. Glikin, J. Hartwig, A. Majumdar, A. Leclair, J. Chung, The effect of reduced gravity on cryogenic nitrogen boiling and pipe chilldown, NP J Microgravity 2 (2016).

[36] S. Kim, J. Lee, J. Hartwig, I. Mudawar, Computational investigation of vertical upflow boiling of liquid nitrogen and effects of bubble collision dispersion force, Int. J. Heat Mass Transf. 203 (2023), 123780.

[37] C. Konishi, I. Mudawar, M.M. Hasan, Investigation of the influence of orientation on critical heat flux for flow boiling with two-phase inlet, Int. J. Heat Mass Transf. 61 (2013) 176–190.

[38] Y.F. Xue, J.F. Zhao, J.J. Wei, J. Li, D. Guo, S.X. Wan, Experimental study of nucleate pool boiling of FC-72 on smooth surface under microgravity, Microgravity Sci. Technol. 23 (2011) 75–85.

[39] A. Weinzierl, J. Straub, Nucleate pool boiling in microgravity environment, in: Proceedings of the International Heat Transfer Conference, Munich, Germany, 1982, pp. 21–27.

[40] I. Mudawar, V.S. Devahdhanush, S.J. Darges, M. Hasan, H. Nahra, R. Balasubramaniam, J.R. Mackey, Heat transfer and interfacial flow physics of microgravity flow boiling in single-side-heated rectangular channel with subcooled inlet conditions – Experiments onboard the International Space Station, Int. J. Heat Mass Trans. 207 (2023), 123998.

[41] I. Mudawar, Flow boiling and flow condensation in reduced gravity, Adv. Heat Transf. 49 (2017) 225–306.

[42] S. Kim, N. Damle, J. Hartwig, I. Mudawar, Experimental heat transfer results and flow visualization of horizontal near-saturated liquid nitrogen flow boiling in uniformly heated circular tube under Earth gravity, Int. J. Heat Mass Transf., in Review.

[43] V. Gnielinski, Forced Convection in ducts, Hemisphere Handbook of Heat Exchanger Design, Hemisphere, New York, 1990.

[44] E.W. Lemmon, M.L. Huber, M.O. McLinden, NIST standard reference database 23: reference fluid thermodynamic and transport properties-REFPROP, Version 10.0, Gaithersburg, Maryland, 2018.

[45] V. Ganesan, R. Patel, J. Hartwig, I. Mudawar, Review of databases and correlations for saturated flow boiling heat transfer coefficient for cryogens in uniformly heated tubes, and development of new consolidated database and universal correlations, Int. J. Heat Mass Transf. 179 (2021), 121658.

[46] S. Baek, I. Park, Y. Jung, S. Jeong, Cool-down characteristics of liquid nitrogen transfer line, in: Proceedings of the 8th KSME-JSME8th KSME-JSME Thermal and Fluids Engineering Conference, Incheon, South Korea, 2012.

[47] S.L. Sharma, T. Hibiki, M. Ishii, C.S. Brooks, J.P. Schlegel, Y. Liu, J.R. Buchanan, Turbulence-induced bubble collision force modeling and validation in adiabatic two-phase flow using CFD, Nuc. Eng. Des. 312 (2017) 399–409.

[48] J. Lee, S. Kim, I. Mudawar, Assessment of computational method for highly subcooled flow boiling in a horizontal channel with one-sided heating and improvement of bubble dispersion, Int. J. Therm. Sci. 184 (2023), 107963.

[49] Y. Taitel, D. Barnea, A.E. Dukler, Modelling flow pattern transitions for steady upward gas-liquid flow in vertical tubes, AIChE J 26 (1980) 345–354.

[50] V. Ganesan, R. Patel, J. Hartwig, I. Mudawar, Universal critical heat flux (CHF) correlations for cryogenic flow boiling in uniformly heated tubes, Int. J. Heat Mass Transf. 166 (2021).

[51] M. Narcy, E. de Malmazet, C. Colin, Flow boiling in tube under normal gravity and microgravity conditions, Int. J. Multiph. Flow 60 (2014) 50–63.

[52] C. Baltis, G.P. Celata, M. Cumo, L. Saraceno, G. Zummo, Gravity influence on heat transfer rate in flow boiling, Microgr. Sci. Technol. 24 (2012) 203–213.

[53] M.T. Lebon, C.F. Hammer, J. Kim, Gravity effects on subcooled flow boiling heat transfer, Int. J. Heat Mass Transf. 128 (2019) 700–714.

[54] J.C. Chen, Correlation for boiling heat transfer to saturated fluids in convective flow, Ind. Eng. Chem. Process Des. Dev. 5 (1966) 322–329.

[55] M.M. Shah, Prediction of heat transfer during boiling of cryogenic fluids flowing in tubes, Cryogenics 24 (1984) 231–236 (Guildf).

[56] K.E. Gungor, R.H.S. Winterton, A general correlation for flow boiling in tubes and annuli, Int. J. Heat Mass Transf. 29 (1986) 351–358.

[57] V.V. Klimenko, A generalized correlation for two-phase forced flow heat transfer—Second assessment, Int. J. Heat Mass Transf. 33 (1990) 2073–2088.

[58] Z. Liu, R.H.S. Winterton, A general correlation for saturated and subcooled flow boiling in tubes and annuli, based on a nucleate pool boiling equation, Int. J. Heat Mass Transf. 34 (1991) 2759–2766.

[59] D. Steiner, J. Taborek, Flow boiling heat transfer in vertical tubes correlated by an asymptotic model, Heat Trans. Eng. 13 (1992) 43–69.

[60] S.M. Kim, I. Mudawar, Universal approach to predicting saturated flow boiling heat transfer in mini/micro-channels – Part II. Two-phase heat transfer coefficient, Int. J. Heat Mass Transf. 64 (2013) 1239–1256.

[61] H.K. Forster, N. Zuber, Dynamics of vapor bubbles and boiling heat transfer, AIChE J 1 (1955) 531–535.

[62] M.G. Cooper, Saturation nucleate pool boiling - a simple correlation. First U.K. National Conference on Heat Transfer, Leeds, England, 1984, pp. 785–793.